DNA NANOTECHNOLOGY: THE DEVELOPMENT OF MULTI-FUNCTIONAL HYBRIDIZATION SENSORS

by

BRITTANY LYNN MUELLER
M.S. University of Central Florida, 2024
B.S. University of Central Florida, 2018

A dissertation submitted in partial fulfillment of the requirements
for the degree of Doctor of Philosophy in the Department of
Chemistry in the College of Sciences
at the University of Central Florida Orlando,
Florida

Fall Term
2024

Major Professor: Dmitry M. Kolpashchikov and Jef Hooyberghs

© Choose an item. Click or tap here to enter text.

ABSTRACT

Hybridization probes have been used to detect specific nucleic acids for the last 50 years. These probes have applications in medicine, including identifying disease-causing genes or multidrug resistant bacteria. To be considered robust, a probe should have high selectivity at ambient or low temperatures, be able to detect folded analytes, and remain economical for use in clinical settings. This work will uncover a challenge faced by molecular beacon probes (MBP), describe an adaptation to a molecular beacon probe (MBP) that enables the hybridization of the probe to a folded target, a multicomponent DNA sensor (OWL2) that overcomes common challenges faced by hybridization probes, and a thresholding sensor (MB-Th) that allows for the quantification of microRNA. Through the use of unwinding arms, the MBP adaptation and OWL2 sensor are able to hybridize with and detect folded analytes. Additionally, the OWL2 sensor contains two analytebinding arms to unwind folded analytes and two sequence-specific strands that bind both the analyte and a universal molecular beacon (UMB) probe to form a fluorescent 'OWL' structure. The sensor can differentiate single base mismatches in folded analytes in the

temperature range of 5–38 °C, even when challenged with excess wild-type analytes. The MB-Th sensor consists of two gates with increasing affinity for the target, with each varying in thermodynamic stability. The gates bind to separate molecular beacons, each with a unique fluorophore, and produce distinct signals that can be measured simultaneously. Both sensor designs are cost-efficient since the same UMB probe can be used to detect any analyte sequence. These sensors have significant clinical benefits for the diagnosis of non-invasive early-stage cancer and cancers associated with miRNA dysregulation.

Should you choose to include a dedication, it should be centered vertically on the page. If you choose, you may center it horizontally as well, provided it is no longer than a paragraph. There should be no heading on the dedication page. This is the only major section with no heading. Delete this page if you do not want a dedication.

ACKNOWLEDGMENTS

The Acknowledgments page is optional, but most theses and dissertations include a brief statement of thanks to advisers, committee members, or others who helped you during the thesis/dissertation process. If you include an Acknowledgments page, place it after the dedication page, or after the Abstract page, if you don't have a dedication page.

You should also use an Acknowledgment page to thank any funding organizations who supported your research. Many funding organizations require a notice of support, so be sure to ask your adviser if such a notice is necessary in your thesis or dissertation.

Delete this page if you do not need or want to include acknowledgments.

TABLE OF CONTENTS

LIST OF FIGURES

LIST OF TABLES

Do not delete the sample LIST OF TABLES. Instead, after you've added your own tables to the document, right-click on the Table 1 entry and select Update Field. When finished, delete these instructions.

LIST OF ABBREVIATIONS

A Adenine

AEGIS Artificially Expanded Genetic Information System

C Cytosine

DNA Deoxyribonucleic Acid

Df Differentiation Factor

G Guanine

LAMP Loop-mediated Amplification

LNA Locked Nucleic Acid

LOD Limit of Detection

MB Molecular Beacon

MBP Molecular Beacon Probe

PCR Polymerase Chain Reaction

RCA Rolling Circle Amplification

RNA Ribonucleic Acid

S/B Signal-to-Background Ratio

SNP Single Nucleotide Polymorphism

SNV Single Nucleotide Variation

T Thymine

Not every thesis or dissertation will need a LIST OF ACRONYMS or LIST OF ABBREVIATIONS.

Remember to alphabetize the entries in this section.

IF YOU DELETE THIS PAGE, BE VERY CAREFUL NOT TO DELETE THE SECTION BREAK.

Turn on Show/Hide so the section break is visible and does not get deleted by mistake.

CHAPTER ONE: INTRODUCTION

Disease & Genetics

Single nucleotide variations (SNVs) are the most common cause of genetic alterations in the human genome, and they have been linked to several different types of disease.[1–3] In Alzheimer's disease, a single mutation can affect the alternative splicing of the MAPT gene, leading to an imbalance in the ratio of 3- and 4-repeat tau isoforms.[4–7] Since Tau is a microtubuleassociated protein responsible for stabilizing microtubules, an imbalance in isoforms can lead to tau aggregation, toxicity, and neurodegeneration. Neurodegenerative, cardiovascular, and autoimmune diseases have all been associated with specific genotypes, and their detection can lead to an early diagnosis.[8–16]

Some genes, such as the miR17-92 cluster, are crucial in pathways that regulate cell proliferation and differentiation. When miR-17 is upregulated, it leads to uncontrolled cell proliferation and the growth of cancer cells.[17–19] Another regulatory gene, the epidermal growth factor receptor (EGFR), can lead to several types of cancers when dysregulated, including colorectal, renal, and non-small cell lung cancer.[20–27] Furthermore, a single SNV causing a T790M mutation can cause non-small cell lung cancer to become resistant to EGFR tyrosine kinase inhibitors and transform into small cell lung cancer.[27–29] Identifying this T790M mutation can help physicians choose medications more suited to their patients' needs. Aside from genetic disease, biosensors can further help physicians by detecting SNVs in clinically relevant microbes; early detection is crucial in treating infections caused by drug-resistant pathogens.[30–34] It is clear that the identification of SNVs and quantification of genetic expression levels is crucial to our understanding and treatment of disease. So, how can we detect them?

Methods of Detection

Traditional methods for SNV detection include DNA sequencing, polymerase chain reaction (PCR) with melting curve analysis,[35] and hybridization assays. DNA sequencing, such as next-generation sequencing (NGS), can identify many SNVs across the genome but requires expensive instrumentation, significant time for data processing, and is prone to false positives due to sequencing errors and data complexity.[36–38] PCR has an astounding range of applications, from probe-based real-time PCR to post-amplification product analysis, but relies on expensive instrumentation with precise temperature control for SNV differentiation.[39–42] Hybridization assays utilizing peptide nucleic acid and locked nucleic acid probes,[43,44] cycling probe technology,[45] TaqMan,[46] and Molecular Beacon Probes (MBP)[47] all suffer from the affinity/selectivity dilemma, which declares that tight binding of a probe to an analyte is associated with low selectivity.[48,49]

Recent advances in SNV detection include ratio sensing via the depletion of wild-type (WT) targets,[50] programmable DNAzymes,[51] the use of CRISPR/Cas systems in conjunction with hybridization chain reactions,[52] and detection via lateral flow dipsticks after recombinase polymerase amplification with altered primers.[53] The best-studied hybridization probes, however, all share the challenges of inefficient hybridization with RNA and DNA analytes folded in stable secondary structures, difficulty differentiating between wild-type (WT) and SNV-containing DNA at ambient temperatures, and their high synthetic cost.[48,49,54,55]

DNA Nanotechnology

DNA Nanotechnology

DNA nanotechnology uses the predictable base-pairing of DNA to create nanoscale constructs.[56–58] DNA is easy to synthesize, has low immunogenicity, and can self-assemble and be programmed to have a predetermined sequence.[59–62] Several motifs, including three and fourway junctions (Figure 1), can be used as building blocks to create 2D and 3D structures due to the presence of

'sticky ends' that enable the motifs to hybridize with each other.[63–67] In addition to the intrinsic properties of DNA, these building blocks impart an architectural quality to these nanostructures – the possibilities are seemingly endless.[68–71]

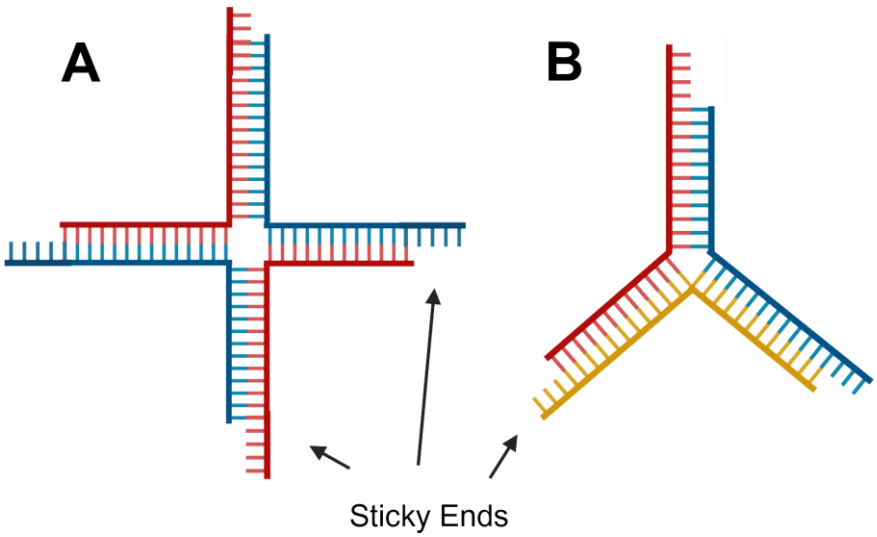

Figure 1. Four- and Three-Way Junctions are used in DNA nanotechnology assembly. **A)** Fourway Junction (4WJ) made with four separate strands, each containing an overhang of a singlestranded 'sticky end' sequence. **B)** A Three-way Junction structure containing sticky ends is made from three hybridized strands.

In a structural sense, DNA has been used to construct nanoscale lattices[72–74] and cargo vesicles.[75–78] Nanoscale lattices can be used as molecular scaffolds and aid in precisely placing molecules for molecular assembly. Cargo vesicles can be used for targeted drug delivery to reduce some of the off-target effects of traditional therapies. Some DNA nanostructures can monitor physical changes, such as pH and temperature,[79–83] and others act as a biosensor to convey information about biological systems, including disease markers.[84–86] Beyond their use as a biosensor, some have even been employed as therapeutic devices.[87–90] Despite its potential, DNA nanotechnology faces several challenges. DNA structures can be compromised through enzymatic degradation or other environmental factors. Some efforts to ameliorate these effects include modifications to the DNA or encapsulation of the structures.[91–94] Additionally, the complexity and size of the nanostructures are limited by scalability; the purification has proven to

be challenging to scale, and as more DNA strands are incorporated into a structure, the probability of assembly errors increases.[95–97] However, since many biologically relevant targets are small, the production of DNA biosensors doesn't necessarily need to be scalable – just measurable. One common way to measure the activity of DNA nanostructures is fluorescence, and a popular fluorescent reporter is the molecular beacon probe (MBP).

Molecular Beacon Probes

Design and Applications

Of the hybridization assays, the MB probe, a fluorophore- and quencher-labeled DNA hairpin, has one of the most elegant designs (Figure 2A).[47,98] The GC-rich stem enables the quencher and fluorophore to remain in contact for more efficient quenching without the complementary analyte sequence. Upon hybridization with the complementary analyte, the MB probe opens into an elongated conformation, and fluorescence is observed (Figure 2B).[47,98]

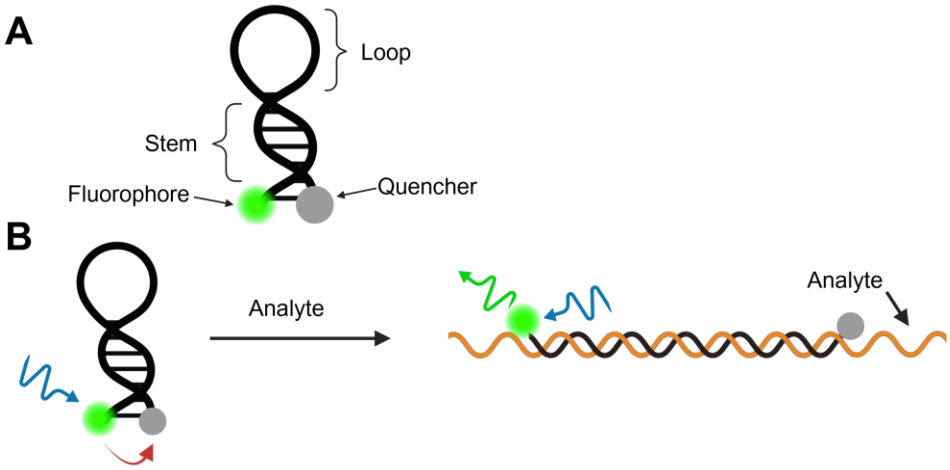

Figure 2. Design and Function of a Molecular Beacon Probe (MBP). **A)** Structure of an MBP probe: a DNA hairpin with a fluorophore at the 5'-end and a quencher at the 3'-end. **B)** The MB probe is in a quenched and closed conformation (left) before opening into a fluorescent structure (right) upon hybridizing with its cognate analyte [99]

A typical MBP achieves a limit of detection (LOD) of ~1 nM,[98] establishing it as a significant diagnostic tool capable of detecting specific nucleic acids after amplification.[100–102] Molecular

Beacon probes have been used in amplification assays such as nucleic acid sequence-based amplification (NASBA),[103] real-time PCR,[104] loop-mediated isothermal amplification (LAMP), [105,106] and rolling circle amplification (RCA).[107] Methods to improve the MBP detection limit include wavelength-shifting MBPs, which allow for a greater separation of the excitation and measured emission wavelength, thus reducing the background signal (Figure 3).[108] Another method, isothermal circular strand-displacement polymerization, has enabled MBPs to achieve femtomolar detection limits by using polymerase and primers to enable complete hybridization between analyte and probe.[109]

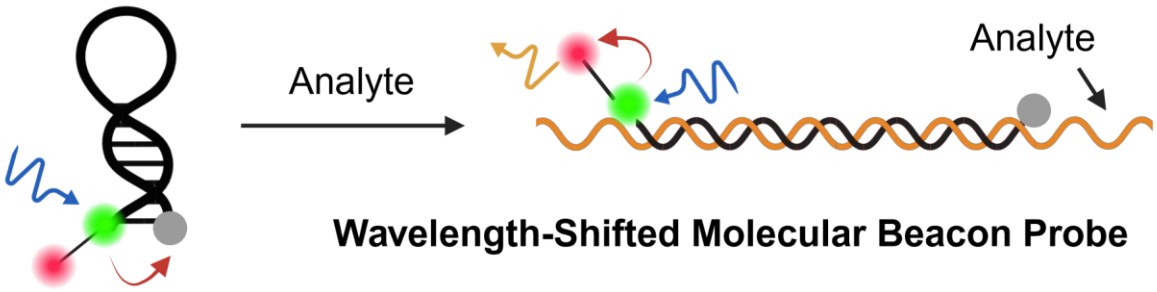

Figure 3. Wavelength-Shifted Molecular Beacon Probe.[99] In the closed state, the primary fluorophore's emission is quenched (grey sphere), and a signal is not produced. Upon forming a duplex with the analyte, the primary fluorophore (green) emits a wavelength that excites the secondary fluorophore (pink), and the final emitted wavelength can be read at a greater Stokes shift than a classical MBP.[108]

Challenges

One of the challenges of MBPs occurs when the MBP can adopt a secondary structure other than a hairpin, leading to stem- or loop- interference (Figure 4). Loop interference occurs when there is unwanted complementarity within the loop of the MBP, which increases the energy needed to open the MBP hairpin for hybridization with the target, thus decreasing the overall energy released upon analyte detection.[110–112] In stem interference, the MBP stem hybridizes with a segment of the MBP loop, resulting in a high background signal due to the fluorophore no longer

being in contact with the quencher. One proposed solution to combat stem interference includes using synthetic L-DNA in the MBP stem and natural D-DNA in the loop.[113] Since L-DNA and DDNA do not form duplexes, the stem cannot hybridize with the MBP loop, thus avoiding stem interference. This modification can additionally be used to solve the problem of stem invasion (Figure 5), which occurs when the MBP stem creates unwanted duplexes with G:C rich analytes. However, ordering MBPs with these modifications can be costly, with prices ranging from $120180 per modified nucleotide at a scale of ~250 nanomoles through companies such as Biosynthesis or GeneLink.

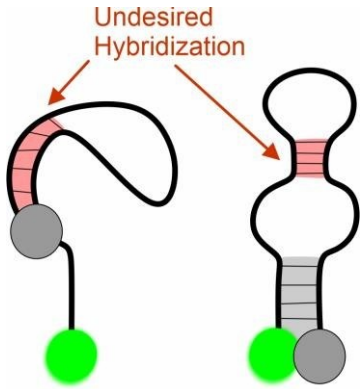

Figure 4. Stem and Loop Interference. Stem interference (left) occurs when nucleotides in the stem are complementary to the loop sequence in the MBP. Loop interference (right) occurs when there is additional complementarity in the loop of the MBP.

Another reported solution to circumvent the problem of stem interference and stem invasion uses modified bases developed as part of an artificially expanded genetic information system (AEGIS).[114] The modified base pairs were developed to hybridize with each other and maintain Watson-Crick geometry by maintaining size complementarity and controlling the donor/acceptor hydrogen bonds between two nucleobases. Due to the artificial nature of these nucleosides and their limitations of only forming a base pair with another synthetic nucleoside, they were successfully used to avoid stem invasion and interference.[115] However, they involve complex syntheses and, when purchased commercially, are expensive.[115–118]

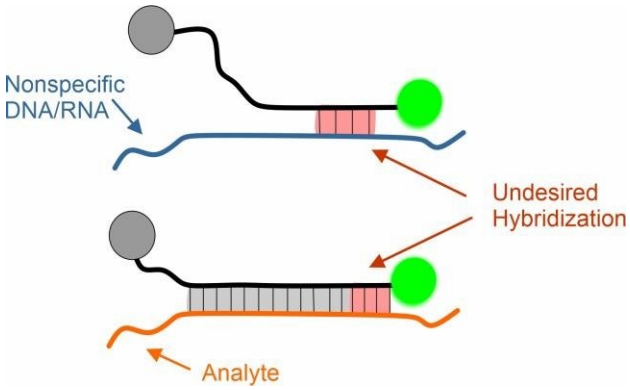

Figure 5. Stem Invasion of a Molecular Beacon Probe. Stem invasion occurs when the stem of the MBP hybridizes to a G:C rich segment of DNA or RNA (top) or when there is undesigned complementarity to the analyte beyond the MBP stem (bottom)

Yet another challenge of MBPs is the dimerization of MBP/analyte duplexes (Figure 6) which will be explored in depth in CHAPTER TWO: DIMERIZATION OF MOLECULAR BEACON PROBES. The fluorescent signal is reduced when MBP/analyte duplexes dimerize because the quencher of one duplex is brought close to the fluorophore of another duplex.

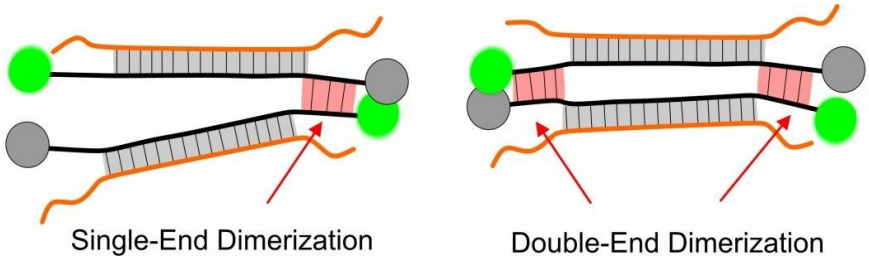

Figure 6. Dimerization of Molecular Beacon Probes. Unpaired nucleotides at the end of a MBP/analyte duplex can form dimers with a second MBP/analyte duplex either at one end (left) or both ends (right) of the dimer. Undesirable interactions are highlighted in red.

In addition to challenges posed by the structure of the MBP, the secondary structure of the analyte can further complicate successful detection. It has been shown that traditional MBPs cannot hybridize with analytes folded in stable secondary structures because both the MBP and analyte must overcome the unfolding of their secondary structure before they can hybridize.[112,119–121] This is especially true when the target sequence is sequestered within the analyte's secondary

structure in the form of dsDNA.[120] Modifications to the traditional MBP will be discussed in CHAPTER THREE: TAILED MB FOR IMPROVING THE DETECTION OF FOLDED ANALYTES.

The analyte's secondary structure can also affect how well the MBP can discriminate against SNVs. Although MBPs can differentiate SNVs in a broader temperature range than linear (hairpin-free) probes,[54] they fail to differentiate SNVs at ambient (0–40 °C) temperatures and, in practice, require costly instrumentation to measure DNA-melting profiles.[100–102] Melting profiles have shown that a mismatch in the target destabilizes the duplex formed between the MBP and target, which dissociates ~ 28 °C lower than the perfectly matched duplex.[122,123] To overcome this limitation and allow MBPs to differentiate SNVs at more ambient temperatures, multicomponent sensors can be used with a universal molecular beacon probe (UMBP).

Multicomponent Sensors

A DNA multicomponent sensor is created when multiple DNA strands are modularly designed so that each component possesses a different function.[124–126] Some common functions include target recognition, signal transduction, and signal amplification.[127–132] Having these different functions allocated to separate sensor regions enables the use of a UMBP. Unlike a traditional MBP, a universal molecular beacon probe is not limited to specific analyte sequences because it can be designed to be complementary to analyte-independent components of the sensor (Figure 7).[133–136] Since the fluorophore and quencher modifications are costly, and universal MBPs are unaffected by the need to redesign the MBP for each new analyte, they are a cost-effective alternative to the traditional MBP.

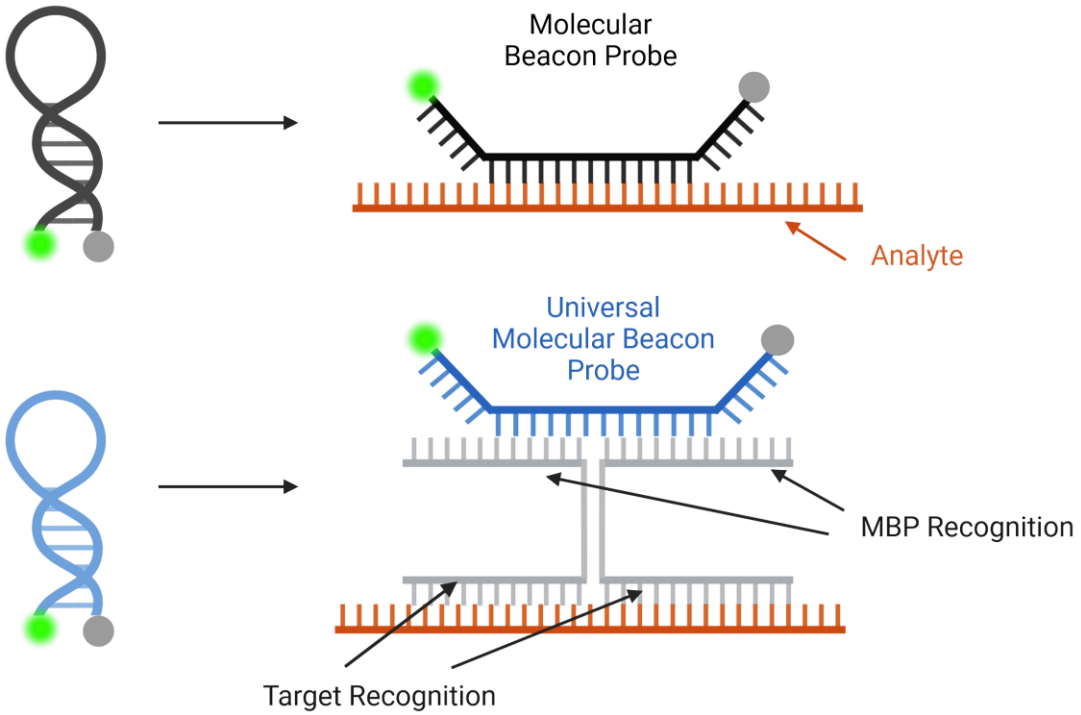

Figure 7. Function of a Universal Molecular Beacon Probe. The traditional MBP hybridizes directly with the target (top), whereas a universal molecular beacon probe hybridizes directly with the sensor and is analyte-independent.[99]

Aside from the cost, the use of UMBPs with multicomponent sensors allows for higher sensitivity and specificity than traditional MBPs or linear probes. Analyte-specific probes are challenged by the specificity and selectivity dilemma; as the duplex becomes long and affinity (specificity) increases, the energy penalty of a signal mismatch represents a smaller percentage of the ΔG of the analyte/probe duplex.[137] Additionally, as the affinity of the probe/analyte duplex increases, higher temperatures are needed to cause the two strands to dissociate. Although temperature control can be used to discriminate against analytes containing SNVs, these high temperatures require instrumentation that can be cost-prohibitive. Using a multicomponent sensor, the target recognition elements can be designed to use shorter sequences to hybridize with their target. This approach produces a higher relative energy penalty for the undesired duplex between a mismatched analyte and the sensor. Additionally, it lowers the temperature required for probe/analyte disassociation and SNV discrimination. The X-sensor, similar to the design with the

UMBP in Figure 7, took advantage of this effect and reduced the temperature needed for SNV differentiation to ~15 – 40 °C. The OWL1 sensor worked similarly, creating a rigid structure through locked ends with short analyte-binding regions to impart selectivity from ~ 5 – 32 °C (Figure 8)

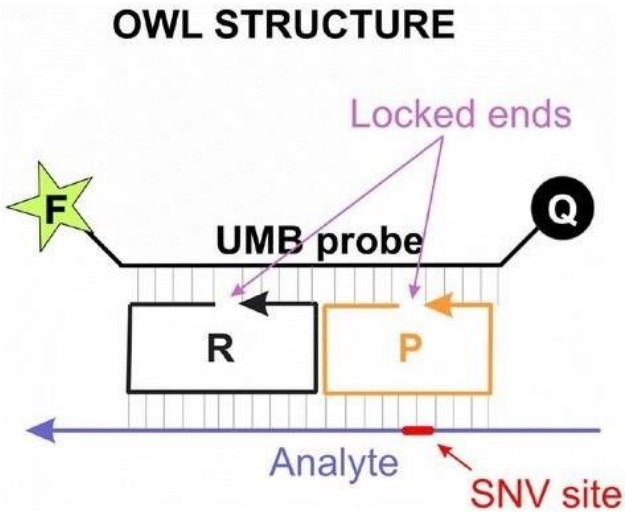

Figure 8. OWL1 Structure consists of the analyte complexed with the sensor's R and P strands, which report the signal through a UMBP.

There is a need to continue the development of these sensors so that they can be easily used in a point-of-care setting and enable clinicians to detect disease biomarkers without significant cost to the patients.

Research Questions

After encountering a challenge with MBPs that were seemingly self-quenching, we set forth to (1) determine the cause of the quenching and which factors, if any, must be present to avoid it. To improve the functionality of MBPs, we also hypothesized that we could (2) adapt a molecular beacon probe to overcome the challenge of hybridizing with its target by including a target-specific 'unwinding' sequence.

Using a universal MBP, we moved forward with multicomponent biosensors. Inspired by the cost-efficient design and the excellent selectivity of the OWL1 sensor, we wanted to overcome

its ability to detect folded targets. We hypothesized that we could (3) use single-stranded ‘unwinding arms’ to allow the sensor to detect folded targets while maintaining selectivity and functionality over broad temperature ranges. In doing so, we could create a cost-efficient sensor that could apply to a broader array of biomarkers. In addition to using unwinding arms in our sensor, we were interested in the applicability of the sensor to more clinically relevant samples containing an excess of wild-type analytes and a small fraction of mutant disease-causing analytes. This required a high degree of selectivity, so we hypothesized that (4) detection of the mutant analytes could be enhanced through the depletion of wild-type targets by using a ‘blocking strand.’

Seeking to develop more biologically relevant biosensors, we aimed to design a ‘thresholding sensor,’ which could differentiate between pathogenic and healthy miRNA concentrations. We thought that we could (5) create a thresholding DNA device by designing separate regions of a DNA sensor to have different affinities to the same miRNA, with each having a distinct reporter.

This work aims to contribute to diagnostic medicine by using DNA nanotechnology to develop biosensors with multiple functions to overcome common challenges, including specificity, selectivity, stability, biocompatibility, and cost.

CHAPTER TWO: DIMERIZATION OF MOLECULAR BEACON PROBES

Introduction

Established challenges of molecular beacon probes include loop interference, stem interference, and stem invasion.[98] In this chapter, we discuss yet another problem in the design of MBPs: dimerization of the MBP/analyte complex due to the interactions of stem-forming

nucleotides as shown in Figure 9. The hybridization of the MBP loop to analyte results in a duplex flanked by the unpaired stem-forming nucleotides, which can then hybridize with another MBP/analyte complex to form a four-stranded structure which results in a ‘dark’ conformation. In this structure, one MBP's 5’- fluorophore is quenched by the 3’- quencher on another MBP, and vice versa.

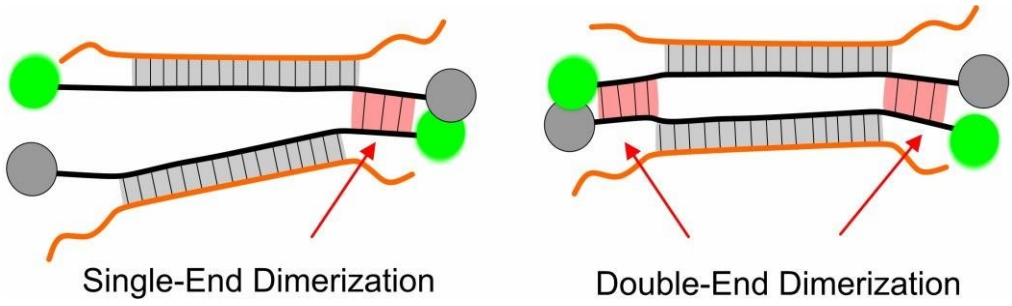

Figure 9. Dimerization of Molecular Beacon Probes. Unpaired nucleotides at the end of a MBP/analyte duplex can form dimers with a second MBP/analyte duplex either at one end **(left)** or both ends **(right)** of the dimer. Undesirable interactions are highlighted in red.

Results and Discussion

MBP3 and Dimerization

We first observed the dimerization with a MBP containing a six nucleotide base pairs (bp) stem and a 22-nt loop (Figure 10A). The MBP (MBP3) contained a CY5 fluorophore at the 5’- end and a quencher at the 3’- end. We found that some analytes resulted in a signal increase followed by a sharp decrease within five minutes or less (Figure 10). We hypothesized that our MBP/analyte was dimerizing and analyzed our system using native polyacrylamide gel electrophoresis (PAGE) (Fig. 2C). We found that an upward shift on the gel correlated with the fluorescence quenching (Fig. 2B). The Dimerization occurred when there were less than four bp complementary to each end of the MB1 stem.

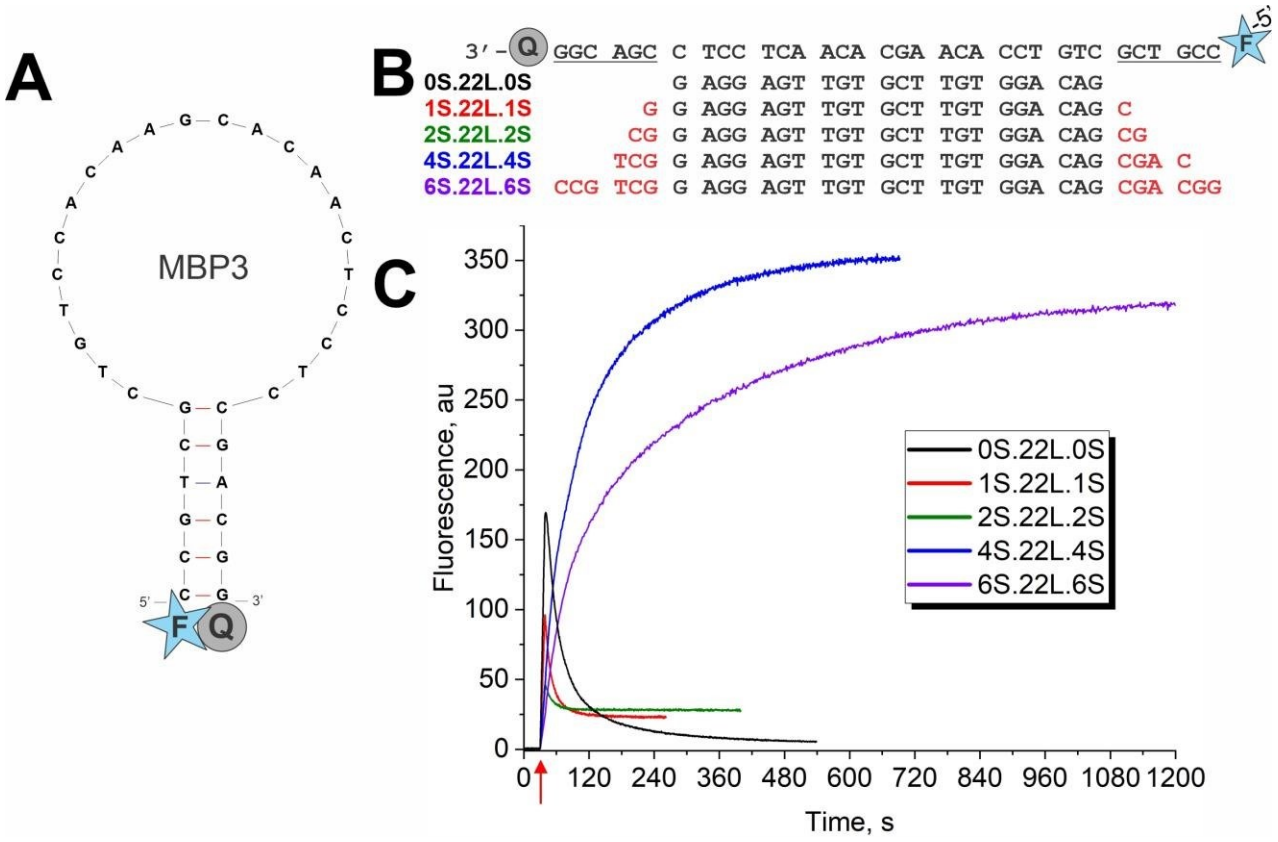

Figure 10. Four free nucleotides on each end of MBP in MBP/analyte complex are sufficient to trigger dimerization. **A)** Sequences of analytes, 5'→ 3' with MB (3' → 5') with red nucleotides representing those complementary to the MB probe stem. **B)** The hybridization kinetics of Cy5MB upon the addition of analyte.

Next, we tested analytes that had complementarity to the 3'- end of the MBP3 stem to determine if the dimerization would still occur when only one end of the MBP hybridized with the analyte (Figure 11A). We found that all four analytes experienced the quenching effect and resulted in a fluorescence higher than baseline after reaching equilibrium. (Figure 11B). However, analyte 2X.20L.0S experienced the most quenching, in contrast to 2X.20L.3S. This provided evidence that increasing complementarity to the 3'- end of the stem can partially prevent some quenching. When there is no complementarity to either side of the stem (2X.20L.0S), the fluorophores from each dimerized MBP can be quenched by the opposing co-hybridized MBP, but when the analyte does have complementarity to one end of the stem, we observe partial quenching as the dimerization occurs only at one end of the dimer (Figure 9).

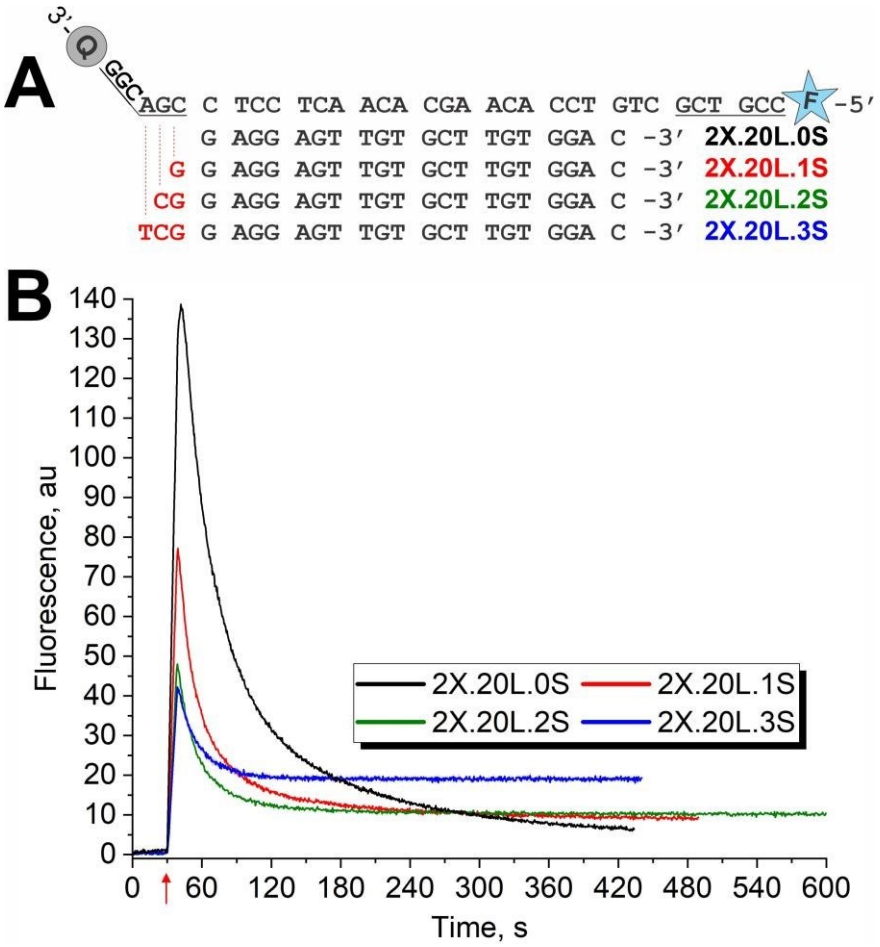

Figure 11. Dimerization of MBP/analyte complex. **A)** Sequences of the targets possessing complementarity to the molecular beacon at the 3'- end of MBP; nucleotides complementary to the stem are red, and nucleotides corresponding to the stem in the MB are underlined. **B)** Time dependence of hybridization between 50 nM MB1 and 100 nM of each analyte at 22 °C. The hybridization buffer had [Tris-HCl] = 50 mM, [$MgCl_2$] = 50 mM, pH=7.4, and 0.1% Tween-20. The analytes were added at the 30-second time point, indicated by the red arrow, and data was collected from ~35 sec onward. The secondary structure of MBP3 was determined by Mfold using the buffer conditions.

Next, we tested analytes with the same number of nucleotides as those in Figure 11 but with complementarity to the 5' end of UMB3 (Figure 12A) to investigate if the effect is locationspecific for the 3'- and 5'- end of the MBP. We found that dimerization occurred for 0S.20L.2X and

1S.20L.2X, with zero and one nts complementary to the 5'- end of the stem, respectively. However, upon hybridization with 2S.20L.2X and 3S.20L.2X, we found that dimerization and quenching were not observed (Figure 12). We observed a slower fluorescent response for 3S.20L.2X, which

could be explained by its stable secondary structure (Fig. S1). This result showed that for MB1, two nucleotides complementary to the stem's 5'- end were necessary to prevent dimerization.

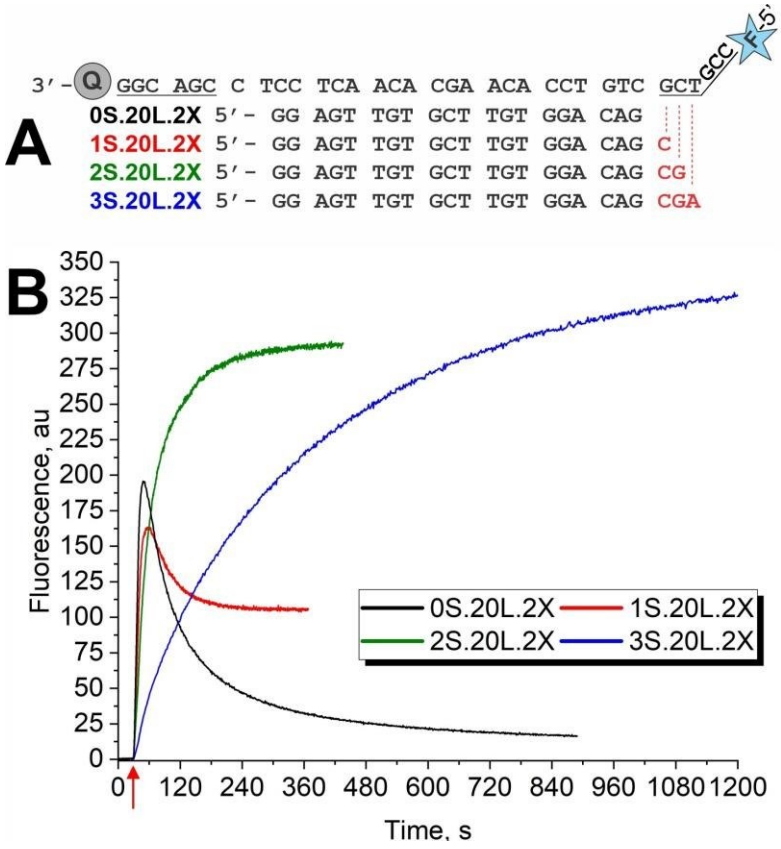

Figure 12. Dimerization of MBP/analyte complex with complementarity to the 5' end of MBP3. **A)** Sequences of the targets possessing complementarity to the molecular beacon at the 5'- end of MBP; nucleotides complementary to the stem are red, and nucleotides corresponding to the stem in the MBP are underlined. **B)** Time dependence of hybridization between 50 nM MBP3 and 100 nM of each analyte under the same conditions as Fig. 2. The analytes were added at the 30-sec time point, indicated by the red arrow, and data was collected from ~35 sec onward.

To eliminate the possibility of the two unpaired nucleotides in the MB1 loop contributing to the dimerization, we tested three analytes that hybridized to all nucleotides in the MB1 loop; 0S.22L.0S contained no stem-hybridizing nts and 3S.22L.0S and 0S.22L.3S contained three additional nts complementary to the 5'- and 3'- end of the MB1 stem, respectively (Figure 13). The findings were similar; three nts complementary to the 5'- end of MB1 were sufficient to prevent dimerization.

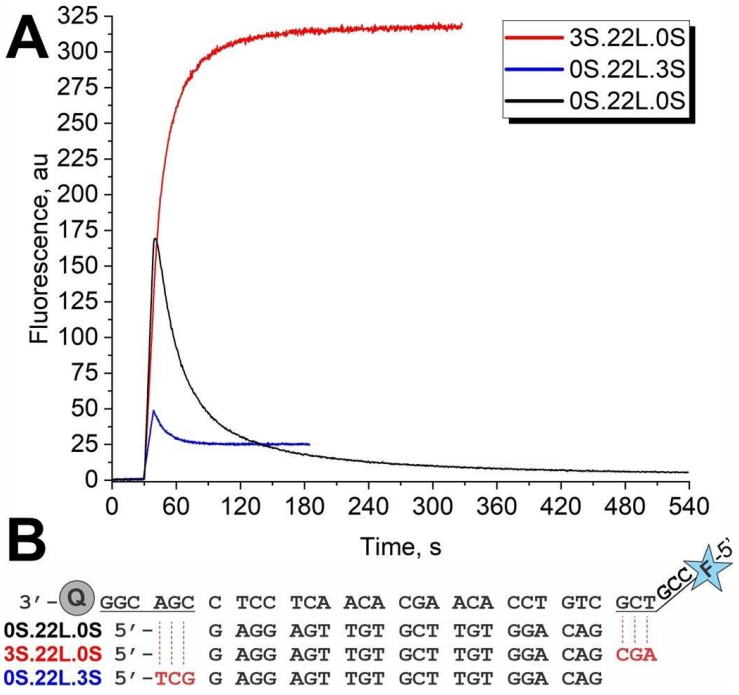

Figure 13. Kinetics of MBP3 with loop complementarity and 3nt hybridizing to each end of the MB stem. **A)** Sequences of MBP3 and the analytes added. Nucleotides in red correspond to those that hybridize with the stem of the MB probe **B)** The hybridization kinetics of MBP3 upon the addition of analyte.

τMB and Dimerization

Next, we assessed the dimerization of MBP/analyte using a different MBP, τMB, and analytes containing complementarity to either end of the MBP stem (Fig S3A). We found that, again, dimerization occurred when the complementarity to the stem was on the 5'- end of the MBP but, for τMB, only a single nucleotide was needed to inhibit dimerization (Fig. S3B). Next, we challenged our system to see if mismatches would impact the dimerization. We used Tau17 2nt3' and Tau17 2nt5', two biologically relevant analytes that contained mutations responsible for Alzheimer's disease (Fig. S4A). Dimerization occurred when there were two nts mismatched to the 3'- end of the MBP stem but not when the two nts were facing the 5'- end (Fig S4B). Additionally, although there were differences in the hybridization rate and thermodynamics, the

mismatches in the center of the analyte appeared to have no impact on dimerization (Fig S4B, S5, S6).

Discussion

Through a systematic study, we determined which criteria should be considered to prevent the 'dimerization' of MBP/analyte complexes. We propose that dimerization occurs through the sticky ends (SE) of the MBPs after the MBP/analyte complex is formed. However, dimerization can be prevented by including 1-2 nucleotides that interact with the 5'- end of the MBP. Sticky ends are unpaired nucleotides that extend beyond a double-stranded DNA helix and are an important tool in DNA recombinant technology. Additionally, these SE are commonly used in DNA origami and are integral in hybridization chain reactions.22–26 Technologies that depend on carefully designed SE are frequently challenged by input-less initiation and subsequent aggregation. The efficiency of SE pairing can be determined via many methods, including realtime fluorescence using MBPs.27 Upon hybridization of the MBP to the target, the probe transitions from a 'closed' hairpin conformation to an 'open' fluorescent state. In this open state, the unpaired SE can dimerize with another MBP: target complex to form a quaternary structure with reduced fluorescence (Fig. 1C).

Conclusion

Modified MBPs have been used in assays to create SE pairing that can be recognized and degraded by a nuclease, resulting in signal amplification and an improved limit of detection.28 Considering both the advantages and unwanted interactions of the SE pairing of MBPs, there is a clear need to understand the parameters that both promote and inhibit this dimerization. One possible solution to the MBP dimerization problem is using a universal MBP approach.29 In this approach, a single optimized MBP is used to analyze any given analyte using two adaptor strands. Therefore, the sequence of such a universal MBP and its interaction with the adaptor strands can

be pre-designed to avoid the dimerization problem, and the universal MBP can be used with all given analytes without the need to change the MBP sequence.

CHAPTER THREE: TAILED MB FOR IMPROVING THE DETECTION OF FOLDED ANALYTES

Introduction

Although the MB probe has proven useful in detecting shorter analytes **(Figure 14A),** detecting folded RNA and DNA has posed a fundamental challenge.[98] The association between the MB probe and targets diminishes when the target is folded in a stable secondary structure **(Figure 14B)**.[138–143] This can impact both the thermodynamic stability of the MB probe/target complex and the hybridization rates.[144] Improvement of MB hybridization kinetics is significant since a typical hairpin-folded probe reaches a plateau after 15-30 min of incubation in homogenous formats[145,146] and 90 min in heterogeneous formats.[147] This time extends analytical assays and reduces the practical value of MB and other harpin-shaped probes. Therefore, a universal and straightforward approach is needed to increase MB probe hybridization rates.

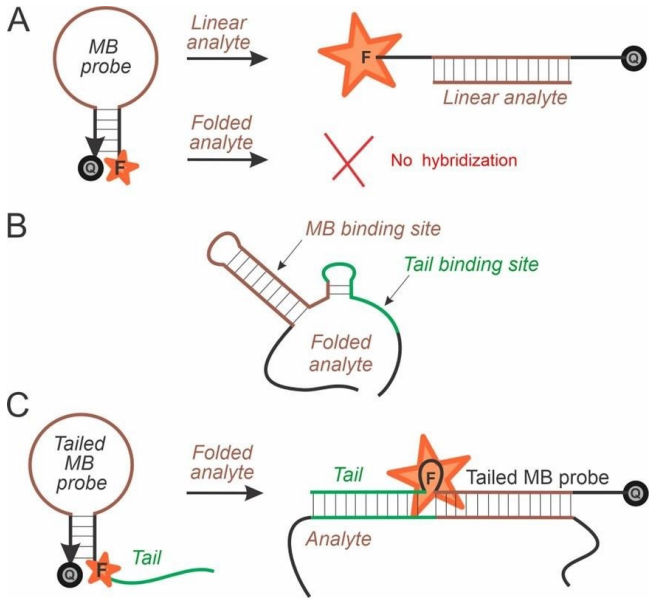

Figure 14. The design of the tailed MB probe. A) The classical MB probe fluoresces upon binding linear analyte but cannot bind to folded DNA or RNA. B) Nucleic acid analyte folded in a stable secondary structure. C) The tailed MB probe efficiently hybridizes with the folded analyte.

Here, we report a strategy to increase both the stability of the MB/analyte complex and its hybridization rates by tailed MB probes **(Figure 14C)**. Tailed MB probes are equipped with a

single-stranded sequence (tail) at one end complementary to the sequence adjacent to the MB loop-targeted sequence. The addition of the tail sequence serves a dual purpose. First, the tail, once hybridized with the analyte, lowers the free energy of the MB/analyte complex. The lower free energy results in an equilibrium shift, which favors complex formation and increases the signal-to-background ratio (S/B). Secondly, tailed MB probes increase the hybridization rates due to the binding of the tail to secondary structure-free nucleotides, thus bringing the MB loop near the targeted sequence.

Results and Discussion

MB1 and MB1-Tail for the Detection of 16S WT Analyte

To prove our hypothesis, we chose a fragment of *E. coli* 16S rRNA that can be used to differentiate *E. coli* from other bacteria. The selected 60 nt fragment (61-120 nt of natural rRNA sequence) contained a stable stem-loop structure **(Figure 15B)**, also present in the natural rRNA secondary structure. An MB1 probe was designed to be complementary to one side of the stem (brown line in **Figure 15B**). The lengths and sequences of the stem and the loop regions of the MB1 probe were designed based on the state-of-the-art procedure for MB probes.[98] The MB1 failed to detect the folded 60-nt 16S DNA analyte as reflected by the S/B ratio of ~1.1, a phenomenon previously reported **(Figure 15C, Figure 16)**.[120,143] This S/B is too low to be useful for practical applications, as the S/B should be at least 1.5 for fluorescent assays.[54]

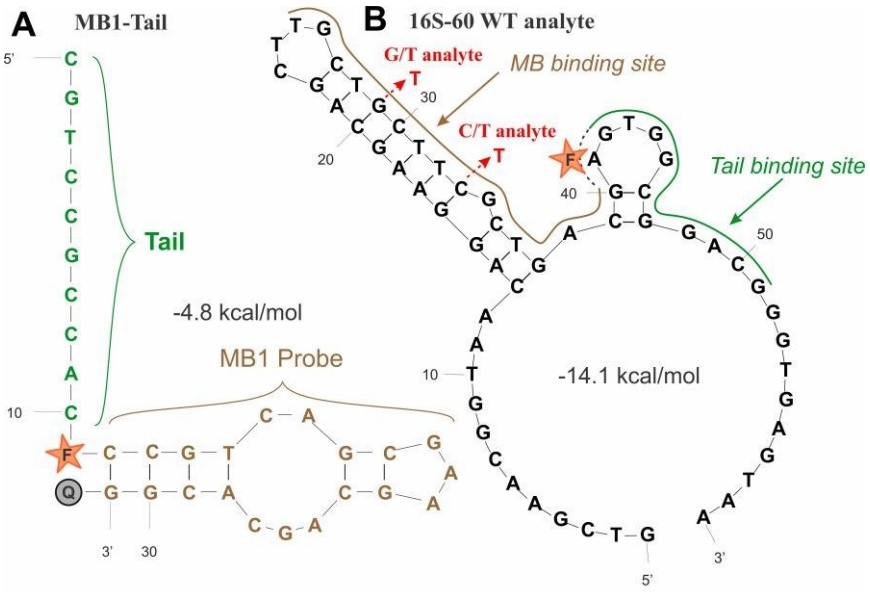

C

ΔG of analyte folding	ΔG of MB Probe/analyte	Change in ΔG upon complex formation	S/B
16S-60 WT ~ -14.1	MB1-Tail ~ -44.7	~ -25.9	42.6
	MB1 ~ -28.9	~ -10.0	1.1

ΔG are in kcal/mol

Figure 15. Structural and Thermodynamic Data for MB1, MB1-Tail, and 16S-60 WT. **(A)** Primary and secondary structures of MB1-Tail probe. **(B)** The cognate analyte 16S-60 WT, with arrows that indicate the two SNVs. **(C)** The secondary structures and Gibbs energy values (ΔG) were obtained at 22 °C, [MB]= 50 nM, [Analyte]= 100 nM, [Na+] = 50 mM, and [Mg2+] = 50 mM using Mfold.[147]

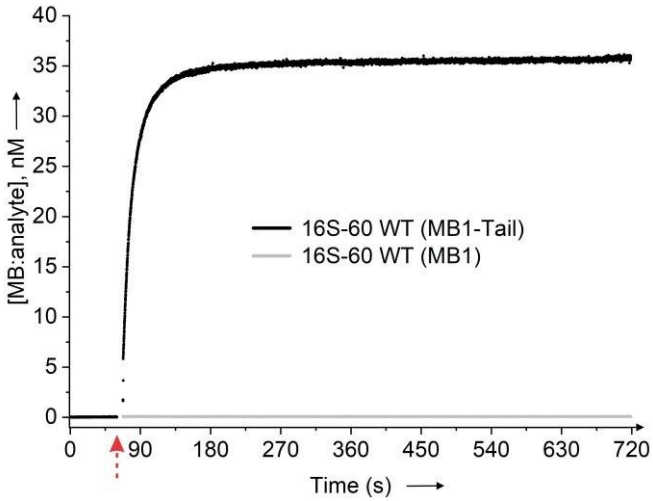

Figure 16. Tailed MB probe improves hybridization thermodynamics. Time dependence of hybridization between 50 nM MB1 and MB1-Tail with 100 nM folded 16S analyte. The hybridization buffer had [Tris-HCl] = 50 mM, [MgCl2] = 50 mM, pH=7.4, and 0.1% Tween-20. The

analytes were added at the 60-sec time point, indicated by the red arrow, and data was collected from 70-sec onward. The concentration of MB:Analyte was determined via calibration curves with MB:analyte duplexes (Fig. S1).

The MB1-tail was designed by adding a 10 nt DNA 'tail' at the 5' end of the MB1 probe (green sequence in **(Figure 15A)**, with an internal fluorophore linked to position 5 of a thymidine. The tail sequence was complementary to the relatively accessible analyte fragment that was not folded in a stable secondary structure (as predicted by Mfold). The free energy of the MB1tail:16S-60WT complex was reduced by – 15.8 kcal/mol and resulted in a 40-fold increase in the S/B ratio compared with the MB1:16S-60WT complex **(Figure 15C).** Additionally, the limit of detection (LOD) for the 16S-60 WT could not be determined with MB1 but was 0.7 nM with MB1-Tail, which is approximately the LOD for traditional MB probes with unfolded targets (Fig. S1).[98]

To further confirm that interaction between the tail fragment and the analyte is essential for achieving high S/B, we investigated the hybridization of MB1 and MB1-Tail probes with short (16 nt) analyte fragment containing only nucleotide sequence complementary to the loop region of MB1 and MB1-Tail (Fig. S2A). The fragment did not form a stable secondary structure (ΔG ~ – 1 kcal/mol, Fig. S2). MB1 and MB1-Tail produced S/B of ~5 and 7, respectively, in the presence of unfolded 16S-16 analyte (Fig. S2B). The LOD for 16S-16 WT was 3.6 nM for MB1-Tail and 6.1 nM for MB1 probe (Fig. S1). The comparable LOD and S/B reflect similar complex stability for the two MB probes and emphasize the importance of tail fragment interaction with the folded analyte for achieving high S/B.

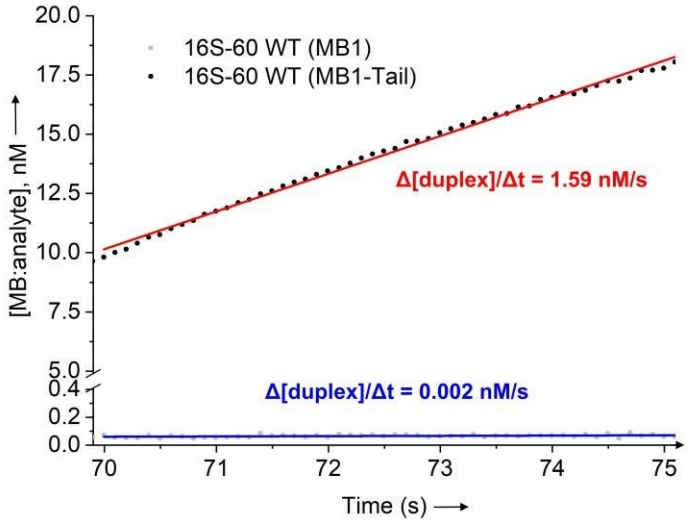

Figure 17. MB1-tail improves hybridization kinetics. Initial hybridization rates of 16S Analyte with MB1 and MB1-tail. The data was measured in triplicate, and the average was fit with a line of best fit using the concentration of the formed duplex over the first five seconds. The slope was taken to be the initial rate of duplex formation.

The hybridization rate of the MB1-tail probe was about 800-fold higher (1.6 nM/s) than that of the MB1 probe (0.002 nM/s, **Figure 17**). At the same time, hybridization with the short 16S-16 analyte had comparable kinetics (initial rates of 0.002 nM/s and 0.007 nM/s, for MB1-Tail and MB1 probe, respectively (Fig. S2). This result proves that the tail fragment is the key functional component of the MB1-Tail probe that improves hybridization kinetics.

τMB and τMB-Tail for the Detection of τ-60 WT Analyte

To check for the general applicability of our tailed MB strategy, we developed a tailed and non-tailed MB probe, τMB-Tail and τMB, respectively, for the detection of another folded analyte, a fragment of tau gene and two of its mutations (Fig. S3). The two mutations, τ-60 0C and τ-60 1A, contribute to the development of Alzheimer's disease via an alternative splicing pathway and skew the ratio of tau protein isoforms, leading to neurofibrillary tangles.[148] We initially designed τMB-Tail and τMB as described above for the 16S-60 analyte, but the tail fragment of τMB-Tail appeared to be complementary to the loop fragment (Fig. S4). We, therefore, substituted one nucleotide in the tail region to avoid tail interference (binding to the loop region), as shown in

Figure S3. The τMB probe detected the folded 60-nt WT analyte with a S/B of 1.7 and LOD of 19.7 nM after 30 min, but the addition of a tail enabled τMB-Tail to achieve a S/B of 5.2 and LOD of 6.5 nM (Fig. S2 & S5). Moreover, the initial hybridization rates for τ-60 WT were determined to be ~0.030 nM/s and ~0.017 nM/s for the tailed and non-tailed MB, respectively, which reflects a two-fold improvement in hybridization rates for the tailed MB probe (Fig S6). Hybridization experiments with the short τ-17WT analyte revealed comparable S/B and LOD for both MB probes and somewhat slower hybridization rates for MB-tail than for the conventional MB probe (Fig. S5 & S7), which was attributed to the ability of the τMB-Tail to bind two analytes at a time. (Fig. S8). Therefore, the design of tailed MB probes should include in silico analysis of such possibilities.

Selectivity of the Tailed and Non-Tailed MB Probes

Next, we studied the selectivity of the tailed-MB approach. The τMB-Tail probe resulted in a S/B of ~12 for the 0C mutant and ~11 for the 1A mutant, each representing a ~7-fold increase compared to the τMB probe (Fig. S3). In comparison to the τMB probe, the initial rate of hybridization between the τMB-Tail probe and τ-60 analytes were each determined to be ~0.1 nM/sec, representing a 5- and 6-fold increase in the initial rate for the 0C and 1A mutants, respectively (Fig S6). Compared to the τ-60 WT analyte, both mutants produced a higher S/B and a faster initial rate, which can be explained by the differences in secondary structure between the WT and mutant tau analytes (Fig. S3). Both the 0C and 1A mutants adopt a secondary structure that increases the number of unpaired nts complementary to the tail region of the τMB-Tail, thus allowing the τMB-Tail to hybridize more readily. Despite the 2:1 hybridization of the τ-60 analytes with the τMB-Tail (Fig S8), the increase in S/B and initial rate indicates that the advantages in hybridization thermodynamics and kinetics were due to the tail fragment.

Next, we further assessed the effect of SNVs on hybridization thermodynamics and kinetics for the 16S analyte. We chose C/T and G/T substitutions linked to the pathogenic E. coli

strain O157:H7.33 We found that the MB1 probe failed to hybridize to the SNV analytes, but the MB1-Tail produced a robust signal with both SNVs (Fig. S9). This is because a single base mispairing did not contribute significantly to the overall high stability of the MB1-Tail: analyte complexes (both for MB1-tail:16S-60 C/T and 16S-60 C/T; the complexes were destabilized only by ~ 2 kcal/mol in comparison with MB1-tail:16S-60 complex).

Next, we introduced mismatches into the 16S-60 analyte that did not impact the analyte's secondary structure but contained mismatches to either the stem-loop or tail of the MB1-Tail probe to determine which component of the tailed MB probe was more important for hybridization to analyte (Fig. S10). We found that a single mismatch in the region that binds to the MB loop (Loop Mut 1) had a more significant impact on the initial rate and S/B than a mismatch in the tail (Tail Mut 1). In contrast with the 16S-60 WT possessing a S/B of 42.6 and an initial rate of 1.59 nM/sec, we found that the Loop 1 Mut had a S/B of 33 and an initial rate of 0.43 nM/sec, and the Tail 1 Mut had a S/B of 47 and initial rate of 0.92 nM/sec (Fig. S11). When two (Loop 2 Mut) or three (Loop 3 Mut) mismatches were introduced into the loop-binding region, the S/B was decreased to 25 for Loop 2 Mut and to 21 for Loop 3 Mut, and the initial rate was reduced to ~ 0.20 nM/sec for each. When additional mutations were introduced into the tail-binding region, the initial rates and S/B were significantly reduced to 0.03 nM/sec and 24 for the Tail 2 Mut, and 0.01 nM/sec and 13 for the Tail 3 Mut. These results suggest that, although the tailed MB probes readily hybridize with the folded analyte, they could be further optimized for selectivity by modifying the complementarity in the MB tail or stem-loop.

Discussion

MB probes are one of the first and simplest fluorescent molecular switches available.1,2 They have been well-studied and explored in multiple applications.3 However, the design of MB probes is not as straightforward as it seems. The most common complications include stem invasion, stem interference, and loop interference.2 Additionally, traditional MB probes pose a

challenge in detecting folded analytes due to the high energy barrier of unfolding both the probe and the analyte.[21–26] Indeed, the MB probe stem-loop structure disfavours the analyte:MB probe-associated state and thus inhibits complex formation. Earlier, this problem was addressed by developing a universal (near ideal) MB probe in combination with additional analyte-binding arms in the context of multicomponent probes.[34,35]

The tailed MB probe studied here overcomes the challenge of detecting analytes with a stable secondary structure. We observed a ~ 40 and ~ 3 times increase in the S/B and 800- and 2-fold increases in hybridization rates for two independent systems. The latter is particularly important since hairpin probes are known to respond slowly, especially in heterogeneous assays.[28]

Tailed MB probes were not sensitive to single mismatched nucleotides. This observation agrees with the affinity selectivity dilemma, which states that hybridization probes with high affinity have low selectivity.[36] Tailed MB, however, significantly reduced their responses in the presence of 2 or 3 mismatches, especially if the mismatches were complementary to the tail region of the probe. This opens the possibility of applying Tailed MB probes in mutation-tolerant assays, for example, for detecting viral RNA folded in stable secondary structures and prone to mutagenesis. Adopting the approach to hairpin hybridization probes used in heterogeneous formats[37,38] may significantly reduce the time for hybridization assays and make them practically useful.

Conclusion

MB probes equipped with additional ‘tail’ fragments complementary to an accessible fragment of nucleic acid analytes can improve both S/B and hybridization rates. At room temperature, such probes are not sensitive to single nucleotide substitutions but sensitive to double and triple nucleotide substitutions, which makes them a promising tool for the analysis of

mutation-probe biological nucleic acids. This hairpin probe strategy is promising for reducing the time of hybridization assays.

CHAPTER FOUR (Part I): OWL2: A MOLECULAR BEACON-BASED NANOSTRUCTURE OF THE HIGHLY SELECTIVE DETECTION OF SINGLE NUCLEOTIDE VARIATIONS IN FOLDED NUCLEIC ACIDS

Reproduced with permission from Mueller, B.L.; Liberman, M.J.; Kolpashchikov, D.M. OWL2: A Molecular Beacon-Based Nanostructure for the Highly Selective Detection of Single Nucleotide Variations in Folded Nucleic Acids. *Nanoscale*, 2023, **15**, 5735. Copyright 2023 The Royal Society of Chemistry.

Introduction

In the traditional MB probe design, the MB probe is directly complementary to the analyte and can only discriminate against SNVs at higher temperatures (Figure 18A). In contrast, the OWL1 sensor was designed to differentiate SNVs at ambient temperatures (Figure 18B).[149] The OWL1 sensor is an MBP-based sensor that forms a four-stranded complex in the presence of the analyte. In the OWL structure, the strands P and R hybridized to the analyte adjacent to each other and cooperatively open the UMBP hairpin. While the R strand forms a perfect 10-nt hybrid with the analyte, the P strand only possesses 9-nts. Therefore, a single-base mismatch readily destabilizes the complex because a mismatch represents ~ 10% of the ΔG associated with the analyte/sensor duplex.

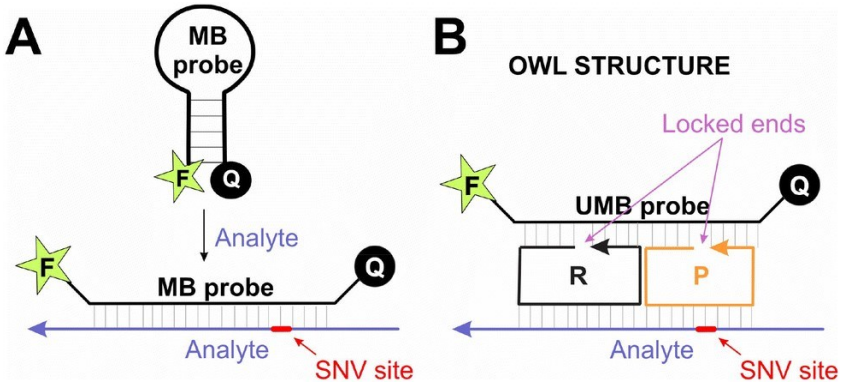

Figure 18 MB Probe and Design of OWL1 Sensor. (A) MB Probe hybridizing with analyte. (B) OWL1 Sensor forms a 4-stranded fluorescent OWL structure only in the presence of the matched analyte. The Universal MB probe (UMB) is not dependent on the analyte's sequence and can be used universally.

Indeed, the OWL1 sensor differentiated SNVs in the 5–32 °C range with single-base mismatched analytes producing only background fluorescence.33 Importantly, at least in part, this unprecedented SNV selectivity was attributed to the unique rigid OWL nanoscale structure: both strands P and R must fold in 'circular' forms with 3′- and 5′-terminal base pairs being in stacking interactions with each other, thus creating a structural lock ('locked ends' in Fig. 1). This feature of the nanoscale structure makes the OWL sensor structurally constrained and less tolerant to mismatches in comparison with other hybridization probes that possess 'unlocked' ends (e.g. MB probe in Fig. 1A).[149] Adjusting the OWL1 sensor to each new analyte requires changing only unmodified DNA strands P and R, and the same MB probe can be used for the analysis of any nucleic acid sequence. This allows for an opportunity to optimize only one universal MB (UMB) probe, which reduces the optimization efforts and the assay cost in comparison with the MB probe approach if multiple sequences are to be detected.

However, the OWL1 structure was too 'fragile' to form a complex with RNA or ssDNA analytes folded in stable secondary structures. This left us with a question: how can we extend the application of the OWL sensor approach toward folded nucleic acids?

Results and Discussion

OWL2 Design and Performance

To overcome the limitations of the OWL1 sensor, we designed the OWL2 sensor **(Figure 19)**. It also uses the UMB probe and P strand, but the free R strand of OWL1 was replaced with an association of DNA strands T1, T2, T3, and T4. The R strand was attached via a trithymidine linker to a fragment complementary to T1. Strands T2 and T4 contained long analyte-binding arms, and T1 provided scaffolding for the complex formation. Together with R strand, the arms of T2 and T4 hybridized to the folded analyte and opened its secondary structure. The association of R, T2, and T4 with the analyte did not result in fluorescent signaling unless the P strand was

selectively hybridized with the SNV-containing site of the analyte and completed the OWL structure by allowing for the binding and subsequent opening of UMB.

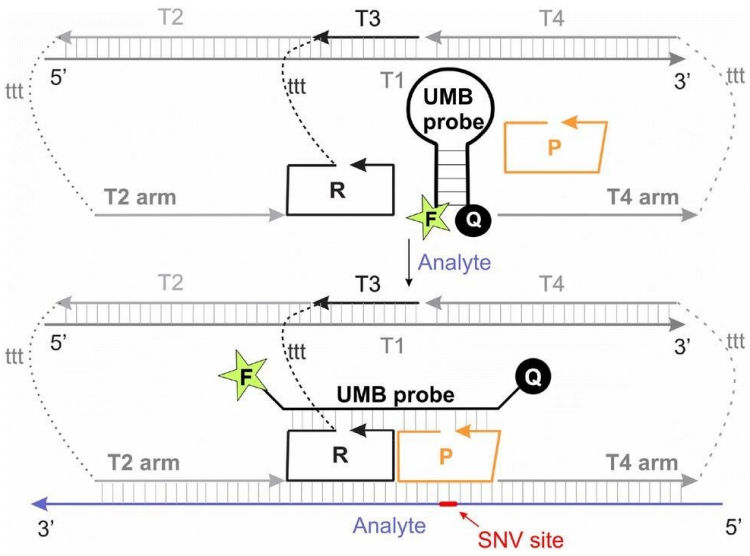

Figure 19. Design of the OWL2 Sensor. OWL2 sensor consists of a P strand, UMB probe, and an association of T1, T2, T3, and T4 strands (top). The strands form a fluorescent structure, even in the presence of folded analytes (bottom)

As a model analyte for the initial optimization of the OWL2 sensor, we chose SNV '0C' and '1A' (Fig. 3A and Table S3†) found in the tau gene. These SNVs can lead to an increase in alternative splicing of exon 10, skewing the ratios of tau protein isoforms and causing Alzheimer's Disease (AD).[150,151] The secondary structures of synthetic fully matched analytes Tau60-WT and Tau18-WT are shown in Fig. 3A. The total energy of folded Tau60-WT is −11.34 kcal/mol, with the SNV-containing stem contributing to much of the stabilization.[151] It is important to note that the MB probe designed against the Tau analyte failed to produce a fluorescent output.[143] Tau18-WT was designed to be fully complementary to strands P and R, but lacked the T2 and T4 binding sites. This short oligonucleotide formed a weak stem-loop structure, thus resembling a linear analyte under experimental conditions (Fig. 3A), and was used to study the effect of T2 and T4 arms on the sensor's performance.

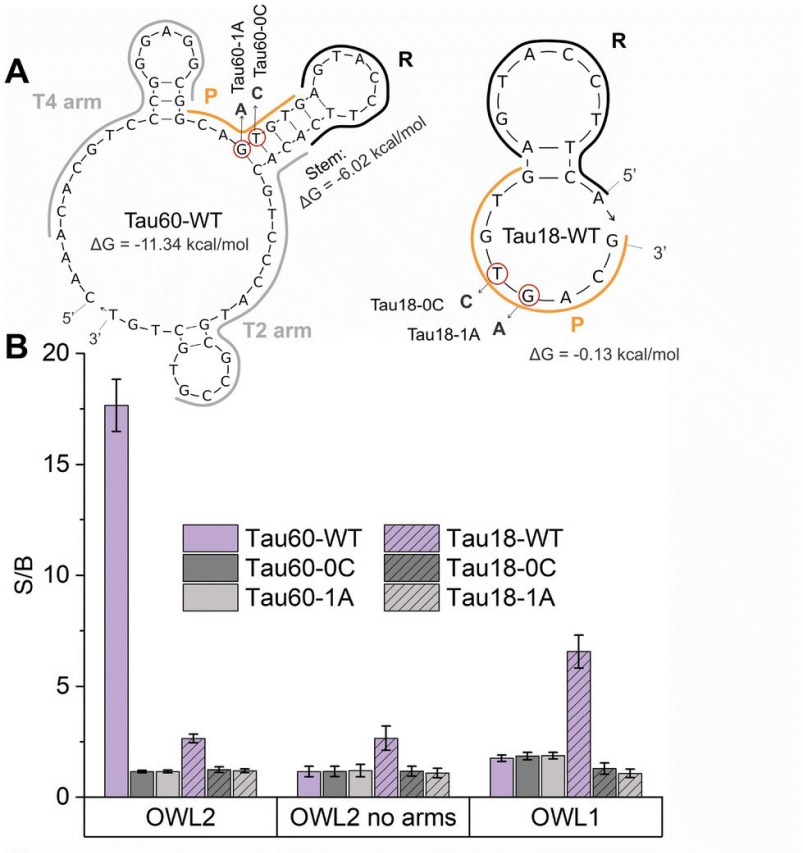

C

Design	S/B (Tau60) WT	0C	1A	D_f* 0C	1A
OWL1	1.76	1.86	1.87	-0.13	-0.15
OWL2	17.7	1.2	1.2	0.99	0.99
Armless OWL2	1.16	1.16	1.20	-0.02	-0.27

*$D_f = 1- (\Delta F_{mm}/\Delta Fm)$

Figure 20. SNV differentiation in Tau analytes. **(A)** The secondary structures of Tau60-WT and Tau18-WT analytes as predicted by NUPACK.[152] The SNV sites are circled red, and the regions of OWL2 hybridization (P/R/T2 and T4 arms) are outlined around their structure. **(B)** OWL2 sensor (UMB, 25 nM; P98, 200 nM; T1/T2/T3/T4 association 100 nM, in the hybridization buffer 1: 50 mM Tris-HCl, 50 mM MgCl2, 0.1% Tween-20, pH 7.4) was incubated with 100 nM Tau60-WT (purple) or Tau18-WT (striped, purple) or corresponding single-base mismatched analytes (grey). The data is the average of three independent measurements. **(C)** Differentiation table for Tau60 (folded) analytes with the formula for the differentiation factor, Df, where ΔF represents the difference between the measured signal and the blank.

The binding site of the P strand was chosen such that the two SNV sites corresponded to the middle positions of the strand for best SNV differentiation.[149] The analyte-binding site for the R strand, adjacent to the P strand binding site, formed a 10 base-pair (bp) duplex with the analyte and enabled both UMB-binding arms of the R strand to be positioned on the same side of the B

DNA helix as needed for the formation of OWL structure.[149] The T2- and T4-arms were chosen to have melting temperatures above the assay temperature (24 °C) and to have little or no secondary structures to ensure tight analyte association with the OWL nanostructure.

We optimized the concentration and sequences of the P strand to produce the highest signal-to-background ratio (S/B) and the greatest SNV differentiation (see details below). The optimal P strand had 9 nts and 8 nts complementary to the UMB probe and the analyte, respectively, and was, therefore, named P98. It was used at a concentration of 200 nM, which provided the highest S/B (Fig. S1†). The optimized OWL2 sensor (Fig. S2C†) produced a S/B of ~18 and maintained excellent selectivity that the OWL1 sensor exhibited for unstructured analytes (Fig. 3B). It was able to differentiate Tau60-WT from single-base mismatched Tau60-1A and Tau60-0C in the temperature range of 5–38 °C (Fig. S3†). This range is shifted toward low temperatures and almost 2 times broader than that for a typical MB probe that differentiates analytes with single base difference in the range of e.g. (53–70 °C).[54] The LOD for the folded Tau60-WT using OWL2 sensor was ~0.4 nM (Fig. S5†), which was lower than that of the short Tau18-WT with OWL1 sensor (~1.3 nM, Fig. S2B†), and falls in the range of LODs demonstrated by the best MB probes in detecting unfolded analytes.[98] To the best of our knowledge, this combination of high S/B and excellent selectivity in detecting folded analytes (Fig. 3B, 1st group of bars) is unprecedented.

Next, we demonstrated that each feature of the OWL2 sensor contributes to at least one of the following functions: (1) enabling detection of folded analytes and (2) accurate discrimination of SNVs, (3) maintaining detection efficiency and selectivity over a range of ambient and low temperatures, and (4) ensuring low reagent cost due to “universality” of the UMB probe.

T2 and T4 arms are necessary for the detection of the folded Tau60-WT analyte

The removal of the T2- and T4-arms resulted in a loss of the OWL2 ability to detect the folded Tau60-WT (Fig. 3B, bars grouped as “OWL2 no arms”), which mimicked the sensing capabilities of OWL1 (Fig. 3B, bars grouped as “OWL1”). The inclusion of arms decreases the energy barrier for hybridization to folded DNA sequences and allows for the opening of their secondary structures. Interestingly, OWL1 produced a lower signal with Tau18-WT than OWL2 in the presence of Tau60-WT (Fig. 3B). This suggests that an important function of T2 and T4 arms is not only to remove the structural constraint in the Tau60-WT structure but also to position the analyte next to the R strand for tighter binding. Therefore, T2 and T4 arms are likely to stabilize the OWL structure by increasing the local analyte concentration in proximity to the R strand.

On the other hand, OWL1 in complex with Tau18-WT produced a greater S/B than OWL2 lacking sensor T2 and T4 (“OWL2 no arms”) (Fig. 3B). This can be explained by the reduced attraction of Tau18-WT to the bulky OWL2 nanostructure due to electrostatic repulsion. At the same time, the OWL1 sensor expectedly failed in detecting the folded Tau60-WT analyte (Fig. 3B). Therefore, we were able to conclude that the T2- and T4-arms are necessary for the detection of analytes folded in stable secondary structures.

Flexible linkers between strand R and the DNA scaffold enable higher S/B

Positioning of the fragile OWL structure near a bulky DNA scaffold formed by T1, T2, T3 and T4 in the OWL2 sensor might be challenging due to steric hindrance, which is hard to predict without knowing the crystal structure of the OWL2 sensor. We varied the nature of the linker between the R strand and the scaffold-forming fragment of the T3 strand ranging from the least flexible regular phosphodiester (PDE) linkage to more flexible trithymidylate (ttt) and hexaethylene glycol (iSp18) linkers (Fig. S4 and S5†). For the experiments with P99, we found that an increase in linker flexibility resulted in a mild increase in fluorescence for both mismatched and matched

analytes (Fig. S4†). In the case of P98, increased flexibility of a linker allowed for an increase in S/B for the fully matched analyte from ~14 (PDE) to ~18 (ttt) and to ~25 (iSp18) without compromising the selectivity (Fig. S5†). Therefore, the S/B reported above for the optimal sensor can be increased from 18 to 25 by replacing the ttt linker with the iSp18 linker. This indicates that a spatial separation of the R strand from the scaffold is important for the stability of the OWL structure. The increase in S/B did not, however, change the LOD of the sensor (Fig. S5C†). In this work we, therefore, considered the increase of S/B for the iSp18 linker a minor advantage in comparison with the lower cost of the ttt linkers and conducted most of the experiments using the ttt linker equipped OWL2 sensor.

Structural constraint in the OWL structure promotes high selectivity of the OWL sensor

Following our previous results,[149] we hypothesized that the unprecedented SNV differentiation, at least in part, is the consequence of the conformational strain ensured by the OWL structure and the locked ends of the P strand (Fig. 1B).

First, we redesigned the optimal P98 strand to have opened ends, named C98 strand (Fig. 4A and Table S2†). Like all known probes, except the OWL sensor, C98 strand had 5′ and 3′ ends unlocked: they were free to acquire any position relative to each other. The fluorescence of the C98-containing OWL2 was found to be higher than that of the P98-equipped sensor. However, the sensor lost its selectivity (Fig. 4B and Table 1). Furthermore, the substitution of P98 with P99 also diminished SNV differentiation and increased the overall fluorescent response (Fig. 4B). The observed increase in fluorescence can be explained by the greater flexibility of the C98- or P99equipped OWL2 sensor (see Discussion for more details).

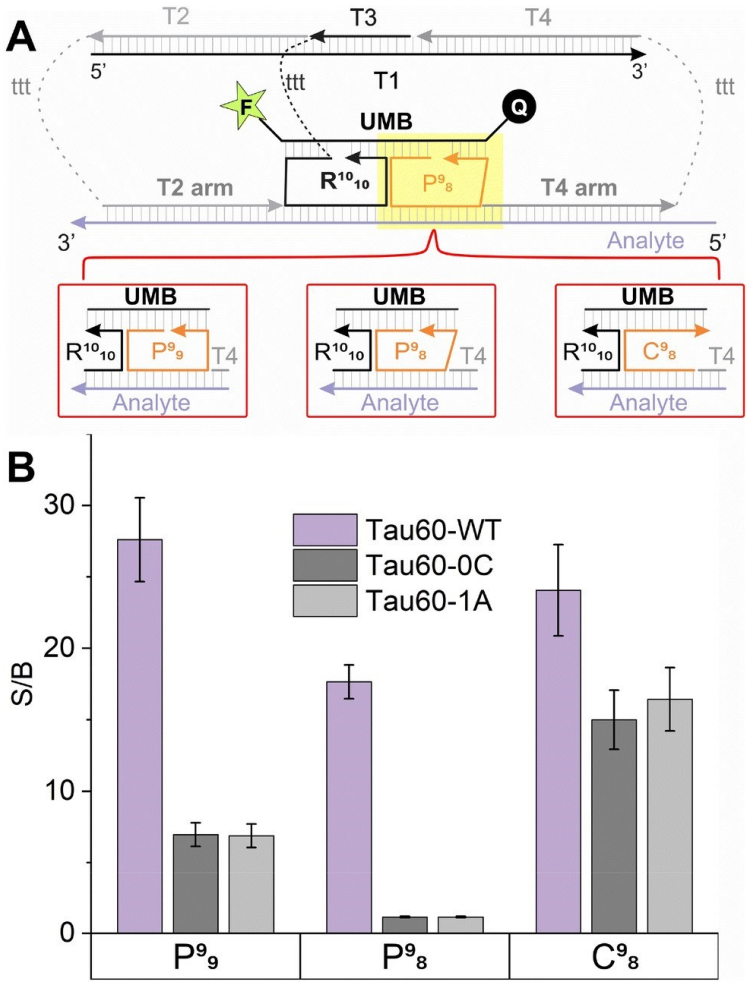

Figure 21 OWL2 equipped with P98 strand was the most selective. (A) OWL2 design with changes in the highlighted region depicted below the OWL2 structure. P99 contains 9 nt complementary each to UMB and the analyte; P98 contains 9 nt complementary to UMB and 8 nt complementary to the analyte. C98 has the UMB- and analyte-binding arms of similar length as P98. (B) S/B of the OWL2 sensor containing different SNV-specific stands in the presence of 100 nM fully matched Tau60-WT or Tau18-WT (dark grey bars) or single-base mismatched analytes (light grey bars). The data is an average of three independent measurements.

Next, we tested whether the flexibility of the R-strand affected selectivity and S/B. For this purpose, we introduced an iSp18 spacer between the UMB-hybridizing and analyte-hybridizing regions of R1010 near its 5′-end (Fig. S6A†). We used this flexible R1010 strand with P98 and found that the S/B changed insignificantly with a noticeable reduction in SNV differentiation (Fig. S6B† and Table 1). Indeed, the differentiation factor (Df,[120]Table 1) decreased from 0.99, which corresponds to a 100-fold higher fluorescent signal of the matched analyte being than that of the

mismatch, to 0.96 (25-fold ratio between the signals triggered by the matched and mismatched analytes). This data suggests that the structural constraint of the R strand has a lower effect on the OWL2 sensor performance than the constraint contributed by the P strand.

Table 1 Signal-to-background ratio (S/B) and differentiation factor (Df) for the OWL2 sensors containing three variations of the P strand. Df = 1 − ΔFmm/ΔFm, where ΔF represents the signal of matched (m) or mismatched (mm) analyte with the signal of the blank (no analyte) subtracted.[120]

Design	**S/B**			**Df**		
	WT	**1A**	**0C**	**1A**	**Free Strand**	**0C**
P98	17.7	1.2	1.2	0.99	0.99	
P99	27.6	7.0	6.9	0.78	0.78	
C98	25.1	15.0	16.4	0.4	0.33	
R10, iSp18	17.9	1.6	1.7	0.96	0.96	

Indeed, the constrained and rigid nature of the SNV-selective P-strand contributes the most to the differentiation of WT from the mutants. By designing the P-strand with locked 5′- and 3′-ends in complex with UMB, we created a conformational strain that cannot remain stable unless all 8 base pairs are complementary to the analyte. In the presence of a mismatch, the strain experienced by P98 is great enough to inhibit P-strand hybridization to the analyte, which decomposes the OWL complex. If there are no mismatches, the P-strand is stabilized by the 8 base pairs complementary to the analyte, the stress of the conformational strain is insufficient to cause dissociation of the P-strand, and the scaffolding for UMB hybridization is complete.

Gap effect and P-strand optimization

Previous studies have shown that the stability of multistranded DNA complexes are affected by the distance between adjacent DNA strands hybridized to a complementary nucleic acid.38–40 Therefore, we introduced a single nucleotide gap between the P-strand and T4-arm. The introduced gap did not significantly affect the S/B or DF of the optimal sensor containing P98 (Fig. S5 and S7†). This indicates that the stability of the OWL structure does not depend on the staking interaction with the flanking T4 arm. However, we noticed a loss in the S/B or selectivity for the OWL2 sensor equipped with other P stands (Fig. S8 and Table S4†). Some of these undesired effects were explained by interaction of the P strand with the gap-forming nucleotide of the analyte (see comments to Fig. S8†). We, therefore, concluded that OWL2 without a gap between P and T4 arm is preferable.

Detection of WT analyte in the presence of mismatched analyte

It was interesting to investigate if the excellent selectivity of the OWL2 sensor allows the detection of the matched analyte in the presence of excess amounts of a mismatched analyte. This sensor capability would be useful for detecting small fractions of cancerous DNA in excess healthy DNA for early-stage cancer diagnosis.[50] We measured the LOD of the fully matched Tau60-WT analyte with the optimal OWL2 sensor in the presence of 50 nM Tau60-0C as a buffer component (Fig. 5). The LOD was found to be 0.4 nM, the same as in the absence of the mismatched analyte. This result indicated that the OWL2 sensor can differentiate from singlebase mismatches and detect the fully matched analyte even when it makes up only 0.8% of the total analyte, which is comparable with the state-of-the-art fluorescent sensors.[50,153] An increase of the mismatched Tau60-0C analyte to 500 nM required an increase in the OWL2 (T1/T2/T3/T4) to 600 nM and a decrease in P98 to 50 nM in order to offset some of the background fluorescence. We found that the concentration of analytes should not exceed our OWL2 (T1/T2/T3/T4 association) sensor concentration, likely due to the hybridization of T2- and T4-arms to analyte, even when it

contains a mismatch. Due to high OWL2 concentration, the background fluorescence was high, which resulted to high LOD of ~8 nM (Fig. 5). Therefore, further sensor optimization is needed to improve the detection of low fractions of the true targets in the presence of single base mismatched analytes.

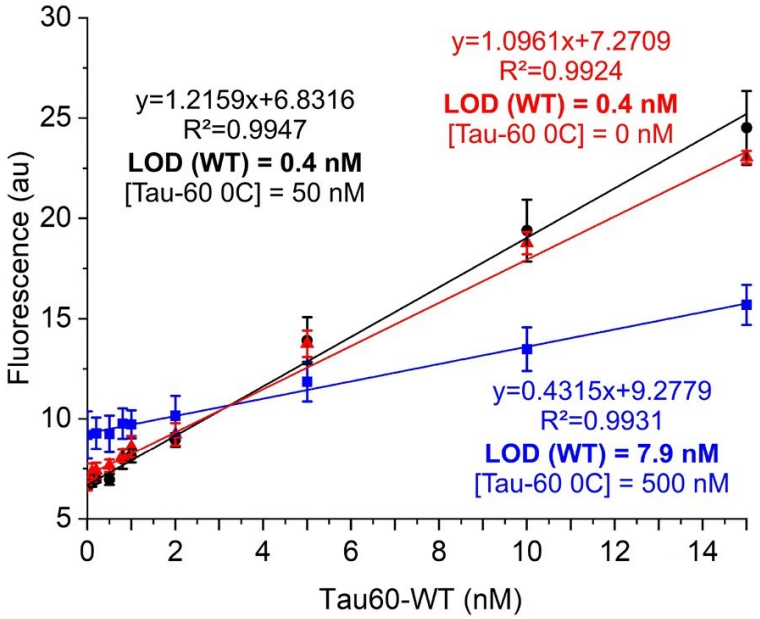

Figure 22. OWL2 sensor detects the fully matched analyte in ~125 times excess of single-base mismatched analytes. The limit of detection of the Tau60-WT analyte in the presence of 50 nM Tau-60 0C (black line) is 0.4 nM, which is the same as the LOD in the absence of mismatch (red line) and corresponds to a detection in the presence of 125× mismatch; 100 nM OWL2 (T1/T2/T3/T4), 25 nM UMB15, 200 nM P98 in hybridization buffer 1 (50 nM and 0 nM Tau60WT). The limit of detection of Tau60-WT analyte in the presence of 500 nM Tau60-0C (blue line) is 7.9 nM, corresponding to a detection in the presence of 60× mismatch with an increase in sensor concentrations; 600 nM OWL2 (T1/T2/T3/T4), 25 nM UMB15, 50 nM P98 strand.

G:T discrimination

G–T mismatches are known to be the least destabilizing of all base-mispairing scenarios and, therefore, the most challenging to discriminate.42,43 Here, we investigated if the OWL2 sensor can differentiate an analyte that forms a single G–T mismatch with the sensor. We found that P98 has Df of 0.45 when tested against the Tau60-2G analyte, which has an A > G substitution (Fig. 6C and Fig. S9D† for structure). We also tested the effect of two other G–T mismatches by

changing the sequence of the P-strand: P98 A > G and P98 C > T (Fig. 6B and Table S2†) had full complementarity to the Tau60-0C and Tau60-1A analytes, respectively. They were able to discriminate against G–T mismatches with a Df of 0.84 and 0.98. (Fig. 6).

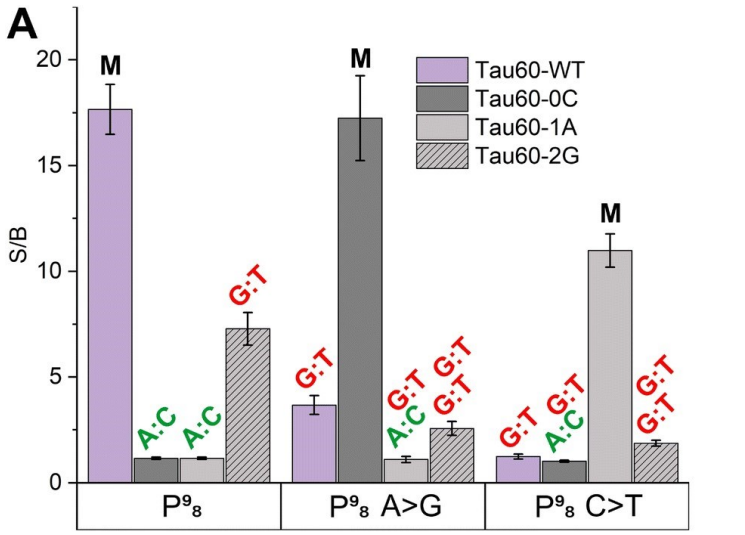

C

Design	S/B (Tau60)				D_f			
Free Strand	"WT"	0C	1A	2G	"WT"	0C	1A	2G
P^9_8 (normal)	17.7	1.2	1.2	7.2	---	0.99	0.99	0.45
P^9_8 (A>G)	3.7	17.2	1.1	2.6	0.84	---	0.99	0.90
P^9_8 (C>T)	1.2	1.0	11.0	1.9	0.98	0.99	---	0.91

Figure 23 Discrimination of G:T mismatches. (A) S/B response of the OWL2 sensor to the presence of 100 nM fully matched (M) or mismatched analytes (A:C and G:T) as indicated above the bars. The data is the average of three independent measurements. (B) Sequences of the P-strand and analytes with changes in the P-strand highlighted in black and the analytes shown below, complementary to the P strand. A:C mismatches are highlighted in green and G:T mismatches are highlighted in red. (C) Tabulated S/B and Df values for each analyte. Tau60-WT is denoted "WT" in the table, but it is only fully complementary to the normal (unsubstituted) P98.

Discrimination using the original P98 was expectedly poor since the G–T was situated between the two stable G–C base pars and shifted from the middle of the stand P-analyte hybrid. Mismatches on the ends of hybridization sites are known to be less destabilizing than those in the center.32,33 Expectedly, the mismatches closer to the center (P98 A > G and P98 C > T) were

better discriminated. However, P98 C > T had a greater A/T content, possibly leading to the best discrimination of the three. We show that, through modification of the P-strand, we can differentiate even G–T mismatches, with the best discriminating ability of the sensors containing G–T mismatch in the middle position of stand P/analyte complex and when flanked by A–T base pairs (Fig. 6A, 3rd group of bars).

Detection of RNA analyte

Since RNA/DNA helical structure characteristics are somewhat different due to the difference in ribose and deoxyribose conformation,[44] we investigated if the same OWL-2 sensor that performs well with DNA analytes is suitable for detecting an RNA analyte. We found that the OWL2 sensor equipped with P98 strand could detect Tau60-WT RNA at a LOD of 0.8 nM, comparable to the 0.4 nM LOD of Tau-60 DNA (Fig. S12†). The ability of the OWL sensor to detect RNA may have practical significance since Tau-60 DNA is associated with the development of Alzheimer's disease.[35,36]

OWL2 sensor can be redesigned for another analyte in a cost-efficient manner

To ensure that OWL2 can be easily redesigned for other analytes, we applied it to a sequence from the Covid-19-causing SARS-CoV2 virus. By only changing the analyte-binding portions of T2, T3, T4, and P-strand (named CP-strand for Covid-19), we were able to show that both CP98 and CP99 allowed for differentiation of the fully matched CVD60-WT from the mismatched CVD60-1C and CVD60-0Ganalytes (Fig. 7). We found this to be juxtaposed with the Tau-specific OWL2 sensor, which was not specific when equipped with P99. The A/T-rich sequence complementary to CP99 in CVD60-WT could explain this different sensor behavior. We speculate that if the P-strand binding region is A/T rich, the P99 may still provide selectivity. However, this statement should be verified with other sets of analytes.

Overall, these results show that the OWL2 design can be easily adapted to detect another analyte without costly changes. The cost of one nucleotide addition in IDT Inc. is $0.42 (minimum synthetic scale), which comes to 56.7 USD for adapting T2, T3, T4, and P-strand to each new analyte. At the same time, the cost of a new MB probe is ~350 USD (minimum synthetic scale) due to the need for conjugation of the oligonucleotide with two dyes and double HPLC purification. Additionally, the design of an MB probe for each new analyte is associated with many problems, such as stem invasion and loop interference, to the degree that it is impossible to design an efficient MB probe for some analytes.28,32 By designing the UMBhybridizing regions of R- and P-strands to be independent of the analyte sequence, we allow the UMB technology to be applied for analytes of potentially any sequence. Furthermore, we showed that OWL2 design applies to both DNA and RNA analytes that contain an SNV in both the stem and the loop regions (Fig. S9 and S10†).

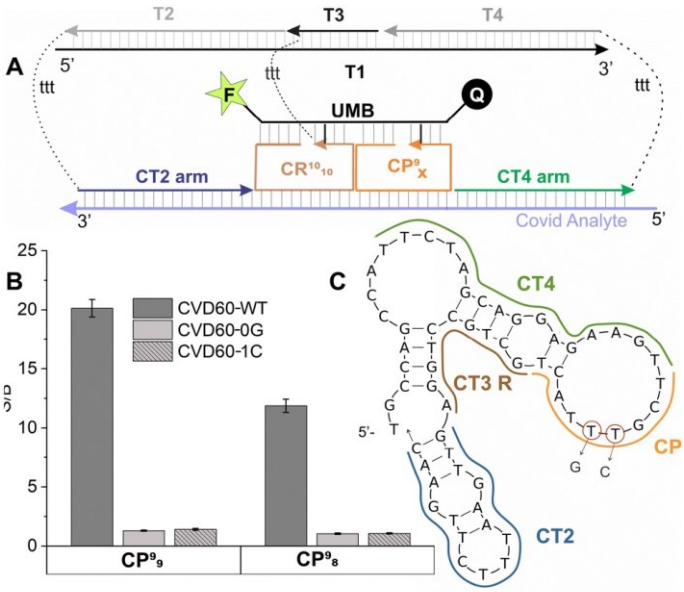

Figure 24 OWL2 Sensor differentiates SNVs in Covid-19-related sequences. (A) OWL2 sensor adapted for detection of Covid-19 analyte; T1 and UMB remain unchanged. (B) S/B for the OWL2 sensor with 200 nM CP98 and CP99 in the presence of 100 nM analyte. (C) Secondary structure

of Covid-19 WT used in this study. T > G and T > C mutations are indicated by red circles. (D) Values for S/B and Df for each analyte.

Conclusion

The OWL2 sensor shines where most hybridization probes fall short. The remarkable characteristics of the sensor include a S/B of 18 and LOD in the sub-nanomolar range both for DNA and RNA analytes. It has an extraordinary ability to differentiate mismatched analytes from the fully matched ones, including the most challenging G–T mismatches in the temperature range of 5–38 °C. Despite looking complex, the sensor is cost-efficient when applied to new analytes. The UMB reporter, the most expensive and hard-to-design component, is analyte-independent, and it can be optimized once and then used to analyze any DNA or RNA sequences. These features make the OWL2 sensor a highly specific, selective, and versatile tool that seeks to improve the field of hybridization assays.

CHAPTER FOUR (Part II): THE APPLICABILITY OF THE OWL2 SENSOR FOR THE DETECTION OF MUTANT ANALYTES MIXED SAMPLES

Introduction

Previously, we had only tested our OWL2 sensor with a single type of analyte, either mutant or wild-type. To make our sensor more applicable to real clinical samples, we explored whether our sensor could detect small concentrations of pathogenic (mutant) EGFR gene in the presence of an excess of wild-type.

Results and Discussion

CHAPTER FIVE: A MOLECULAR BEACON PROBE-BASED DNA NANODEVICE WITH A CONCENTRATION THRESHOLD FUNCTION (MB-TH)

Introduction

Current methods to detect the over- or under-expression of miRNA include nanopore decoding, northern blot analysis, reverse transcriptase-quantitative polymerase chain reaction (RT-qPCR), and liquid hybridization assays.[154–157] To overcome the cost associated with these assays, we created a multicomponent sensor that responds hierarchically to an input of discrete amounts of target.

Sensor Design

The fluorescent threshold sensor (FTh) is composed of a rail strand (Q-rail), which provides the scaffolding for gate strands 1A and 2A while simultaneously allowing for the quantification of FTh due to the inclusion of a ROX fluorophore (Figure 25). When fully complexed with two equivalents of the analyte, oligonucleotide strands 1B and 2B come from the solution and form a non-classical four-way junction with a universal molecular beacon probe, analyte, and 1A and 2A.

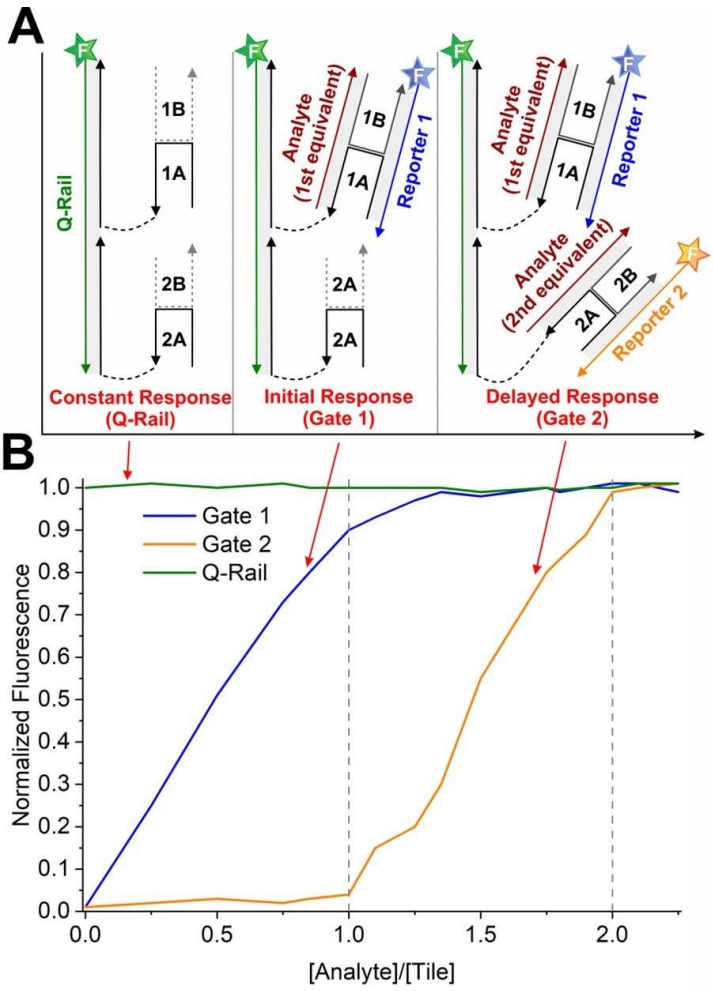

Figure 25. Threshold Sensor Design. **A)** The threshold sensor comprises a Q-rail and attached strands 1A and 2A. Upon hybridization to one equivalent of the analyte, subsequent hybridization of 1B and Reporter 1 occurs. An additional equivalence of analyte results in the hybridization of 2B and Reporter 2. **B)** Ideal response of the Threshold Sensor: Gate 1 results in an increase in signal from Reporter 1 until the first equivalence is reached. After one equivalence

fully hybridizes with Gate 1, Gate 2 begins responding via Reporter 2. The Q-rail is not quenched and results in a constant signal, allowing for sensor quantification.

The sensor is designed such that Gate 1 (1A and 2A) has lower free energy than Gate 2 (2A and 2B), and the analyte should first hybridize with Gate 1, leading to the concentrationdependent increase in fluorescence from Reporter 1 (Figure 26). When the ratio of analyte to tile surpasses 1:1, Gate 2 will respond in a delayed fashion via Reporter 2 (Figure 25).

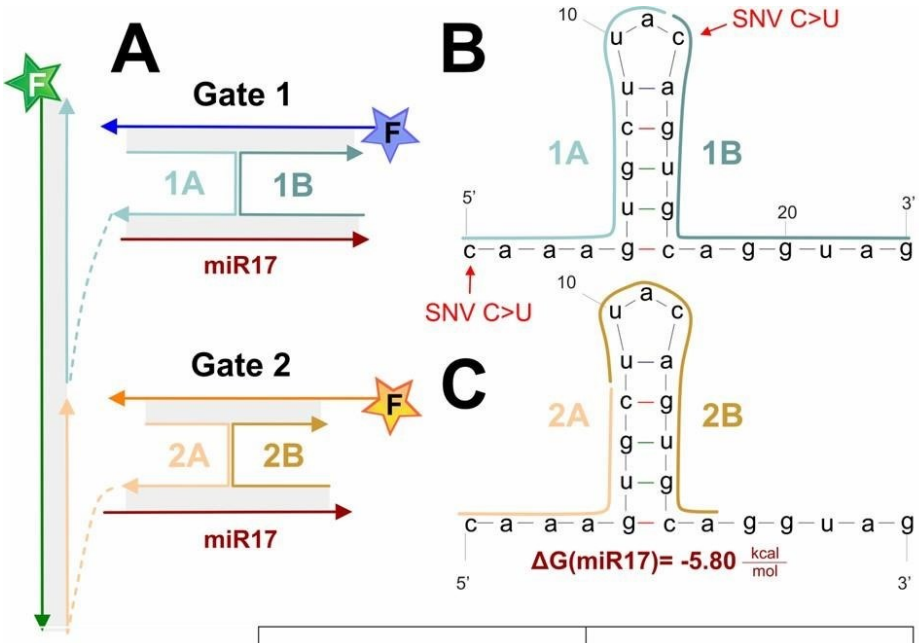

D

	Gate 1			Gate 2		
	1A	**1B**	**Sum**	**2A**	**2B**	**Sum**
ΔG RNA/RNA duplex (kcal/mol)	-19.46	-27.95	**-47.41**	-14.77	-19.56	**-34.33**
ΔG DNA/DNA duplex (kcal/mol)	-17.29	-19.84	**-37.13**	-12.71	-16.00	**-28.71**

Figure 26. Free energies of FTh and analyte. **A)** Design of FTh colored to match strands shown in panel B and C. **B)** structure of miR17 with analyte-binding regions outlined in light blue (1A) and dark blue (1B) along with identification of two SNVs corresponding to miR20. **C)** The structure of miR17 and its ΔG, with 2A and 2B analyte-binding regions outlined in light and dark yellow, respectively. **D)** The ΔG values for the hybridization between gate strands and the complementary sequence corresponding to miR17 were found using NUPACK15 and Mfold web server16 at 22 °C.

Results and Discussion

Sensor Performance

To determine the functional range of our sensor, we explored FTh concentrations from 10100 nM with analyte concentrations ranging from 0 to approximately two equivalents of FTh. We found that, although Gate 1 responded immediately to an input of analyte, the increase in signal of Gate 2 was delayed almost until after the first equivalence of analyte was added (Figure 27C).

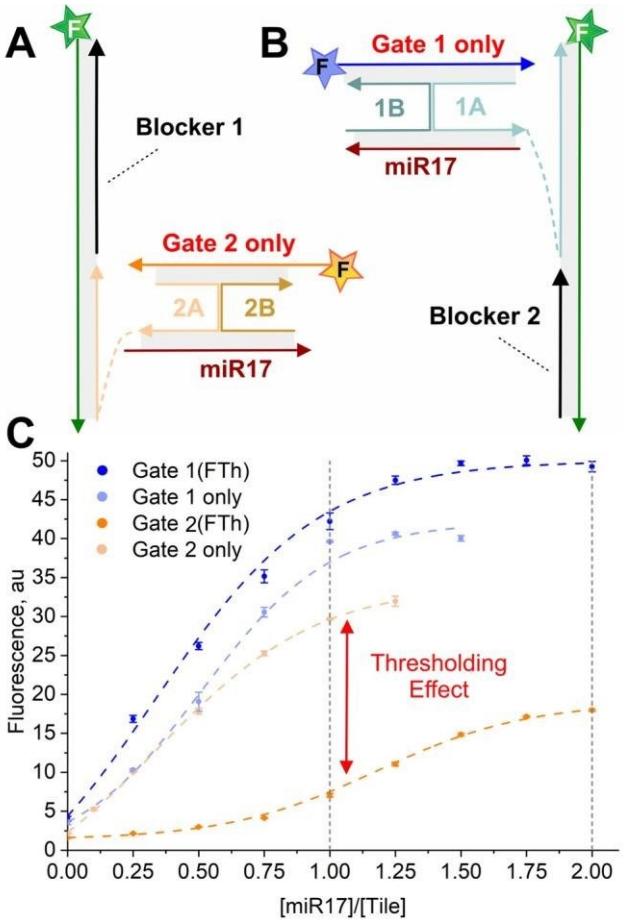

Figure 27. Demonstration of Thresholding Effect. **A)** Sensor with only Gate 2. **B)** Sensor with only Gate 1. **C)** Concentration dependence of the individual gates (light blue and light orange), and with both Gate 1 and 2 on the same sensor (dark blue and dark orange), as shown in Figure 26.

We further investigated the importance of ΔG on our thresholding sensor by comparing the response with the DNA sequence corresponding to miR17 (miD17). The ΔΔG between Gate 1 and 2 was 13.1 kcal/mol for the RNA/RNA duplex and 8.4 kcal/mol for the DNA/DNA duplex (Figure 26C). We found that the reduced difference in the Gate 1 and 2 ΔG resulted in a loss of the thresholding function; Gate 2 responded earlier and Gate 1 responded over a range from 0-1.5 equivalents of analyte to FTh (Figure 28).

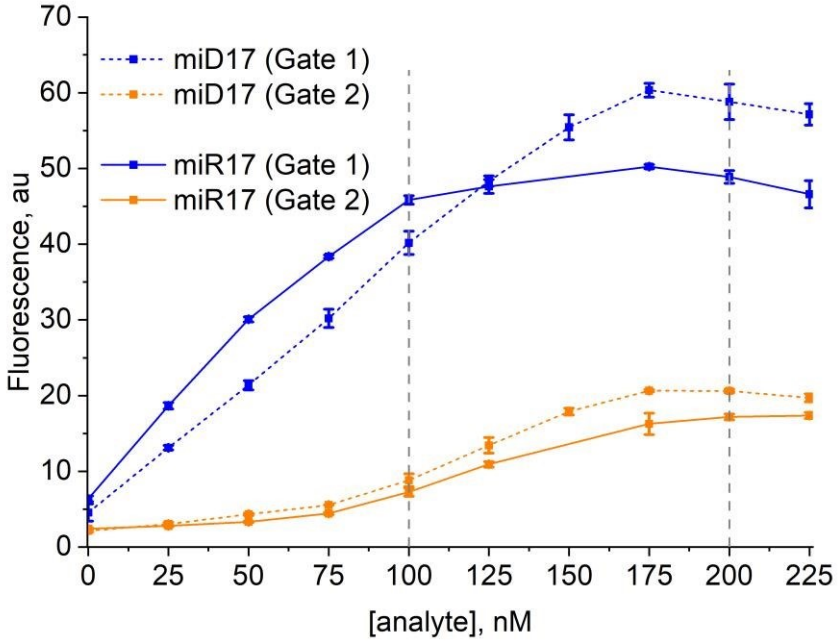

Figure 28. Threshold Sensor Response to miR17 and miD17. RNA analytes (solid line) maintained the thresholding function, but the DNA analytes did not.

Analyte Quantification

To quantify the amount of analyte present in a sample using our sensor, we derived a relationship between the responses at different [FTh]. A line of best fit was created in OriginLab using a Dose-Response fit (Equation 1).

$$y = A1 + \frac{A2 - A1}{(1 + 10^{(log x0 - x) * p})} \quad (1)$$

The associated parameters were then plotted against the concentration of FTh and equations were derived from these relationships (SI info). Using these equations, we could determine the concentration of miR17 in a sample by using the fluorescent values of our three fluorophores after background subtraction and normalization with the maximum fluorescence of each. Although the equations worked for the concentration ranges that we tested, variations in the measurements and fitted equations resulted in a large uncertainty when determining concentrations.

Sensor Kinetics

Next, we assessed the kinetics of our sensor to determine differences between FTh (on tile) and the free strands (in solution). We found that, upon the addition of less than one equivalent of the analyte, the hybridization of the target with gate 1 occurred more quickly with the tile system, and after five minutes, the FTh association with miR17 at Gate 2 was less than that of the free strands (Figure 29).

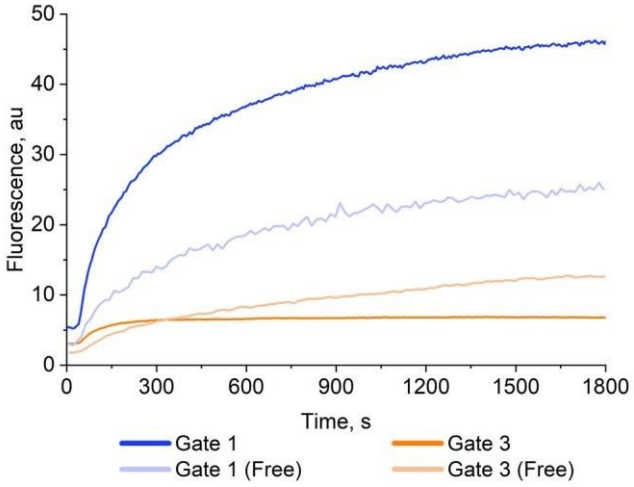

Figure 29. Kinetics of FTh on-tile & off-tile with 100 nM miR17. The fluorescence of FTh on tile shows improved kinetics for Gate 1 and shows a diminished increase in fluorescence for Gate 2 when compared to the free strands.

Sensor Selectivity

MiRNAs within the same family have high sequence similarity, typically differing in one or two nucleotides. Therefore, the ability to discriminate between miRNAs within the same family is important to reduce false positives. The sensor was challenged with selectivity by testing the response against miR20, which contains two C>U mutations (Figure 26). We found that Gate 3 was essentially non-responsive to this target, and Gate 1 response was significantly diminished, only achieving ~40% of its maximum fluorescence at 100 nM FTh (Figure 30).

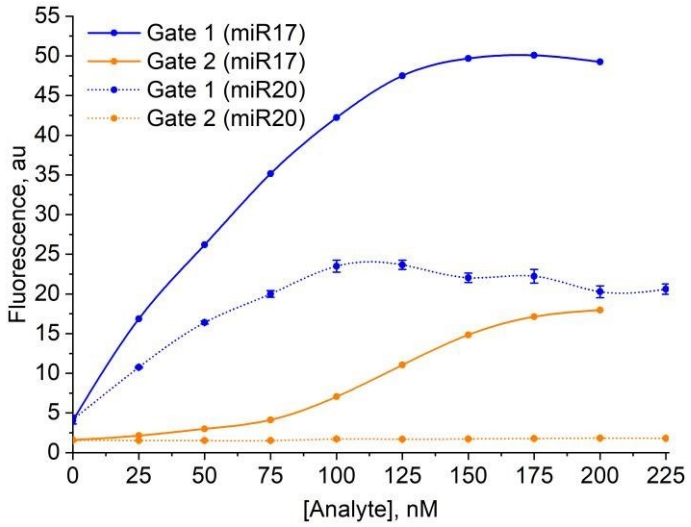

Figure 30. Response of FTh to miR20 and miR17. The concentration dependence of miR20 is shown in the dashed lines for Gate 1 (blue) and Gate 2 (orange), whereas the signal for miR17 is shown as a solid line.

Alternative Analyte

To test the applicability of our sensor to another target, we tested miR146b, a miRNA involved in papillary thyroid cancer. The ΔΔG between Gate 1 and 2 was determined to be 10.05 kcal/mol for the RNA targets and 6.53 kcal/mol for the DNA targets.[147] We found that neither demonstrated the thresholding function and, again, the DNA analytes performed worse than their RNA counterparts (Figure 31).

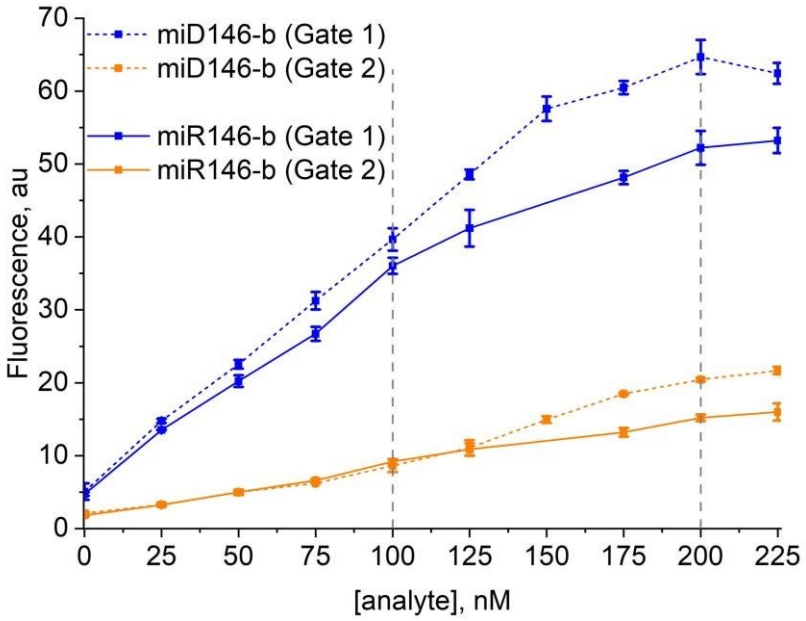

Figure 31. The Thresholding Response to miR146-b and miD146-b, a miRNA responsible for papillary thyroid cancer. The DNA analytes (dashed line) performed worse than the RNA analytes (solid line).

Biological Challenges

To mimic biological conditions, we challenged our sensor by adding 0.01-0.6 mM HSA to our buffer with 100 nM FTh. We added 200 nM of miR17 and found that there was almost no response from either gate above 0.5 mM HSA (SI 1). Therefore, we chose to further test 0.1 mM HSA-containing samples and added 20-nt randomized (NNN) oligonucleotides to compete with our sensor and analyte strands for binding to HSA. We found that the addition of (5 μM?) NNN increased the background for both gates, with the Gate 1 background increasing significantly compared to Gate 2. (SI 2). Increasing [NNN] from 1-10 uM caused an increase in the maximum fluorescence of Gate 1; conversely, minimal change in Gate 2 behavior was observed with increasing [NNN]. Compared to the performance of FTh in the absence of HSA and NNN, the hierarchical response of the gates also diminished.

Design Challenges

We first began designing the FTh sensor with a three-gate system (SI#). However, we could not produce a threshold response and found that two gates responded simultaneously. The removal of one of these gates showed an improvement in response.

After adopting the two-gate system, we moved towards extending the rail-binding arms for each of the attached strands. We found no difference in response, proceeded with the extended rail, and added the ROX fluorophore to allow for quantification of the sensor itself. The introduction of ROX resulted in a decrease in the maximum fluorescence seen for UMB L1. Additionally, the response for ROX was not constant and decreased as the signal from UMB L1 increased. To investigate the signal decrease for ROX and UMB L1, we tested the sensor by replacing the MBs with hairpins containing the same DNA sequence but no fluorophore or quencher. We tested the sensor response after replacing UMB L1 with HP1 (SI#) and UMB_FAM with HP3 (SI#). The ROX fluorophore doesn't affect the sensor's performance, but it does affect the maximum signal achieved by gate 1. The decrease in ROX signal is also affected by Cy5, which we show in experiments where UMB L1 is replaced by HP1 and UMB fam is replaced by HP3 (SI).

Discussion

Compared to the free strands (no rail) kinetics, we find that the rail-associated gates demonstrate faster kinetics for Gate 1 (FIG). This shows a cooperative effect that comes from having the two gates associated with each other on the rail. One hypothesis is that the Gate 2A strands can act as a scavenger strand, and recruit targets for hybridization to Gate 1A. Only once there are no available Gate 1A strands can the analytes begin to bind with Gate 2A.

Although we achieved a thresholding effect, the delayed response from Gate 2 was imperfect. Considering the results from the alternative analyte and RNA and DNA analytes, we

determined that a ΔΔG between the two gates should be at least 10-13 kcal/mol to achieve the thresholding effect.

Conclusion

By creating a multicomponent system with two gates differing in their free energies, we were able to design a thresholding system that can hierarchically respond to an input of analyte. The tile-associated FTh sensor outperforms its free-stranded counterpart by allowing for the scavenging of analyte and recruitment to the most thermodynamically stable when available. We could roughly determine the amount of analyte present through our derived equations by inputting only the fluorescent response of three fluorophores at their maximum, minimum, and test signals. This sensor shows promise as a point-of-care diagnostic tool that can quantify potentially oncogenic miRNAs that are over- or under-expressed. Another potential application of this thresholding sensor is that Gate 2 is replaced with an actuating component instead of a reporter. In the case of over-expressed miRNA, once the 'criteria' is met and a certain threshold is surpassed, the actuating element of Gate 2 could perform a therapeutic function similar to previously described nanodevices.[158]

CHAPTER SIX: CONCLUSIONS

This work achieved its goal of contributing to diagnostic medicine by using DNA nanotechnology to develop biosensors that overcome common challenges, including specificity, selectivity, and cost. In Chapter Two, we explored another challenge faced by molecular beacon probes and, through a systematic study, determined that undesired quenching can be avoided by ensuring that at least two nucleotides from the analyte overhang or are complementary to the 5'- end of the MBP. Alternatively, some applications of MBPs may find this dimerization desirable. For example, modified MBPs have been used in assays to intentionally create sticky-end pairing (dimerization)

that can be recognized and degraded by a nuclease, resulting in signal amplification and an improved detection limit.

Chapter Three explored a different adaptation to the molecular beacon probe that enabled it to hybridize with folded analytes using a single-stranded DNA tail with improved kinetics and thermodynamics. Although the Tailed molecular beacon probes were not selective, we moved forward and combined the unwinding feature of the Tailed MBPs and the selectivity of the OWL1 sensor to create the OWL2 sensor. In Chapter Four, we showed how the strain of the asymmetric P strand adds additional instability to the structure, making it able to dissociate from mismatched targets more readily. We found that the OWL2 sensor could detect folded targets via the unwinding arms, was selective at ambient temperatures, and was cost-effective due to its use of a universal molecular beacon probe. Looking to adapt our sensor to more real-world applications, we wanted to enable the OWL2 sensor to detect small quantities of mutant analyte, even when surrounded by large amounts of wild-type analyte. To do this, we needed our sensor to be incredibly selective. In Part II of Chapter Four, we explored the use of a blocker strand to improve the selectivity of the OWL2 sensor and, through collaboration, were able to identify the ΔΔG associated with the P-strand strain and rLOD of XX% **[Am I allowed to describe this in my work?].** Further applications of this sensor could include the detection of tumor-derived methylated DNA, which can constitute less than 0.1% of the total DNA in clinical samples, requiring highly sensitive and selective detection methods.[159–161]

Lastly, we explored a different type of sensor in Chapter Five that was not selective but could report quantities of miRNAs hierarchically. Although the threshold sensor has room for improvement, we were still able to achieve our goal of delaying the second response and determined the minimum ΔΔG necessary for attaining the threshold function. Aside from using the threshold sensor as purely diagnostic, it could be used as a therapeutic if imparted with an actuating component instead of the second signaling component.

The scientific discoveries uncovered in this work help elucidate the many possibilities of DNA Nanotechnology. By better understanding the natural rules of DNA and designing specialized components that can perform specific functions, we can create multifunctional DNA nanodevices that have implications in many fields.

APPENDIX MB DIMER: SUPPORTING INFORMATION FOR CHAPTER TWO

APPENDIX:O3418 TAILED MB CHAPTER SUPPLEMENTAL MATERIAL

Experimental Section

Reagents

All solutions were made using DNAse/protease-free water purchased from FisherScientific. Synthesized oligonucleotides were obtained from Integrated DNA Technologies, Inc (Coralville, IA) and concentrations of oligonucleotide stock solutions were quantified via absorbance at 260 nm on a ThermoScientific NanoDrop One (Waltham, MA).

Duplex Calibration Curve

Each molecular beacon probe was annealed with its complement by heating to 95 °C in 2 L of water for 5 minutes and cooled overnight. The MB probe and analyte were combined at 100 nM with a total volume of 1 mL. A calibration curve was then created by measuring the fluorescence for a range of duplex concentrations. The best-fit line was used to find the concentration of probe:analyte from the fluorescent intensity. Unless otherwise specified, all hybridization assays were performed with 50 mM Tris-HCl, 50 mM MgCl2, 0.1% Tween-20, and pH 7.4.

Kinetics Assays

Solutions containing hybridization buffer and molecular beacon probes were placed into a Cary Agilent Fluorimeter with λex = 485 nm and λem = 517 nm and excitation and emission slit widths each at 10 nm. After reading the baseline for 60 seconds (MB1 and MB1-Tail) or 30 seconds (τMB or τTailMB), 50 nM of the respective analyte was added and mixed, and measurements were resumed after 10 sec. The temperature was kept at 22 °C using a Single Cell Peltier attachment.

Determination of Gibb's Free Energy (ΔG) for MB:Analyte complexes

The Gibbs energy values (ΔG) were obtained at 22 °C, [Na^+] = 50 mM, and [Mg^{2+}]= 50 mM using Mfold.

Limit of Detection Assays

The limit of detection was determined for each study by conducting fluorescence experiments using a 60 µL quartz cuvette in a PerkinElmer (San Jose, CA) in Cary Agilent Fluorescence Spectrophotometer with a xenon lamp. (λ_{ex} = 485 nm, λ_{em} = 517 nm). After the addition of analyte at varying concentrations, the samples were incubated in a 22 °C water bath for 30 min before being analyzed. Fluorescent values at 517 nm were recorded for three independent trials for each sample. The averages and standard deviations were plotted in Excel and OriginLab 2021 (Northampton, MA), and the linear region was found and fitted with an equation. The LOD was determined by using the equation with the fluorescent signal of the blank + 3*(Standard deviation of the blank).

Differentiation Fluorescent Assays

The differentiation of each tested sensor was determined by conducting fluorescence experiments in a similar manner to the limit of detection. The signal to background was determined by taking the ratio of MB probe fluorescence in the presence of the analyte divided by the fluorescence of just the MB probe in a hybridization buffer following a 30-minute incubation (50 nM MB, 100 nM analytes). The differentiation factor was used to determine the differentiation of wild-type from mutant analyte. The differentiation factor (Df = 1- ΔFmm/ΔFm) was calculated with ΔF representing the difference in signal from the blank for the mismatched (mm) and matched (m) analyte, respectively, and subtracting this from 1. All calculations were done using the fluorescent average of at least three trials.

Oligonucleotide Sequences

Table 2. Oligonucleotides used in the Tailed MB Probe study. Mutations are highlighted in red.

Name	Sequence 5‘ → 3‘[a-,f]
MB1-Tail	CGT CCG CCA C /iFluorT/ CCGT CAG CGA AGC AGC ACGG /3BHQ_1/
MB1	/FAM/ CCG TCA GCG AAG CAG CAC GG /3BHQ_1/
16S-60 WT	GTC GAA CGG TAA CAG GAA GCA GCT TGC TGC TTC GCT GAC G A GTG GCG G ACG GGT GAG TAA
16S-60 C/T	GTC GAA CGG TAA CAG GAA GCA GCT TGC TGC TTT GCT GAC G A GTG GCG G ACG GGT GAG TAA
16S-60 G/T	GTC GAA CGG TAA CAG GAA GCA GCT TGC TTC TTCGCT GAC G A GTG GCG G ACG GGT GAG TAA
16S-60 (s-1)	GTC GAA CGG TAA CAG CAA GCA GCT TGC TGC TTG GCT GAC G A GTG GCG G ACG GGT GAG TAA
16S-60 mut (s-2)	GTC GAA CGG TAA CAG CTA GCA GCT TGC TGC TAG GCT GAC G A GTG GCG G ACG GGT GAG TAA
16S-60 mut (s-3)	GTC GAA CGG TAA CAG CTT GCA GCT TGC TGC AAG GCT GAC G A GTG GCG G ACG GGT GAG TAA
16S-60 (t-1)	GTC GAA CGG TAA CAG GAA GCA GCT TGC TGC TTC GCT GAC G A GTG ACG G ACG GGT GAG TAA
16S-60 (t-2)	GTC GAA CGG TAA CAG GAA GCA GCT TGC TGC TTC GCT GAC G A GTA ACG G ACG GGT GAG TAA
16S-60 (t-3)	GTC GAA CGG TAA CAG GAA GCA GCT TGC TGC TTC GCT GAC G A GAA ACG G ACG GGT GAG TAA
16S-16 WT	TGC TGC TTC GCT GAC G
16S-16 C/T	TGC TGC TTT GCT GAC G
16S-16 G/T	TGC TTC TTC GCT GAC G
тMB-Tail	GAC GTTT GA AGG T^{FAM} CCGC TAC TCA CAC TGC CGC GCGG /3BHQ_1/
тMB	FAM-CCGC TAC TCA CAC TGC CGC GCGG/3BHQ_1/
т-17 WT	GCG GCA GTG TGA GTA CC
т-17 0C	GCG GCA GCG TGA GTA CC
т-17 1A	GCG GCA ATG TGA GTA CC
т-60 WT	CA AAC ACG TCC CGG GAG GCG GCA GTG TGA GTA CCT TCA C AC GTC CCA TGC GCC GTG CTG T
т-60 0C	CA AAC ACG TCC CGG GAG GC G GCA GCG TGA GTA CCT TCA C AC GTC CCA TGC GCC GTG CTG T
т-60 1A	CA AAC ACG TCC CGG GAG GCG GCA A TG TGA GTA CCT TCA C AC GTC CCA TGC GCC GTG CTG T

Supplementary Images

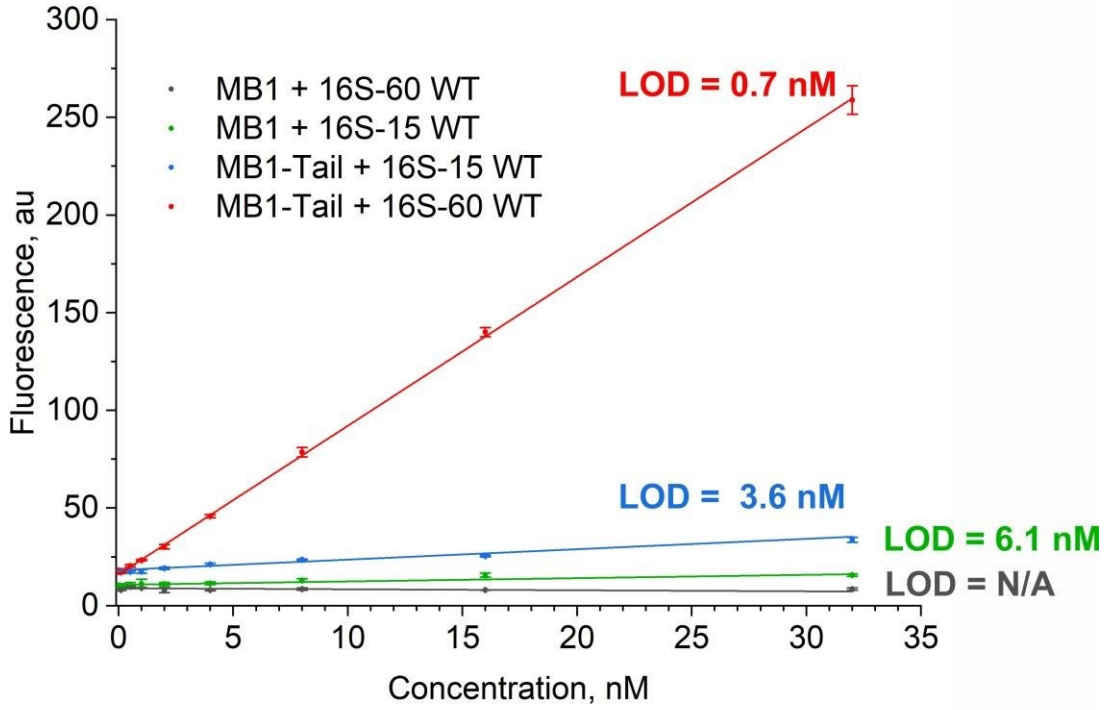

Equation	y = a + b*x			
Plot	MB1 + 16S-60 WT	MB1 + 16S-15 WT	MB1-Tail + 16S-15 WT	MB1-Tail + 16S-60 WT
Intercept	8.9 ± 0.3	10.7 ± 0.3	18.2 ± 0.6	16.0 ± 0.3
Slope	-0.05 ± 0.02	0.17 ± 0.02	0.53 ± 0.07	7.62 ± 0.11
Pearson's r	-0.71	0.95	0.95	1.00
R-Square (COD)	0.50	0.89	0.90	1.00
Adj. R-Square	0.43	0.88	0.89	1.00

Figure 32. Limit of Detection for MB1 and MB1-Tail with long and short 16S analytes. A calibration curve was used to determine the Limit of Detection (LOD) for each analyte by finding the line of best fit. To determine LOD, the average signal of the blank (F0) was added to three times the blank's standard deviation (SD), and this value was used in the line of best fit to solve for x, the lowest detectable concentration of the analyte.

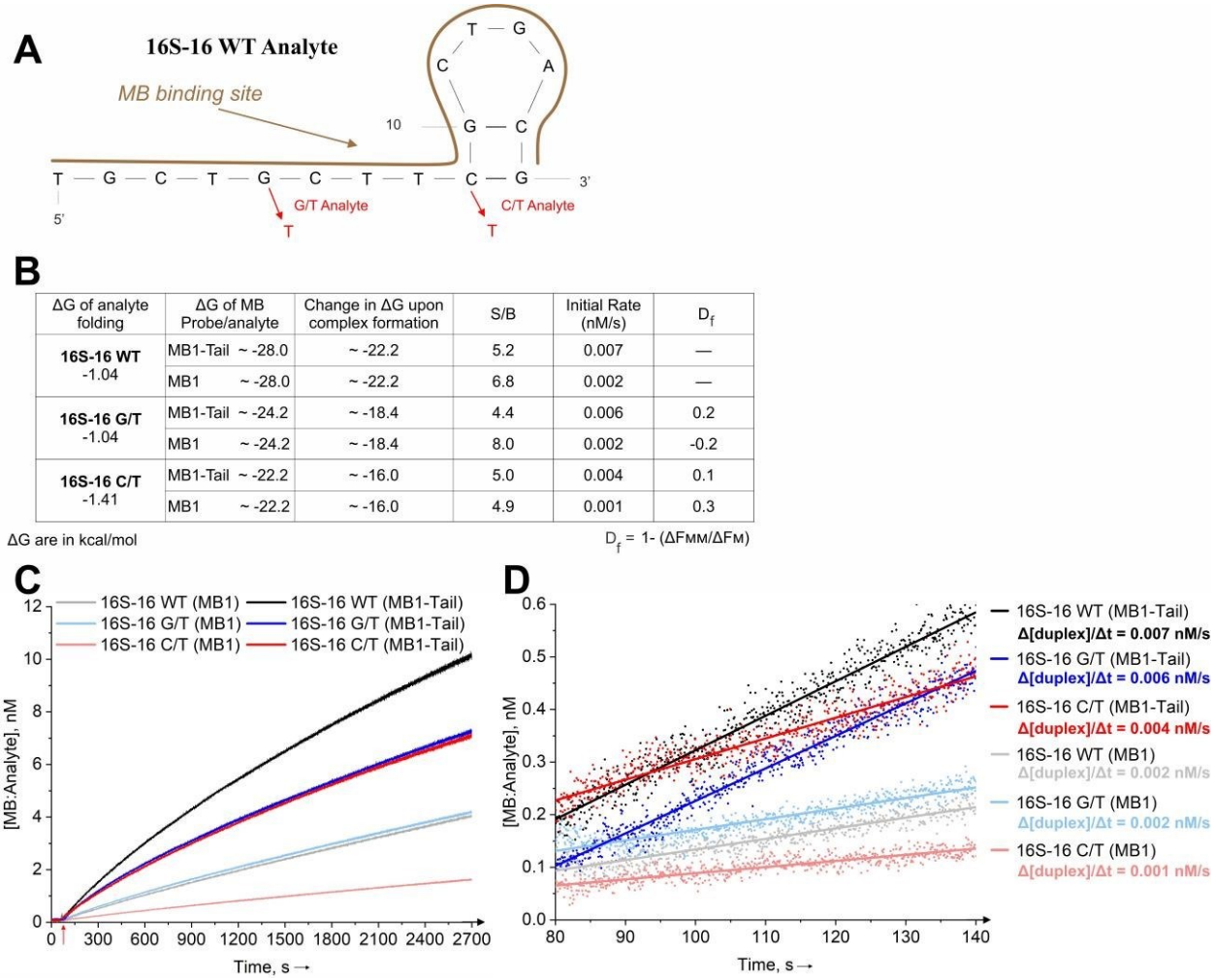

Figure 33. Kinetics and quantitative data for 16-nt linear fragments of 16S analytes. **(A)** The secondary structure of the 16S-16 WT analyte, with red arrows indicating the position of mutants G/T and C/T. The brown outline indicates the binding region of the MB probe and encompasses the entire analyte sequence. **(B)** Free energy values and quantitative data for the analytes. The signal to background was determined by taking the ratio of MB probe fluorescence in the presence of the analyte divided by the fluorescence of just the MB probe in a hybridization buffer following a 30-minute incubation (50 nM MB, 100 nM analytes). The differentiation factor was used to determine the differentiation of wild-type from the mutant analyte, and the equation used was Df = 1 − ΔFmm/ΔFm, where ΔF represents the signal of matched (m) or mismatched (mm) analyte with the signal of the blank (no analyte) subtracted. **(C)** The time-dependent hybridization kinetics between analytes and MB1 or MB1-Tail were measured. The analytes were added at the 60s time point, and measurements were resumed at ~75 s, as indicated by the red arrow. **(D)** Initial hybridization rates of 16S analyte with MB1 and MB1-Tail. The line of best fit was used to determine the slope over the first 60 seconds and was taken to be the initial rate of duplex formation.

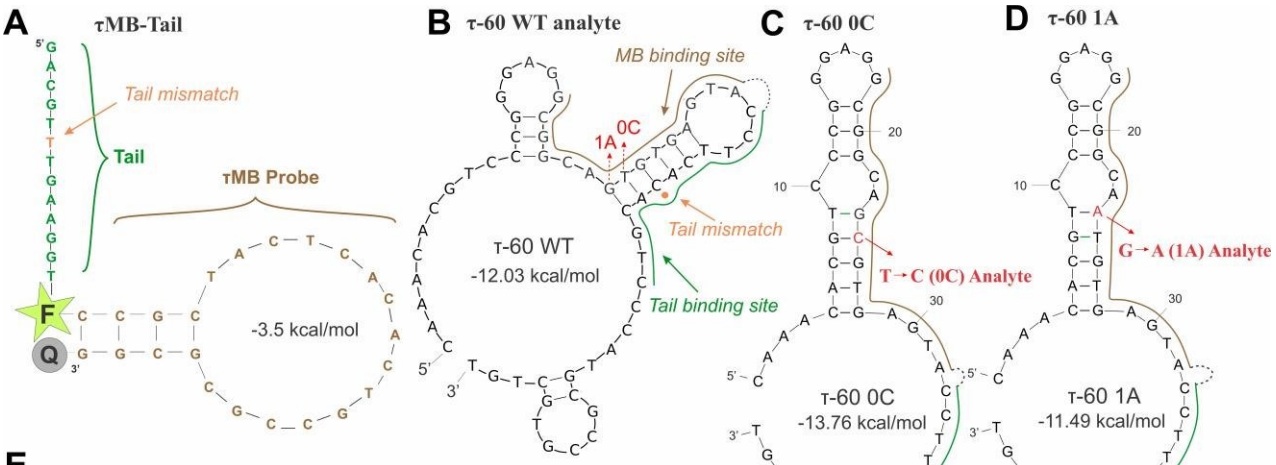

E

ΔG of analyte folding	ΔG of MB Probe/analyte		Change in ΔG upon complex formation	S/B	D_f
τ-60 WT -12.03	τMB-Tail	~ -38.4	~ -22.9	5.2	—
	τMB	~ -28.2	~ -12.7	1.7	—
τ-60 0C -13.76	τMB-Tail	~ -33.6	~ -16.3	11.8	-1.6
	τMB	~ -23.4	~ -6.1	1.6	0.1
τ-60 1A -11.49	τMB-Tail	~ -33.1	~ -18.1	11.3	-1.4
	τMB	~ -22.9	~ -7.9	1.6	0.1

ΔG are in kcal/mol

D_f = 1- (ΔFмм/ΔFм)

Figure 34. Secondary structures of τMB and Tau analytes with quantitative hybridization parameters. **(A)** τMB-Tail has the additional tail outlined in green, τMB outlined in brown, and a mismatch in the tail in blue. **(B)** Secondary structure of τ-60 WT with the tail and MB-binding sites outlined in green and brown, respectively. The SNV-containing analytes 0C and 1A tested are indicated with red arrows in panels **(C)** and **(D)**. The blue circle represents a mispairing of C:T with T in the tail of the τMB-Tailed probe to prevent unwanted self-complementarity. **(E)** The free energy associated with each analyte, the complex formed between analyte and probe, the free energy change associated with the formation of the complex, and the differentiation factor for mutant analytes. The signal to background (S/B) was calculated by taking the fluorescent signal at 30 minutes and dividing it by the MB signal. The differentiation factor is calculated with the equation Df = 1 − ΔFmm/ΔFm, where ΔF represents the signal of matched (m) or mismatched (mm) analyte with the signal of the blank (no analyte) subtracted. Due to their secondary structure, the 0C and 1A mutants produced a higher S/B than the WT analyte, resulting in a negative Df. Compared to the WT analyte, the tail-binding region is mostly contained in a loop, rather than a stem, which allows the tail to easily bind and further facilitate the hybridization of the MB. ΔG values were estimated as described in Fig. 1 legend. ΔG for both τMB and τMB-Tail probes ΔG is –3.49 kcal/mol (not shown in the table). The data are average values of at least 3 independent measurements.

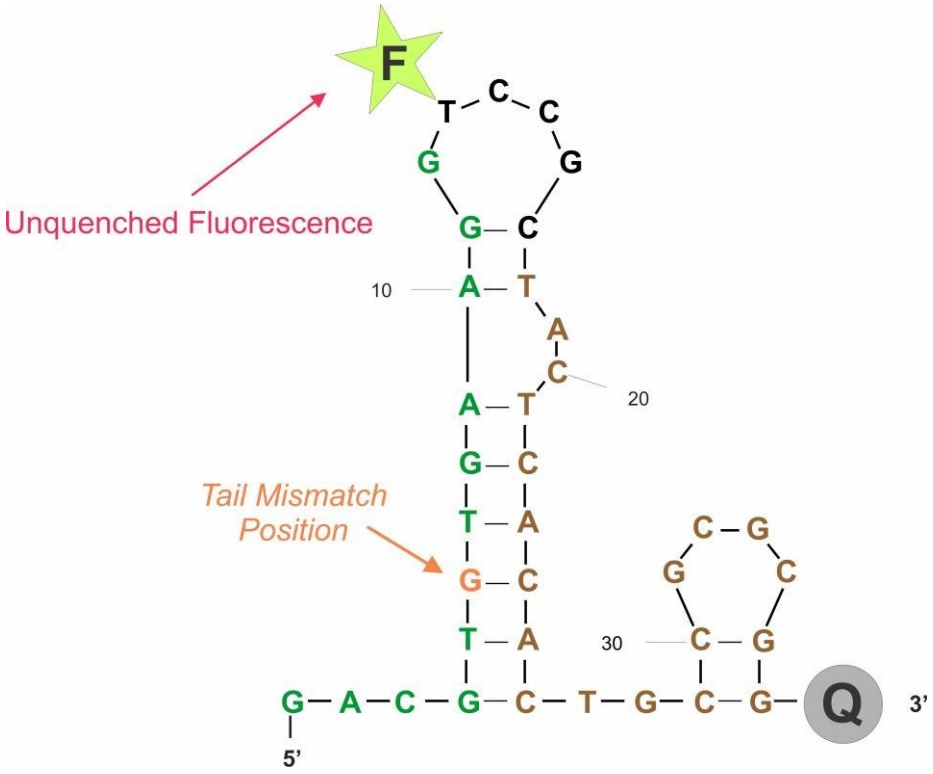

Figure 35. The Tail Invasion Problem in тMB-Tail Without a Tail Mismatch. Without introducing a mismatch in the tail, the MB probe adopts a more stable secondary structure in which the fluorophore cannot be quenched via contact quenching.

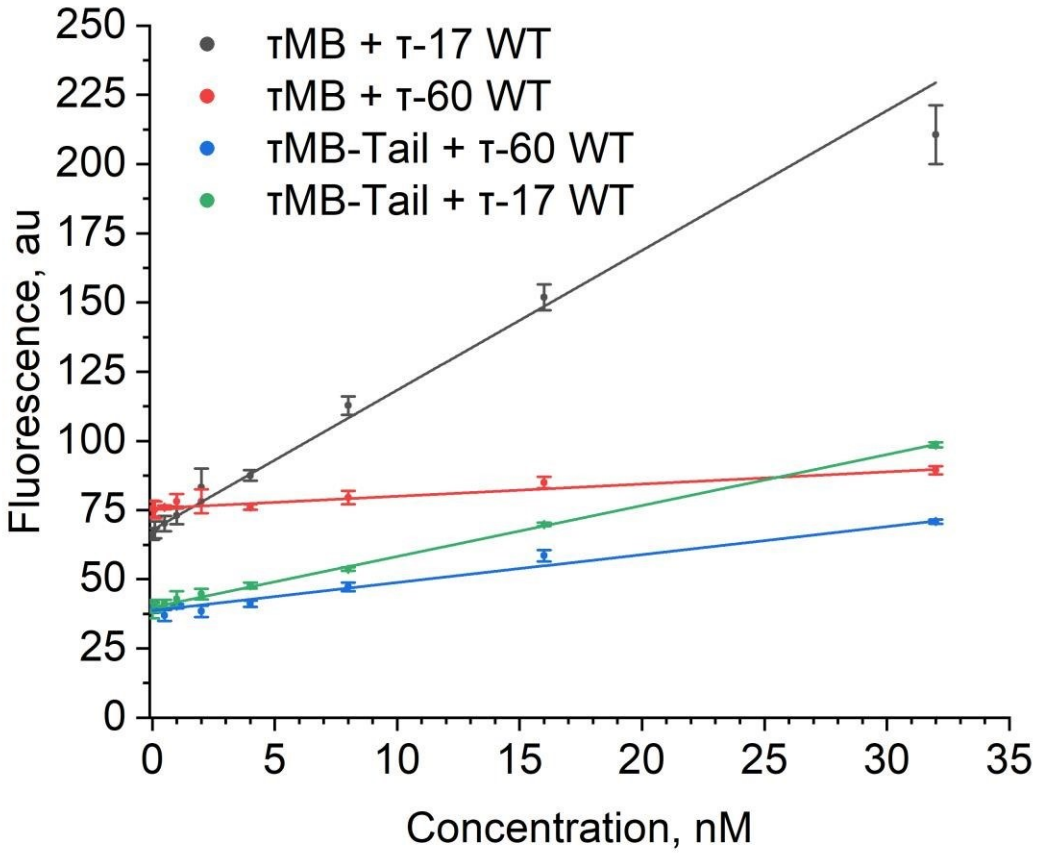

Equation	y = a + b*x			
Plot	τMB + τ-17 WT	τMB + τ-60 WT	τMB-Tail + τ-60 W	τMB-Tail + τ-17 W
Intercept	67.8 ± 1.2	75.6 ± 0.4	38.7 ± 0.5	39.9 ± 0.4
Slope	5.05 ± 0.21	0.44 ± 0.04	1.01 ± 0.03	1.84 ± 0.03
Pearson's r	0.99	0.98	1.00	1.00
R-Square (COD)	0.99	0.96	0.99	1.00
Adj. R-Square	0.99	0.95	0.99	1.00

Figure 36. Limit of Detection for τMB-Tail And τMB With Long and Short Tau Analytes. A calibration curve was used to determine the Limit of Detection (LOD) for each analyte by finding the line of best fit. To determine LOD, the average signal of the blank (F_0) was added to three times the blank's standard deviation (SD), and this value was used in the line of best fit to solve for x, the lowest detectable concentration of the analyte.

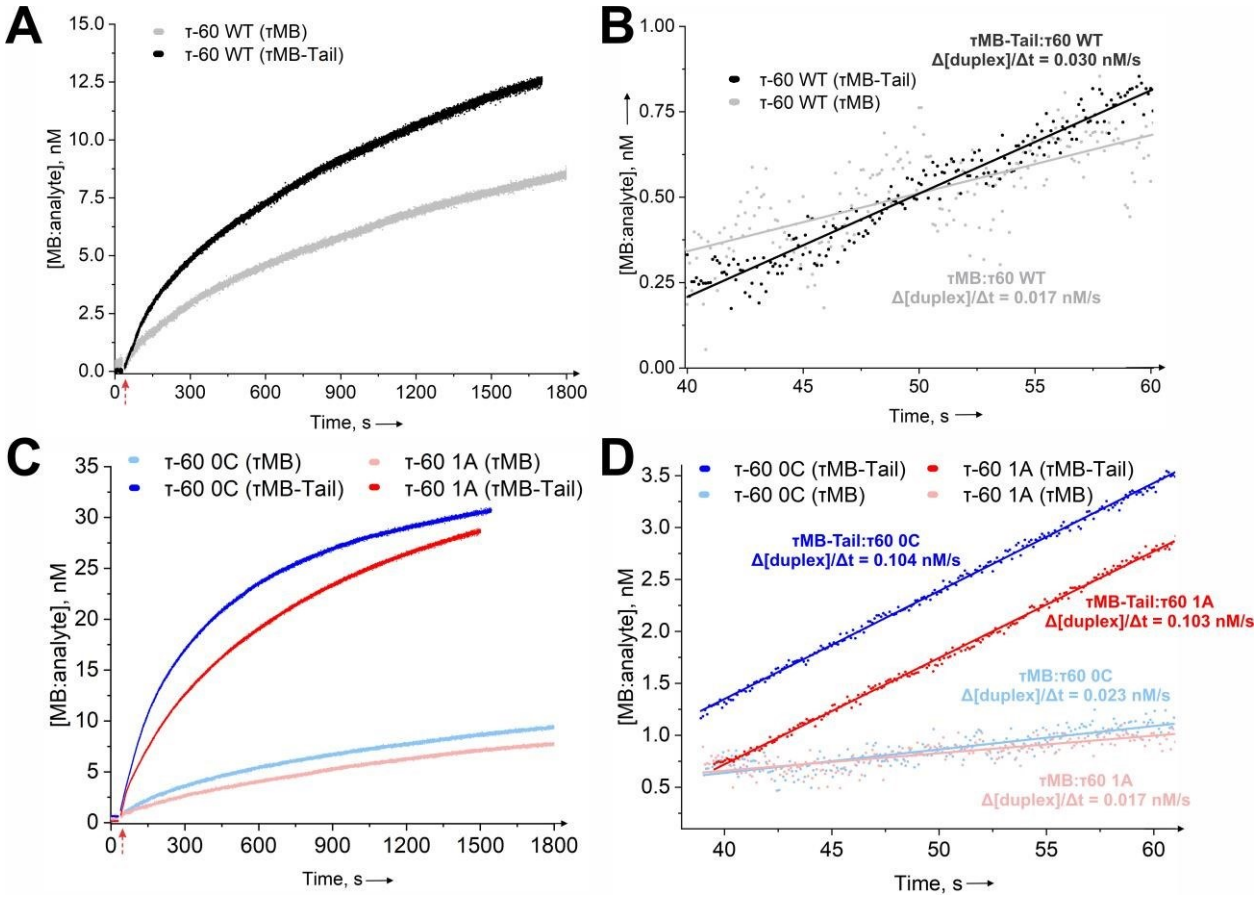

Figure 37. Tailed MB Probe Improves Hybridization Thermodynamics for 60-nt τ Analytes. **(A)** Time-dependent fluorescent duplex formation between MB probes and matched analytes. The analytes were added at the 30 s time point, indicated by the red arrow, and readings began again at ~40 s. The concentration of MB:Analyte was determined via calibration curves with MB:analyte duplexes (Fig. S12) **(B)** Initial hybridization rates of tau analytes with τMB and τMBTail. A line of best fit was determined over the first 20 seconds after analyte addition, and the slope was taken to be the initial rate of duplex formation. **(C)** Time-dependent fluorescent duplex formation for the mismatched τ-60 analytes, 0C and 1A. **(D)** Initial hybridization rates of τ-60 mismatched analytes with τMB and τMB-Tail resulted in a 4.5- and 6.1-fold increase for the 0C and 1A mutants, respectively. Compared to the WT analyte, the faster initial hybridization rates of 0C and 1A mutants can be explained by their secondary structure and the accessibility of ssDNA nucleotides that can readily hybridize with the tail in τMB-Tail and facilitate toeholdmediated hybridization (Fig. S2). The data are average values of at least three independent measurements.

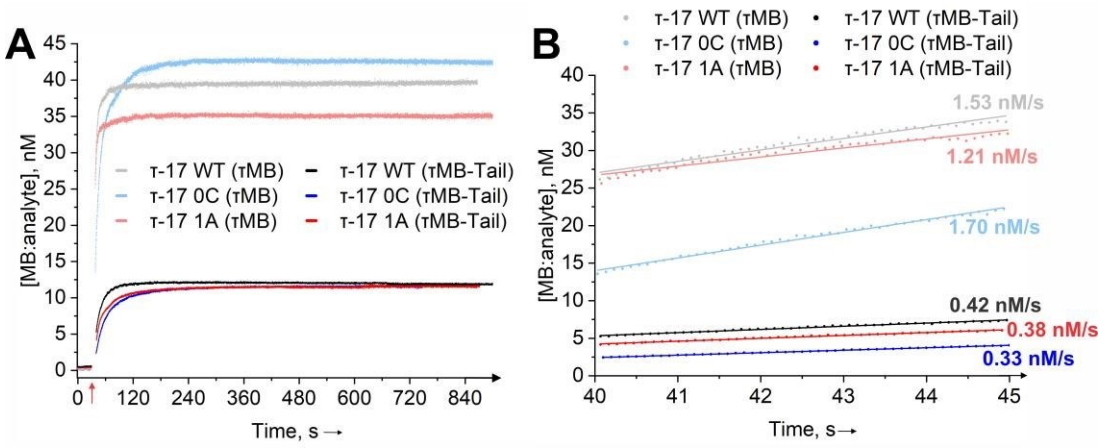

C

ΔG of analyte folding	ΔG of MB Probe/analyte	Change in ΔG upon complex formation	S/B	Initial Rate (nM/s)	D_f
τ-17 WT -0.22	τMB-Tail ~ -24.7	~ -21.0	4.1	0.42	—
	τMB ~ -24.7	~ -21.0	3.4	1.53	—
τ-17 0C -1.88	τMB-Tail ~ -19.9	~ -14.5	3.9	0.33	0.04
	τMB ~ -19.9	~ -14.5	3.5	1.70	-0.06
τ-17 1A -0.82	τMB-Tail ~ -19.4	~ -15.1	4.0	0.38	0.04
	τMB ~ -19.4	~ -15.1	3.0	1.21	0.14

ΔG are in kcal/mol

D_f = 1- (ΔFмм/ΔFм)

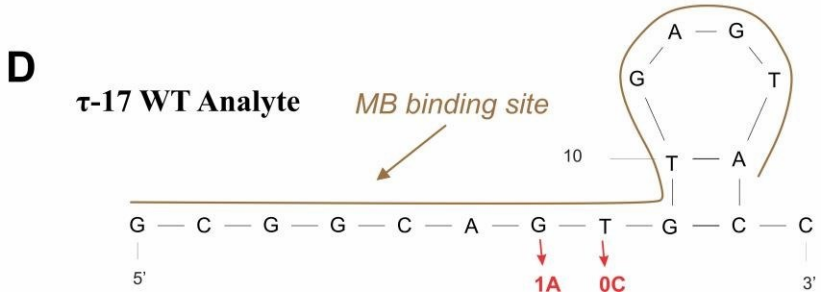

Figure 38. Kinetics and Quantitative data for 17-nt fragments of Tau Analytes. **(A)** Timedependent fluorescent duplex formation between MB probes and short tau analytes. The analytes were added at the 30 s time point, indicated by the red arrow, and readings began again at ~40 s. **(B)** Initial hybridization rates of analytes with τMB and τMB-Tail. A line of best fit was determined over the first 5 s after analyte addition, and the slope was taken to be the initial rate of duplex formation. **(C)** The free energy associated with each analyte, the complex formed between analyte and probe, the free energy change associated with the formation of the complex, and the differentiation factor for mutant analytes. The signal to background (S/B) was calculated by taking the fluorescent signal at 30 minutes and dividing it by the MB signal. The differentiation factor is calculated with the equation Df = 1 − ΔFmm/ΔFm, where ΔF represents the signal of matched (m) or mismatched (mm) analyte with the signal of the blank (no analyte) subtracted. ΔG values were estimated as described in Fig. 1 legend. ΔG for both τMB and τMBTail probes ΔG is –3.49 kcal/mol (not shown in the table). **(D)** Secondary structure of the τ-17 WT analyte, with the MB binding site outlined in brown and mutations indicated with red arrows.

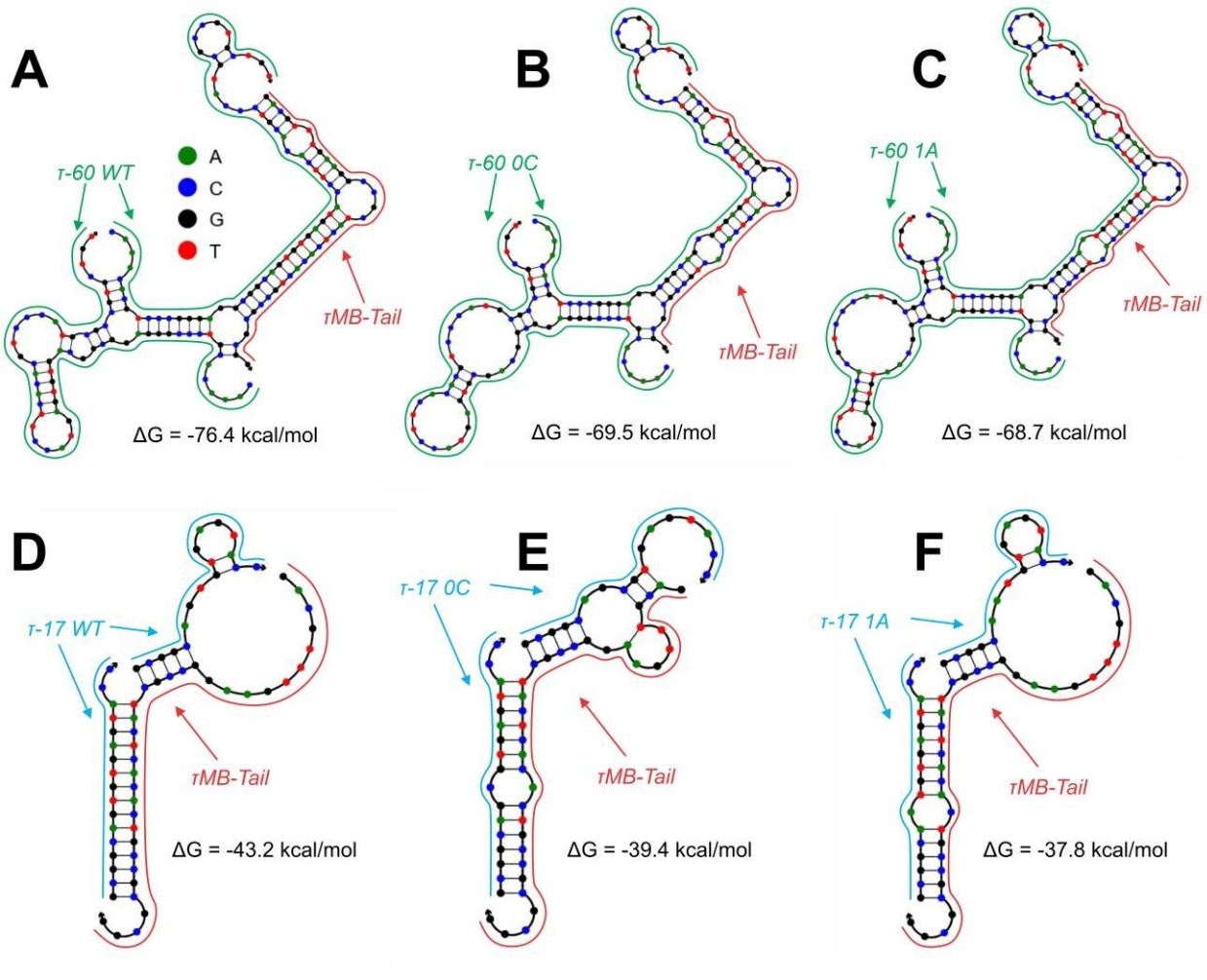

Figure 39. τMB-Tail probe can bind two analytes. **(A-C)** Secondary structures formed upon hybridizing two equivalents of 60 nt analyte with one equivalent of τMB-Tail. **(D-F)** Secondary structures formed upon hybridizing two equivalents of 17 nt analytes with one equivalent of τMB-Tail.

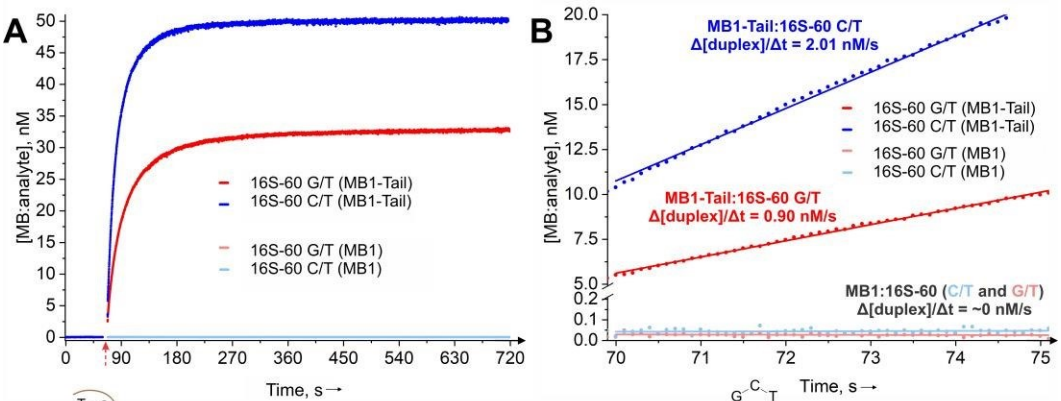

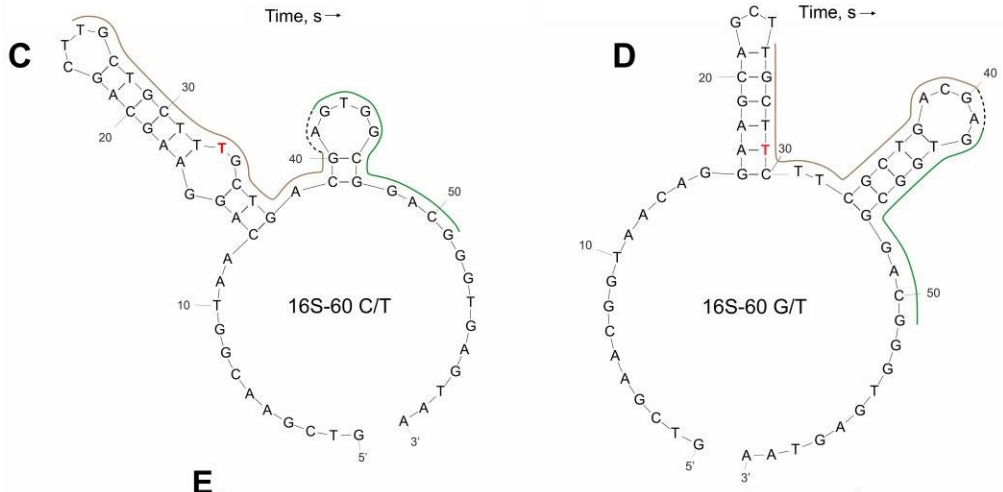

E

ΔG of analyte folding	ΔG of MB Probe/analyte	Change in ΔG upon complex formation	S/B	D_f
16S-60 C/T -12.50	MB1-Tail ~ -41.0	~ -23.7	48.8	-0.2
	MB1 ~ -25.2	~ -7.9	1.0	X
16S-60 G/T -10.6	MB1-Tail ~ -39.0	~ -23.6	40.7	0.1
	MB-1 ~ -23.1	~ -7.7	0.9	X

ΔG are in kcal/mol X- indistinguishable from background D_f = 1- (ΔFmm/ΔFm)

Figure 40. Tailed MB Probe Improves Hybridization Kinetics to Folded 16S Mutant Analytes. **(A)** The time-dependent hybridization kinetics between analytes and MB1 or MB1-Tail were measured. The analytes were added at the 60s time point, and measurements were resumed at ~70 s, as indicated by the red arrow. The MB:Analyte duplex concentration was determined using a line of best fit from a calibration curve (Fig. S13) **(B)** Initial hybridization rates of 16S analyte with MB1 and MB1-Tail. The line of best fit was used to determine the slope over the first 5 seconds and was taken to be the initial rate of duplex formation. **(C)** The secondary structure of the 16S-60 C/T and **(D)** 16S-60 G/T analyte, with mutated nucleotides in red. The brown outline indicates the binding region of the MB probe and the green outline indicates the binding region of the tail. **(E)** Free energy values and quantitative data for the analytes. The signal to background was determined by taking the ratio of MB probe fluorescence in the presence of the analyte divided by the fluorescence of just the MB probe in a hybridization buffer following a 30-minute incubation (50 nM MB, 100 nM analytes). The differentiation factor was used to determine the differentiation of wild-type from mutant analyte and the equation used was Df = 1 − ΔFmm/ΔFm, where ΔF represents the signal of matched (m) or mismatched (mm) analyte with the signal of the blank (no analyte) subtracted.

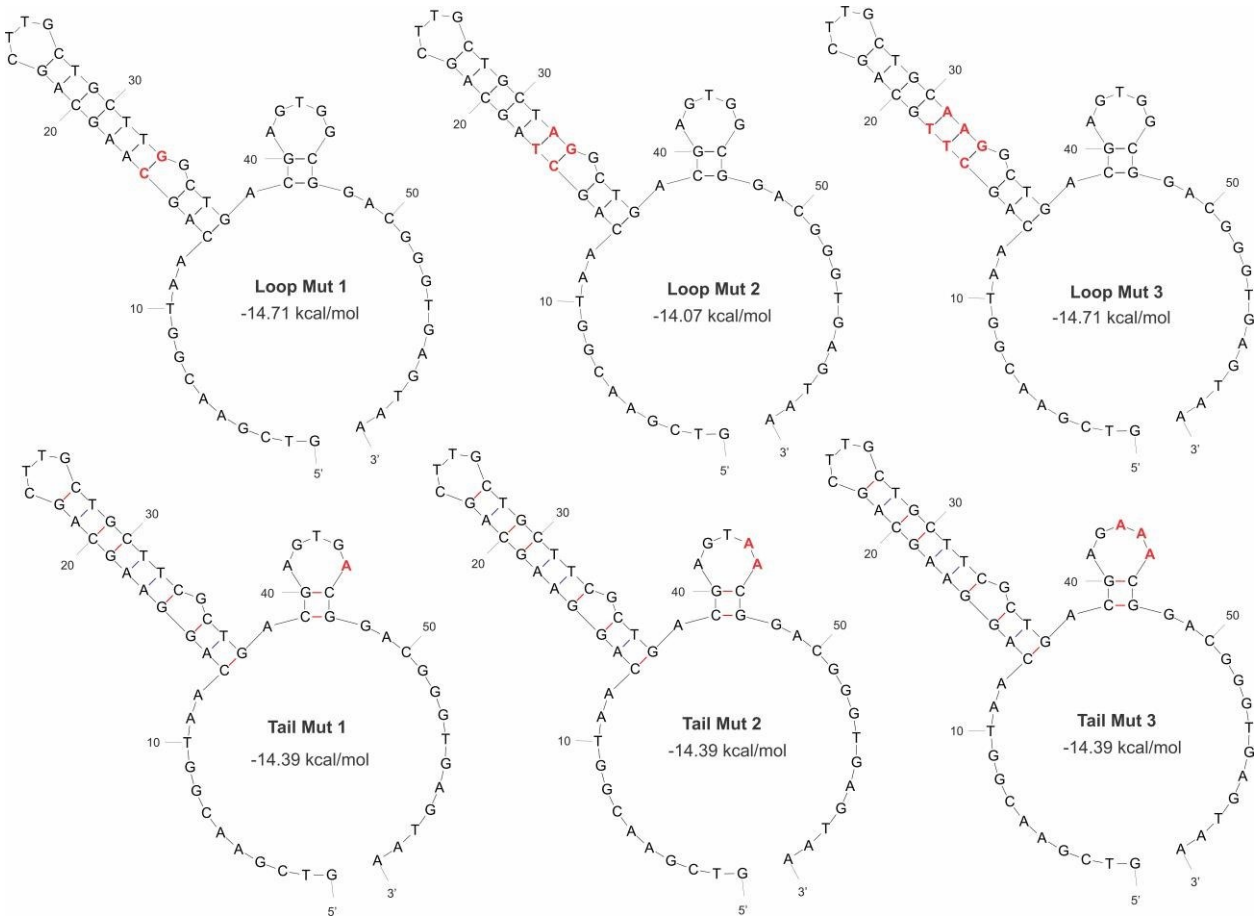

Figure 41. Secondary Structures Of 16S-60 Used In The Evaluation For Impact On MB1-Tail Regions. In the loop mutants **(Loop Mut 1-3),** the mutations emboldened in red were introduced such that the secondary structure was unaltered, but a mismatch to the MB stem loop was present. In the tail mutants **(Tail Mut 1-3)**, mismatches were introduced such that the secondary structure of the analyte was unaltered, but the complementarity to the tail of the MB1-Tail probe was reduced.

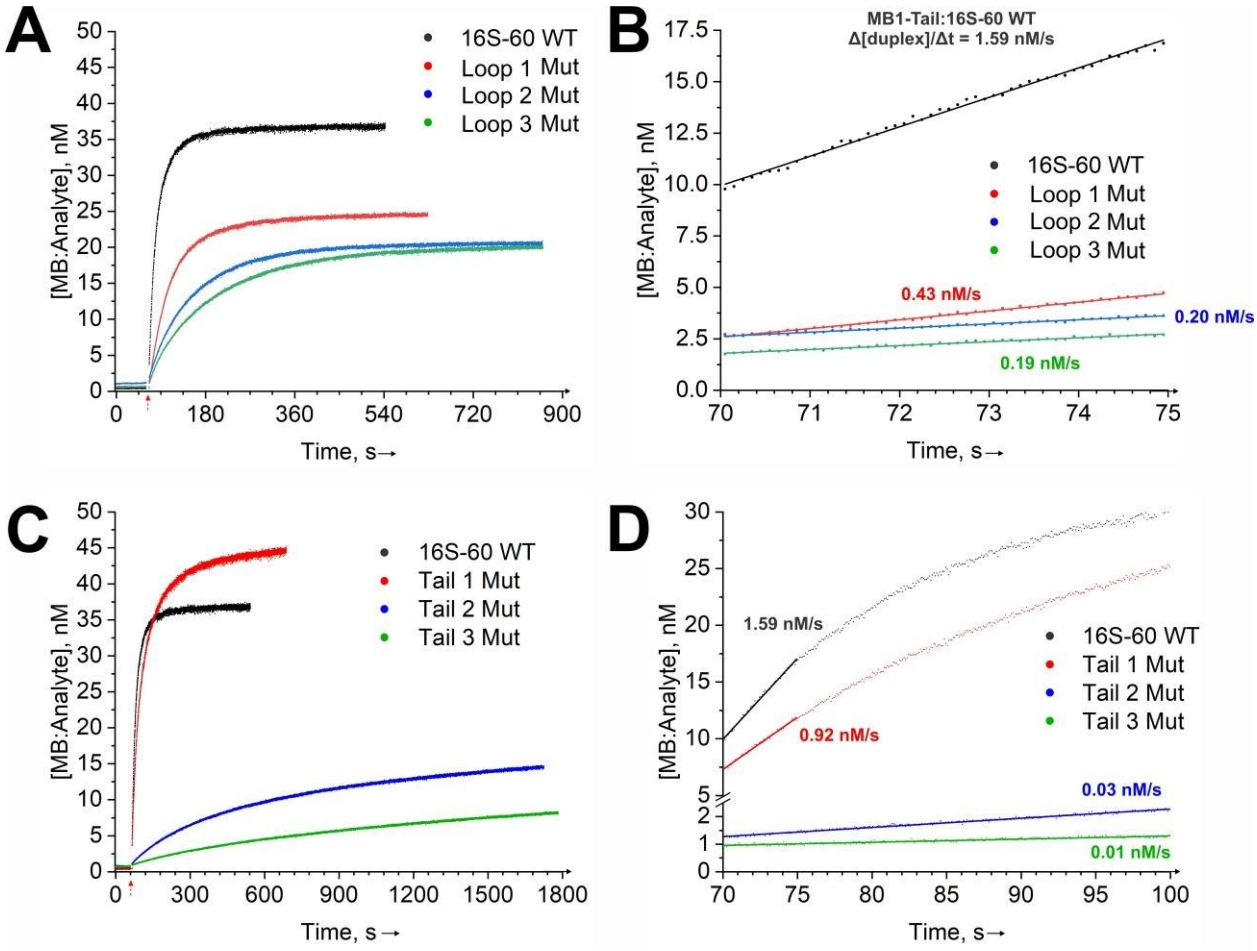

E

Mutant Type	Mutant	S/B	Initial Rate (nM/s)	D_f
Complementary to MB loop	Loop 1 Mut	32.8	0.43	0.24
	Loop 2 Mut	24.7	0.20	0.43
	Loop 3 Mut	21.2	0.19	0.51
Complementary to MB 'tail'	Tail 1 Mut	47.0	0.92	-0.10
	Tail 2 Mut	23.9	0.03	0.45
	Tail 3 Mut	13.0	0.01	0.71

$D_f = 1- (\Delta F_{MM}/\Delta F_M)$

Figure 42. Stem and Tail Mutant 16S Analyte Performance with MB1-Tail. **(A)** Time-dependent fluorescent duplex formation between 50 nM of MB probes and 100 nM of 16S analytes, either wild-type (WT) or with a mutation in the stem (Fig. S10). The analytes were added at the 60 s time point, indicated by the red arrow, and readings began again at ~70 s. **(B)** Initial hybridization rates of analytes with MB1 and MB1-Tail. A line of best fit was determined over the first 5 seconds after analyte addition, and the slope was taken to be the initial rate of duplex formation. **(C)** Similar to Panel A, but with analytes containing a mutation in the tail-binding region. **(D)** The initial rate of duplex formation was determined similarly to Panel B, but the rate for both the Tail 2 Mutant and Tail 3 Mutant were determined over 30 s due to an unobservable increase in the first

5 s. **(E)** Free energy values and quantitative data for the analytes. The signal to background was determined by taking the ratio of MB probe fluorescence in the presence of the analyte divided by the fluorescence of just the MB probe in a hybridization buffer following a 30-minute incubation (50 nM MB, 100 nM analytes). The differentiation factor was used to determine the differentiation of wild-type from mutant analyte and the equation used was Df = 1 − ΔFmm/ΔFm, where ΔF represents the signal of matched (m) or mismatched (mm) analyte with the signal of the blank (no analyte) subtracted.

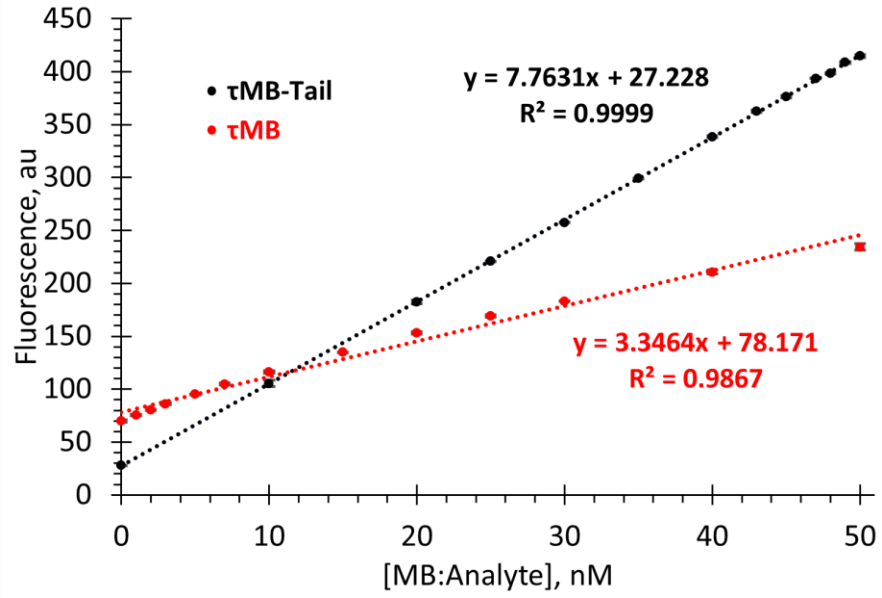

Figure 43. Calibration Curve for Calculation of Kinetic Constants of Hybridization. MB-probe and WT analyte were annealed at a concentration of 100 nM each, heating for 5 min at 95 °C and cooling overnight. The concentration of fluorescent duplex was assumed to be 100 nM. Serial dilution was performed to obtain solutions with a concentration of fluorescent duplex 0 – 50 nM. The Fluorescence of each solution was recorded in triplicate, and the line of best-fit and equation of best-fit lines were obtained in Excel. The data are average values of 3 independent measurements.

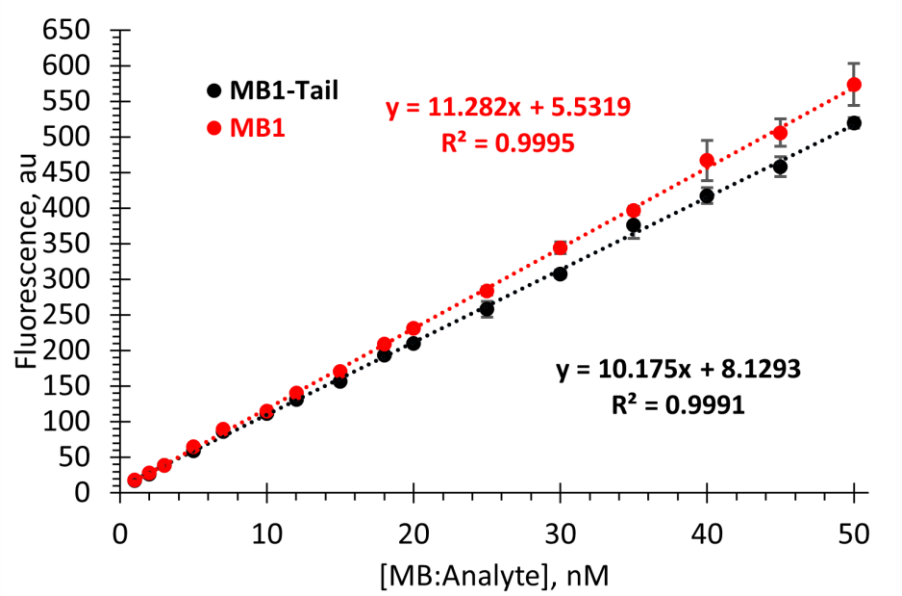

Figure 44. MB1 and MB1-Tail Calibration Curve for Calculation of Kinetic Constants of Hybridization. MB-probe and WT-16 analytes were annealed at a concentration of 100 nM each by heating for 5 min at 95C and cooling overnight. The concentration of fluorescent duplex was assumed to be 100 nM. Serial dilution was performed to obtain solutions with a concentration of fluorescent duplex 0 – 50 nM. The Fluorescence of each solution was recorded in triplicate, and the line of best-fit and equation of best-fit lines were obtained in Excel. The data are average values of 3 independent measurements.

APPENDIX:O2A OWL CHAPTER SUPPLEMENTAL MATERIALS

Experimental Section

Reagents

All solutions were made using DNAse/protease-free water purchased from FisherScientific. Synthesized oligonucleotides were obtained from Integrated DNA Technologies, Inc. (Coralville, IA), and concentrations of oligonucleotide stock solutions were quantified via absorbance at 260 nm on a ThermoScientific NanoDrop One (Waltham, MA).

Annealing of DNA Tiles

All tiles were annealed in 1 mL microcentrifuge tubes overnight (~8-10 h) in a 2 L bath of water after being heated to 95 oC and boiled for 5 min. Oligonucleotides were combined in a total volume of 1 mL with a concentration of 100 nM. Unless otherwise specified, tiles were annealed with T1, T2, T3, and T4 variations, but not the P-strand. The hybridization buffer consisted of 50 mM Tris-HCl, 50 mM MgCl2, 0.1% Tween-20, and pH 7.4.

Melt Curve Fluorescence Assays

Using DNA tiles previously annealed, UMB and ROX were added to the solutions to a final concentration of 25 nM and P-strand was added to a final concentration of 200 nM. Bringing the total volume to 30 µL each using either water or analyte, the samples were then added to the 96-well plate. A control consisting of only UMB and ROX were used, in addition to a sample containing the tile with no P-strand added, and a sample with no analyte added.

After adding the samples to the plate, an optical adhesive cover was securely fitted to the top of the plate and wells were sealed using a tool provided with the QuantStudioTM 6 Flex System. The plate was lightly flicked to eliminate bubbles and was vortexed and centrifuged for 20 s on a Fisher Scientific Mini Plate Spinner Centrifuge (Hampton, NH). After allowing 30 min for annealing the plate was then placed into the QuantStudioTM Flex 6 system and cooled to 5 oC where it was held for 5 min. The fluorescence of the samples was then read continuously as the samples were heated from 5 oC to 70 oC (0.1 oC/s). ROX was selected as a passive reference and FAM™ was read as the ‘Target’. Although the system was calibrated to account for well factors, background, and dye fluorescence, there were small variations between the background fluorescence of UMB and controls without analyte; therefore, there may be small fluorescence value variations observed depending on the date of the experiment.

Data was exported to excel and subsequently to OriginLab 2021 (Northampton, MA) for data normalization and processing. The processed readings from at least three wells were averaged and plotted as a function of FFAM/FROX. The derivative of fluorescence vs time was calculated by the QuantStudioTM Real-Time PCR Software to determine the melting temperature (T_m).

Limit of Detection Assays

The limit of detection was determined for each study by conducting fluorescence experiments using a 60 µL quartz cuvette in a PerkinElmer (San Jose, CA) LS-55 Fluorescence Spectrophotometer with a xenon lamp. (λex = 485 nm, λem = 517 nm). The samples were used directly from annealed tiles, and, to this solution, P-strand was added such that the final concentration was 200 nM and UMB was added to a final concentration of 25 nM. After the addition of analyte at varying concentrations, the samples were incubated in a 24 °C water bath for 30 min before being taken out of the bath and analyzed. Fluorescent values at 517 nm were recorded for three independent trials for each sample. The averages and standard deviations were plotted in Excel and OriginLab 2021 (Northampton, MA), and the linear region was found and fitted with an equation. The LOD was determined by using the equation with the fluorescent signal of the blank + 3*(Standard deviation of the blank).

Differentiation Fluorescent Assays

The differentiation of each tested sensor was determined by conducting fluorescence experiments in a similar manner to the limit of detection. For the OWL1 design, the samples were made such that Rx and Py were added to final concentrations of 150 nM and 200 nM, respectively, unless stated otherwise. The differentiation factor (Df = 1- ΔFmm/ΔFm) was calculated with ΔF representing the difference in signal from the blank for the mismatched (mm) and matched (m) analyte, respectively, and subtracting this from 1. For the Fm/Fmm assays, this was calculated by taking the Fluorescence of the Wild-Type analyte (Fm) and dividing it by the

Fluorescence of the respective SNV-containing analyte corrected by the blank. All calculations were done using the fluorescent average of at least three trials.

Kinetics Assays

Using the same experimental conditions as for the other fluorescent assays, the fluorescence was measured over 45 min on a Cary Agilent Fluorimeter for 45 min. The OWL2 sensor and Pstrand were mixed, the analyte was added, and fluorescence was read immediately afterward.

Oligonucleotide Sequences

Table 3 Oligonucleotides used in the assembly of variations of OWL2 Sensor. F, fluorescein; BQ1, black hole quencher 1; underlined are the fragments complementary to UMB probe; ttt, trithymidine linkers between tile-forming fragments and the analyte binding arms; /iSp18/ internal spacer 18.

Name	***Sequence 5'-> 3'***
UMB	F-CG C GTTC CCATA CAAC CAATC GCG-BQ1
T1	GAACG T GAA GGT ACT TATGG GTA TCA GTC ATT ACC AGT AGT CGGAC CTAGG CTCTCGGT CTA G CCAC TTAAC
$T2_2$	ACT ACT GGT AAT GAC TGA TAC *ttt* C GGC GCA TGG GAC GTG
$T3_2$-9 no linker	CCTAG GTCCG GAACG TGA AGG TACT TATGG
$T3_2$-9-ttt	CCTAG GTCCG *ttt*
$T3_2$-9 iSp18	CCTAG GTCCG/*iSp18*/ GAACG TGA AGG TACT TATGG
$T3_2$-9 RiSp18	CCTAG GTCCG *ttt*
$T4_2$	GC CTC CCG GGA CGT GT ttt GTT AA GTGG CTAG ACCGAGAG
T32-9 + T42+1	CGC CTC CCG GGA CGT GT ttt GTT AA GTGG CTAG ACCGAGAG CCTAG GTCCG ttt GAACG T GAA GGT ACT TATGG
$T4_2$+1	CGC CTC CCG GGA CGT GT ttt GTT AA GTGG CTAG ACCGAGAG GAACG T */iSp18/* GAA GGT ACT TATGG
$T4_2$-1	C CTC CCG GGA CGT GT ttt GTT AA GTGG CTAG ACCGAGAG
CT2	ACT ACT GGT AAT GAC TGA TAC ttt GTTC AAGA AATT CAAC
CT3-9	CCTAG GTCCG ttt GAACG TCCAG GCAGC TATGG
CT4	ACTT CTCC TGCT AGAA ttt GTT AA GTGG CTAG ACCGAGAG
CT4+1	AACTT CTCC TGCT AGAA ttt GTT AA GTGG CTAG ACCGAGAG

Table 4 Sequences of P-strand and R-strand variations used in this study. Underlined nucleotides are complementary to the UMB probe.

Name	***Sequence 5' -> 3'***
P_{99}	GTTG CAC ACT GCC GATTG
P_{89}	GTTG CAC ACT GCC ATTG
P_{98}	GTTG CAC ACT GC GATTG
P_{98} A>G	GTTG CAC GCT GC GATTG
P^{9}_{8} C>T	GTTG CAC ATT GC GATTG
P_{108}	GGTTG CAC ACT GC CGATT
P_{109}	GGTTG CAC ACT GCC CGATT
P_{88}	GTTG CAC ACT GC ATTG
P_{97}	GTTG CAC ACT G GATTG
C_{98}	GATTG GTTG CAC ACT GC
CP_{99}	GTTG AGTA AACGA GATTG
CP_{98}	GTTG AGTA AACG GATTG
R_{1010}	GAACG GTGAAGGTAC TATGG

Table 5 Sequences of the analytes used in the OWL2 study. SNV sites are in red; underlined are the fragments complementary to P and R strands; RNA nucleotides are shown in lowercase.

Name	***Sequence 5'-> 3'***
Tau60-WT	CA AAC ACG TCC CGG GAG GC G GCA GTG TGA GTA CCT TCA C AC GTC CCA TGC GCC GTG CTG T
Tau60-WT (RNA)	ca aac acg ucc cgg gag gc g gca gug uga gua ccu uca c ac guc cca ugc gcc gug cug u
Tau60-0C	CA AAC ACG TCC CGG GAG GC G GCA GCG TGA GTA CCT TCA C AC GTC CCA TGC GCC GTG CTG T
Tau60-1A	CA AAC ACG TCC CGG GAG GCG GCA ATG TGA GTA CCT TCA C AC GTC CCA TGC GCC GTG CTG T

Tau60-2G	CA AAC ACG TCC CGG GAG GCG GCG GTG TGA GTA CCT TCA C AC GTC CCA TGC GCC GTG CTG T
Tau19-WT	GCA GTG TGA GTA CCT TCA C
Tau19-0C	GCA GCG TGA GTA CCT TCA C
Tau19-1A	GCA ATG TGA GTA CCT TCA C
Tau18_WT	GCA GTG TGA GTA CCT TCA
Tau18_0C	GCA GCG TGA GTA CCT TCA
Tau18_1A	GCA ATG TGA GTA CCT TCA
CVD60_WT	TGC CAG CCA TTC TAG CAG GAG AAGT TCG TTT ACT GCT GCC TGG A G TTG AAT TTC TTG AAC
CVD60_1C	TGC CAG CCA TTC TAG CAG GAG AAGT TCG CTT ACT GCT GCC TGG A G TTG AAT TTC TTG AAC
CVD60_0G	TGC CAG CCA TTC TAG CAG GAG AAGT TCG TGT ACT GCT GCC TGG A G TTG AAT TTC TTG AAC

Supplementary Images

A

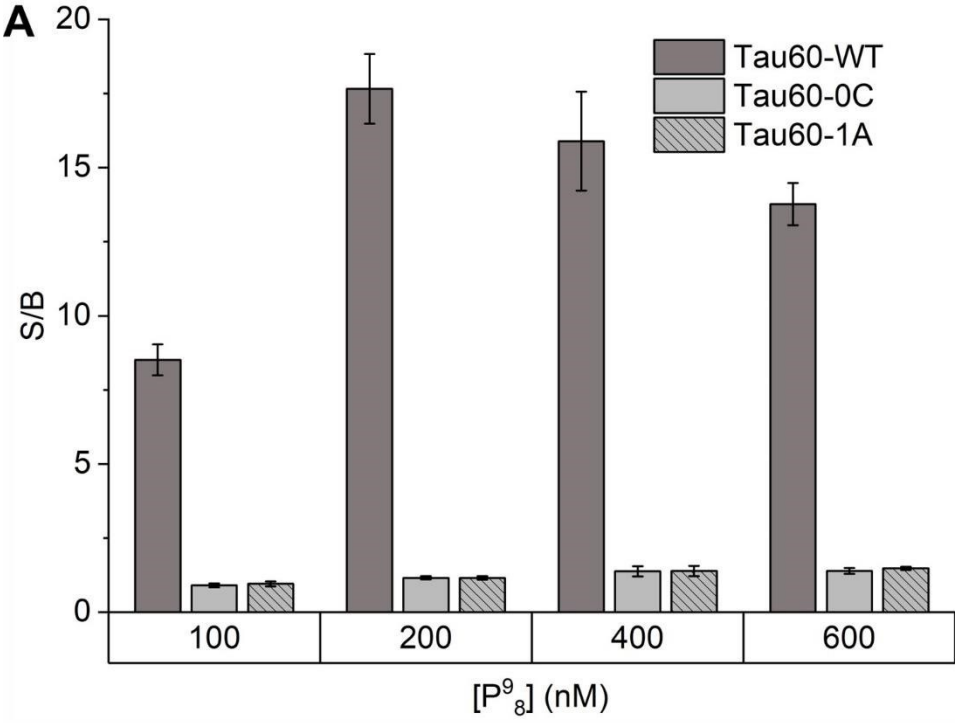

B

	S/B			D_f	
[P98] (nM)	**WT**	**0C**	**1A**	**0C**	**1A**
100	8.5	0.9	1.0	1.01	1.00
200	17.7	1.2	1.2	0.99	0.99
400	15.9	1.4	1.4	0.97	0.97
600	13.8	1.4	1.5	0.93	0.82

Figure 45 Optimization of P-strand concentration for OWL2 sensor A) Concentration dependence of P98 with 100 nM of our OWL2 sensor. B) Table depicting the exact values for S/B from the graph as well as differentiation factor (Df = 1- ΔFmm/ΔFm where ΔF represents the difference in signal from the blank for the mismatched (mm) and matched (m) analyte, respectively).

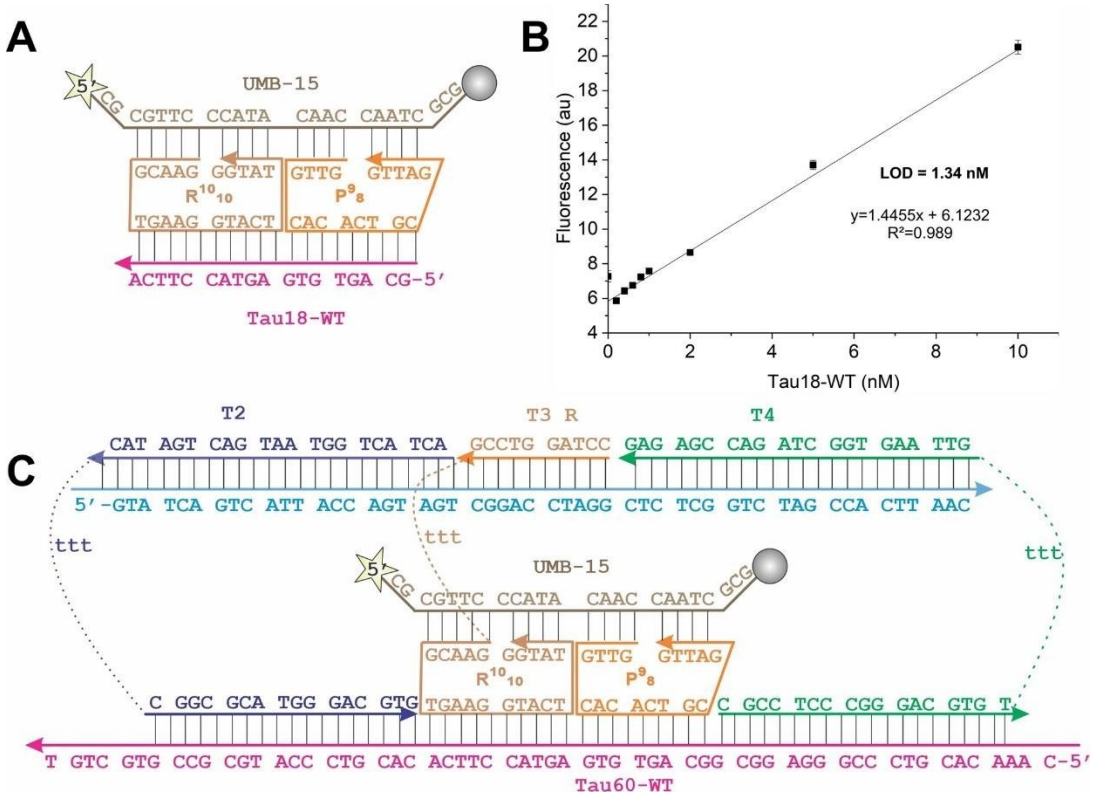

Figure 46 OWL1 and OWL2 sensors in complex with Tau analyte. A) OWL1 design consists of R- and P-strand along with UMB-15 to form a complex with short-fragment Tau18-WT analyte. B) Limit of detection of Tau18-WT with the OWL1 sensor. C) OWL2 design has additional T2- and T4- unwinding arms which allow for the opening of longer Tau60-WT analyte with secondary structure.

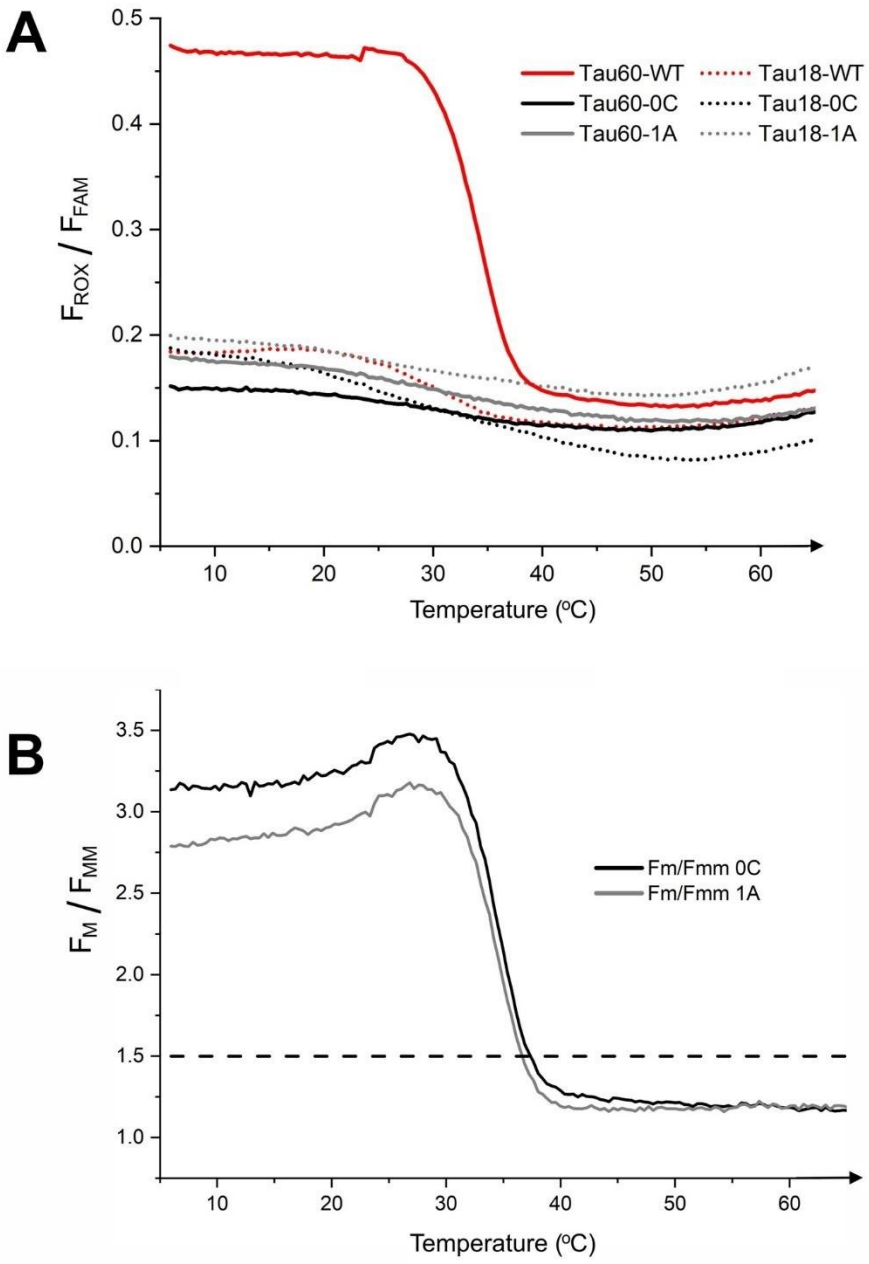

Figure 47 Melting curve for OWL2 sensor shows discrimination for fully matched WT from SNVcontaining analytes from 5-38 oC. The melting curve (left) normalized using ROX as an internal reporter shows the higher signal from the WT folded analyte. The discrimination (right) is shown by dividing the fluorescence of the fully matched wild-type analyte by the fluorescence of the mismatched analyte. The dashed 1.5 line is the threshold at which we determine that the wildtype has been differentiated from the mutant.

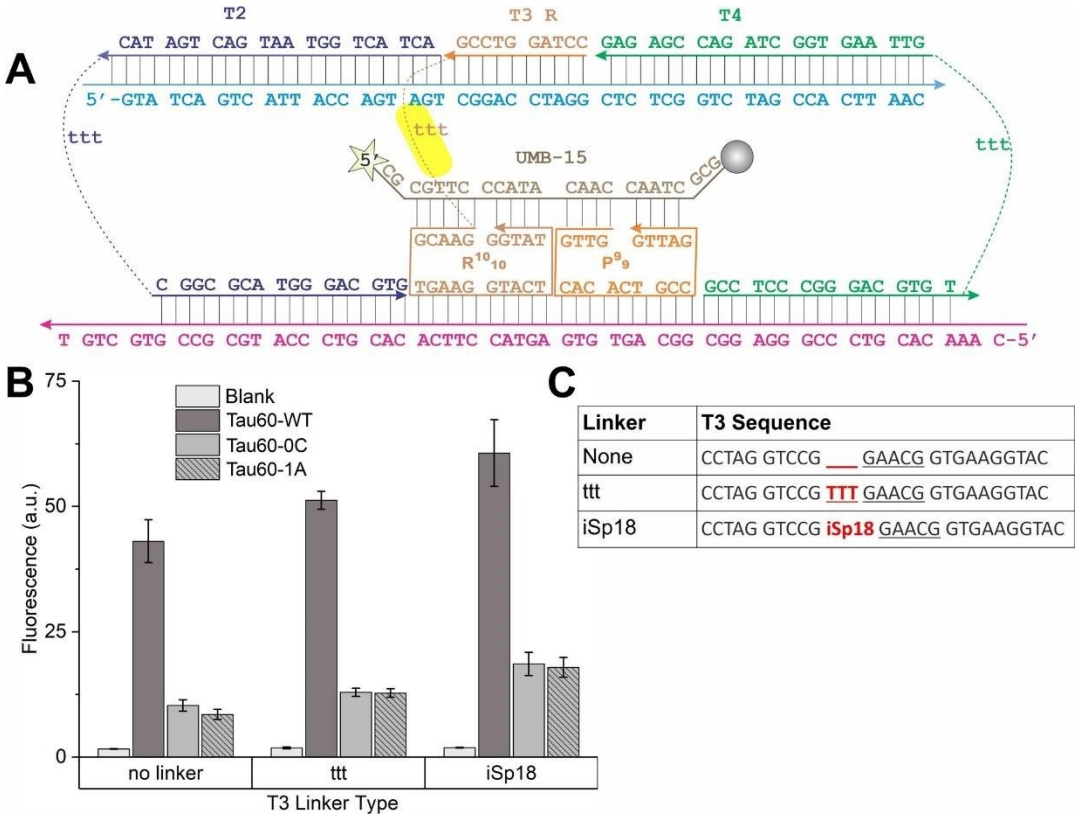

Linker	T3 Sequence
None	CCTAG GTCCG ___ GAACG GTGAAGGTAC
ttt	CCTAG GTCCG TTT GAACG GTGAAGGTAC
iSp18	CCTAG GTCCG iSp18 GAACG GTGAAGGTAC

Figure 48 Flexible linkers between R stand and tile provides higher fluorescence. (A) OWL2 design with P99 with the highlighted region representing the linker between T1-hybridizing portion of T3 and the UMB- and analyte- hybridizing R portion of T3 (B) Fluorescence measured on PerkinElmer Fluorimeter showing an increase in fluorescence for all analytes. (C) Table containing the sequence of T3 and the types of linkers tested.

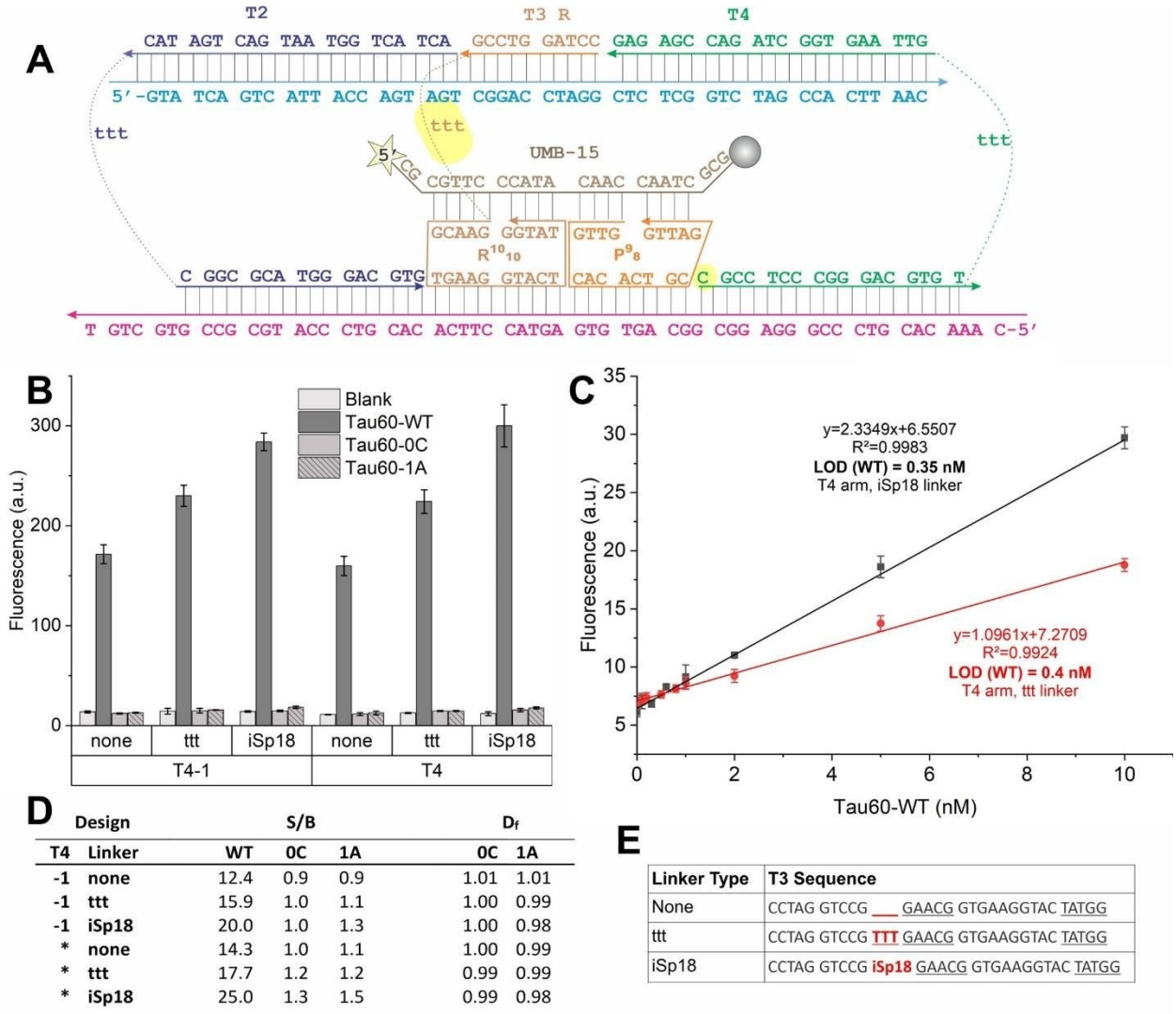

D

Design		S/B			D_f	
T4	Linker	WT	0C	1A	0C	1A
-1	none	12.4	0.9	0.9	1.01	1.01
-1	ttt	15.9	1.0	1.1	1.00	0.99
-1	iSp18	20.0	1.0	1.3	1.00	0.98
*	none	14.3	1.0	1.1	1.00	0.99
*	ttt	17.7	1.2	1.2	0.99	0.99
*	iSp18	25.0	1.3	1.5	0.99	0.98

E

Linker Type	T3 Sequence
None	CCTAG GTCCG ___ GAACG GTGAAGGTAC TATGG
ttt	CCTAG GTCCG **TTT** GAACG GTGAAGGTAC TATGG
iSp18	CCTAG GTCCG **iSp18** GAACG GTGAAGGTAC TATGG

Figure 49 Introduction of a gap between P98 and T4 unwinding arm does not significantly destabilize the OWL structure. For T4, two strands were used; one in which there is no gap between the T4 arm and P98 (denoted with an asterisk) and one in which there is an introduction of a gap (denoted as T4-1) between P-strand and T4. (A) Design of OWL2 in complex with Tau60-WT, P98, and UMB. The linker variation is highlighted region on T3 R. The highlighted nucleotide in T4 represents the nucleotide that is removed to introduce a gap between P-strand and T4 (T4-1). (B) The fluorescent readout from PerkinElmer LS55 Fluorimeter showing that a more flexible linker leads to a higher signal with insignificant compromise to differentiation. (C) The limit of detection for the OWL2 sensor with iSp18 linker and T4 arm is 0.35 nM, which is comparable to the 0.4 nM LOD for the ttt linker. (D) Signal to background and Differentiation factor for the OWL2 variations shown in (B). (E) T3 sequences corresponding to the different linkers.

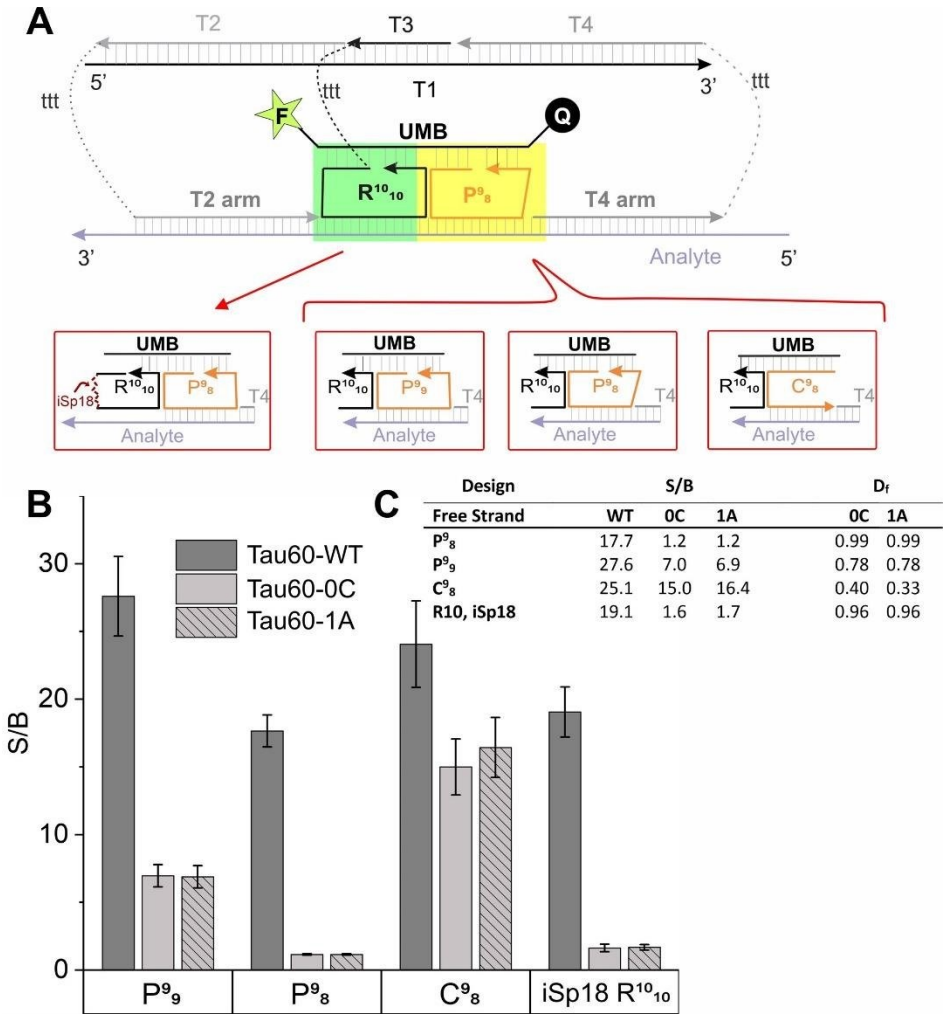

Design	S/B			D_f	
Free Strand	WT	0C	1A	0C	1A
P^9_8	17.7	1.2	1.2	0.99	0.99
P^9_9	27.6	7.0	6.9	0.78	0.78
C^9_8	25.1	15.0	16.4	0.40	0.33
R10, iSp18	19.1	1.6	1.7	0.96	0.96

Figure 50 Constrained Structure of P strand contributes to high selectivity of OWL2 Sensor. (A) OWL2 design with changes in the highlighted region depicted below the OWL2 structure. R1010 with an internal iSp18 linker was used in conjunction with P98, which contains 9 nt complementary to UMB and 8 nt complementary to analyte. P99 contains 9 nt complementary each to both UMB and analyte. C98 has similar binding to P98, but nucleotides complementary to UMB are consecutive starting at the 5'- end and nucleotides complementary to analyte are consecutive ending at the 3'- end. (B) Fluorescence for P99 is higher for t60 WT than for P98 but has diminished differentiation of mutations. Fluorescence for C98 is comparable to that of P99 but has poorer differentiation due to the flexibility of the C-strand.

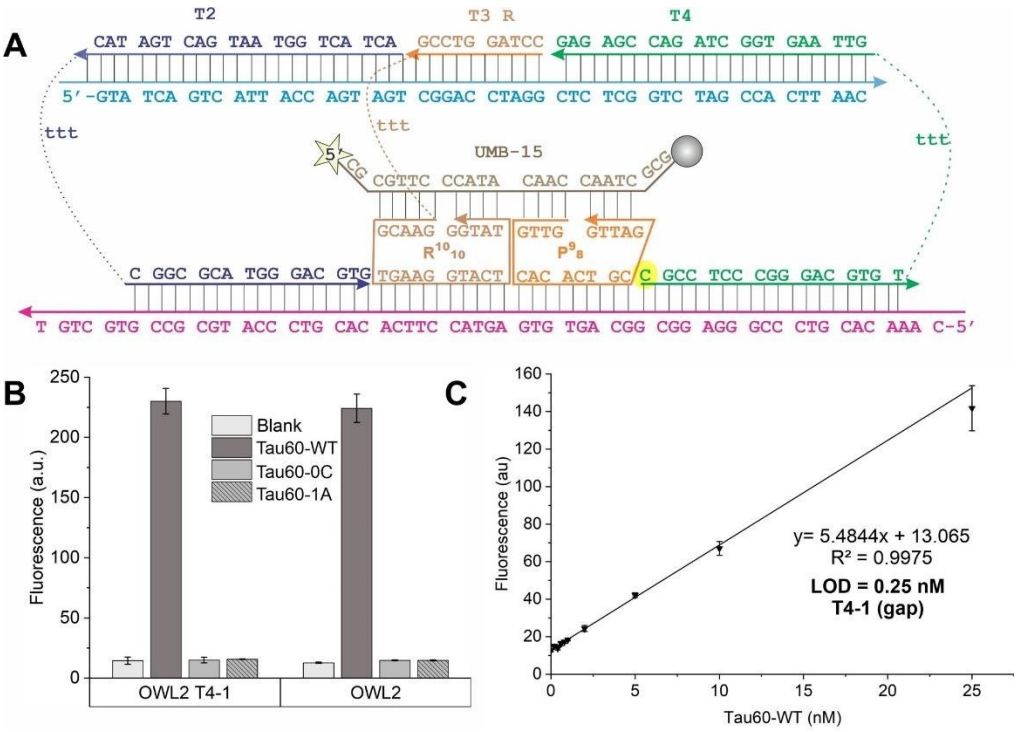

Figure 51 Removal of a nucleotide on T4 to introduce a gap between P and T4 has little effect on fluorescence or limit of detection. (A) OWL2 Design in complex with UMB, P98, and analyte. Removed nucleotide on T4 is highlighted in yellow (B) Fluorescence measured on PerkinElmer LS55 Fluorimeter with no appreciable difference between the two designs. (C) Limit of Detection created using Fluorescence read on a Perkin-Elmer Fluorimeter with a LOD of 0.25 nM for T4-1 (removed nucleotide- a gap is introduced)

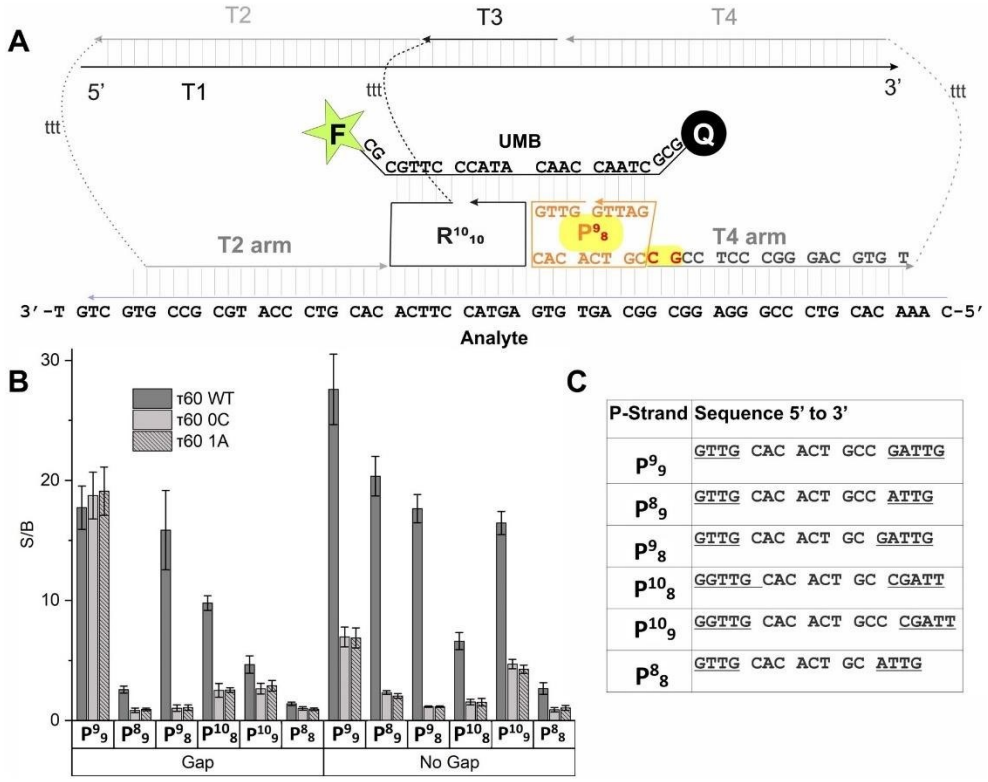

D

Design		S/B			D_f	
Gap	P-strand	WT	0C	1A	0C	1A
+	P^9_9	17.7	18.8	19.1	-0.06	-0.08
+	P^8_9	2.6	0.9	0.9	1.09	1.05
+	P^9_8	15.9	1.0	1.1	1.00	0.99
+	P^{10}_8	9.8	2.5	2.5	0.83	0.82
+	P^{10}_9	4.7	2.7	2.9	0.55	0.48
+	P^8_8	1.4	1.0	0.95	1.06	1.06
-	P^9_9	27.6	7.0	6.9	0.78	0.78
-	P^8_9	20.4	2.3	2.0	0.93	0.95
-	P^9_8	17.7	1.2	1.2	0.99	0.99
-	P^{10}_8	6.6	1.5	1.5	0.90	0.91
-	P^{10}_9	16.5	4.7	4.3	0.76	0.79
-	P^8_8	2.7	0.9	1.1	1.06	0.96

Figure 52 . Introduction of a single gap between the T4 arm and the P strand. (A) The introduction of a gap between P-strand and T4 via removal of a nucleotide on the T4 arm slightly destabilizes the OWL2 Structure. (B). The S/B for fully matched analyte decreases upon the addition of a gap, except in the case of P108. We believe the increase in signal upon introduction of a gap is due to the sequence of the P-strand; when there is a gap the first nucleotide intended to hybridize with the UMB, underlined in (C), may instead hybridize with the analyte since they share complementarity. (D) Signal to background (S/B) and differentiation factor (Df) for all analytes with varying combinations of P-strand and Gap or No Gap.

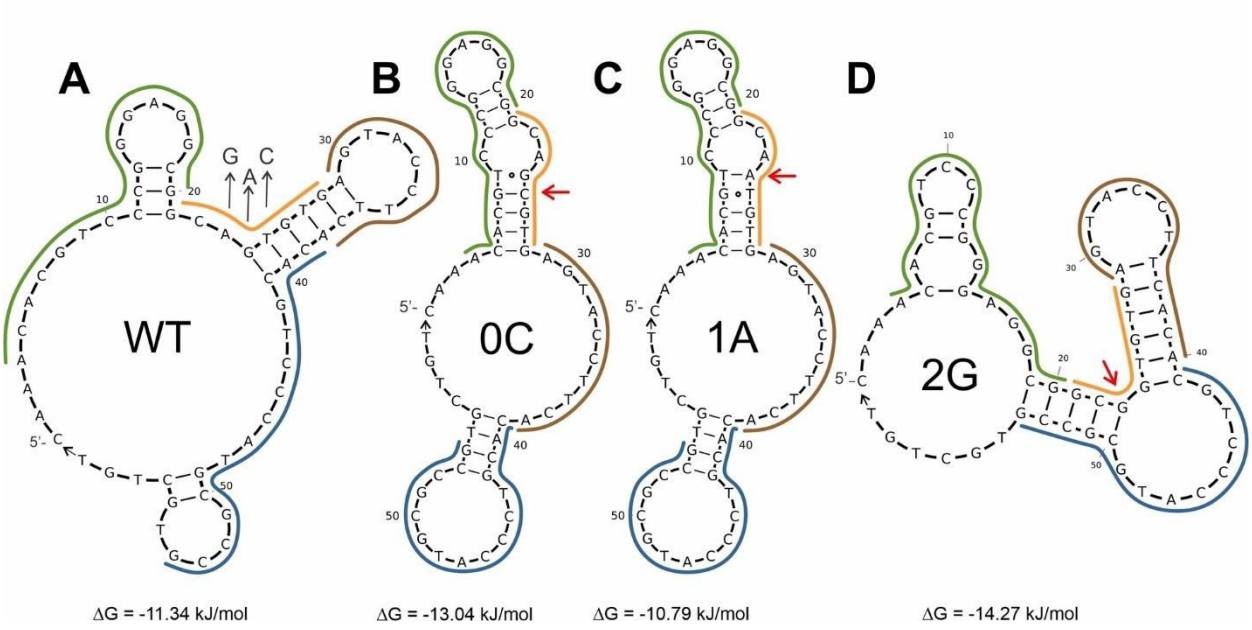

Figure 53 Secondary structures and free energies of Tau analytes. (A) Tau60-WT with T2binding arms outlined in blue, T3-R-binding in brown, P- binding in orange, and T4-binding in green. SNP-containing mutants of tau with mutations 0C (B), 1A (C), and 2G (D) are indicated with a red arrow.

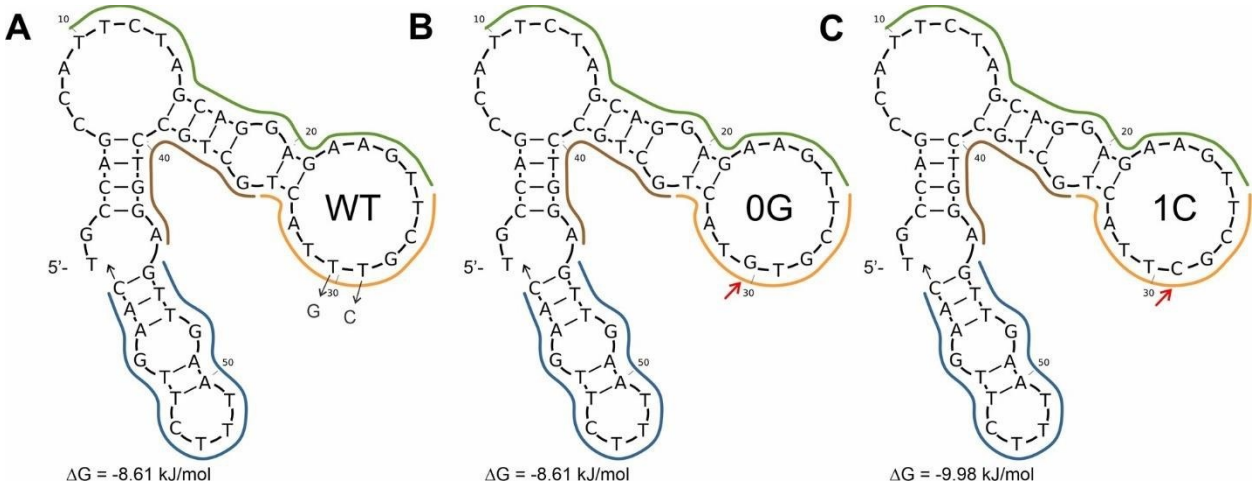

Figure 54 Secondary structures and free energies of Covid analytes. (A) CVD60-WT with T2binding portions highlighted in blue, T3-R-binding in brown, P- binding in orange, T4-binding in green, and SNP-locations highlighted in yellow. (B) and (C) SNP-containing mutants CVD60-0G and CVD60-1C with mutations indicated by red arrows.

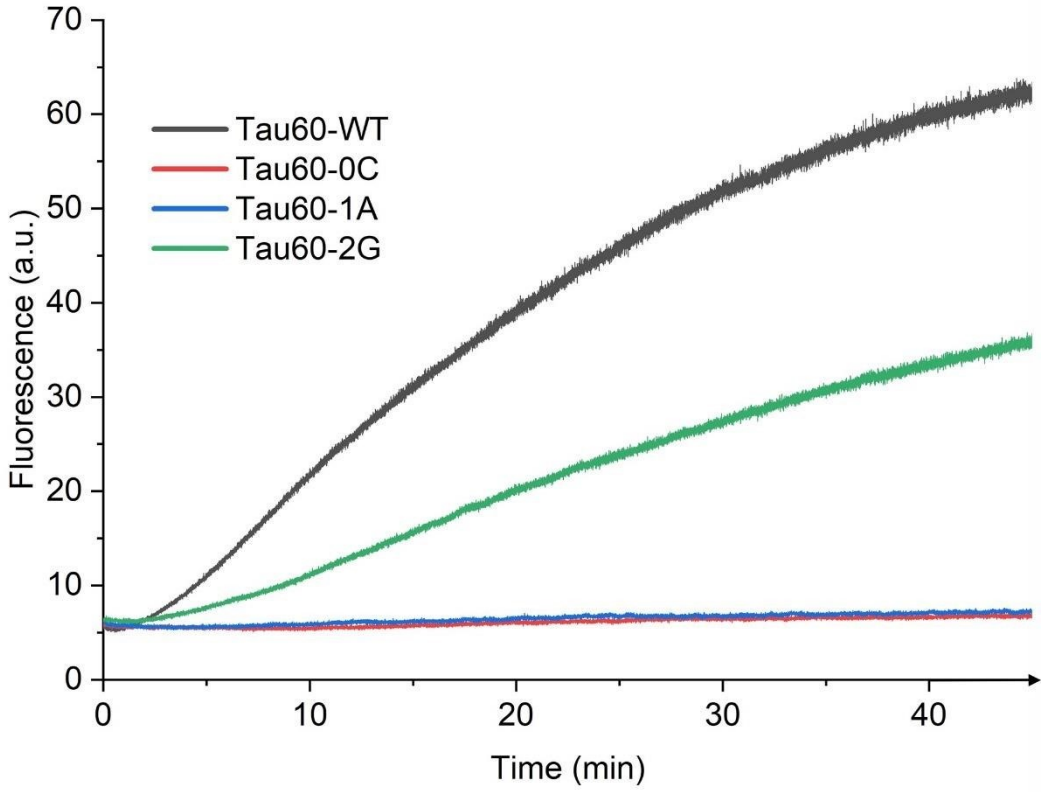

Figure 55 Fluorescent response of OWL2 sensors over time for Tau analytes. Fluorescence was read over 45 min for each mismatch. A four-fold increase in fluorescence can be seen over the first ten minutes with discrimination against mutants 0C and 1A. The 2G mismatch shows a slower increase when compared to the WT.

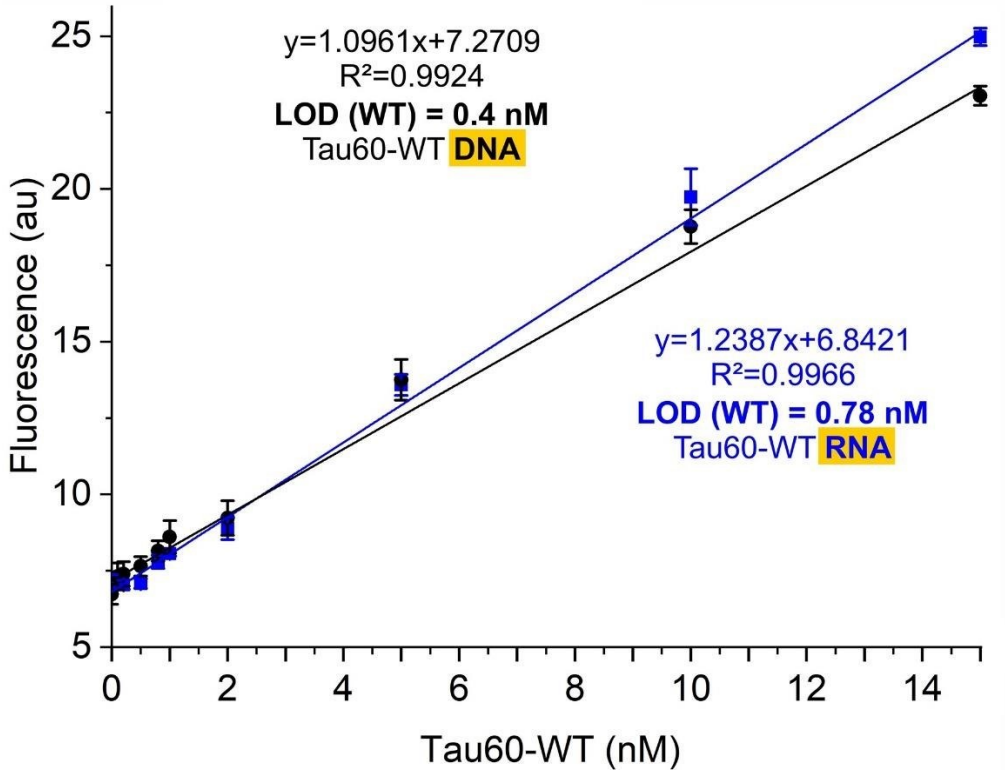

Figure 56. Limit of detection for Tau60-WT DNA and RNA using OWL2 sensor with P98 in buffer 1. LOD for DNA sequence (black) was found to be 0.4 nM and LOD for the RNA sequence (blue) (Table S3) was found to be 0.78 nM. Since the disease-causing SNV-containing analyte is Tau60 mRNA, this provides evidence that our OWL2 sensor would be applicable to real-world analysis

LIST OF REFERENCES

Below is a sample reference with a hanging indent, formatting along APA style.

1 S. Nurk, S. Koren, A. Rhie, M. Rautiainen, A. V. Bzikadze, A. Mikheenko, M. R. Vollger, N. Altemose, L. Uralsky, A. Gershman, S. Aganezov, S. J. Hoyt, M. Diekhans, G. A. Logsdon, M. Alonge, S. E. Antonarakis, M. Borchers, G. G. Bouffard, S. Y. Brooks, G. V. Caldas, N.-C. Chen, H. Cheng, C.-S. Chin, W. Chow, L. G. de Lima, P. C. Dishuck, R. Durbin, T. Dvorkina, I. T. Fiddes, G. Formenti, R. S. Fulton, A. Fungtammasan, E. Garrison, P. G. S. Grady, T. A. Graves-Lindsay, I. M. Hall, N. F. Hansen, G. A. Hartley, M. Haukness, K. Howe, M. W. Hunkapiller, C. Jain, M. Jain, E. D. Jarvis, P. Kerpedjiev, M. Kirsche, M. Kolmogorov, J. Korlach, M. Kremitzki, H. Li, V. V. Maduro, T. Marschall, A. M. McCartney, J. McDaniel, D. E. Miller, J. C. Mullikin, E. W. Myers, N. D. Olson, B. Paten, P. Peluso, P. A. Pevzner, D. Porubsky, T. Potapova, E. I. Rogaev, J. A. Rosenfeld, S. L. Salzberg, V. A. Schneider, F. J. Sedlazeck, K. Shafin, C. J. Shew, A. Shumate, Y. Sims, A. F. A. Smit, D. C. Soto, I. Sović, J.

M. Storer, A. Streets, B. A. Sullivan, F. Thibaud-Nissen, J. Torrance, J. Wagner, B. P. Walenz, A. Wenger, J. M. D. Wood, C. Xiao, S. M. Yan, A. C. Young, S. Zarate, U. Surti, R. C. McCoy, M. Y. Dennis, I. A. Alexandrov, J. L. Gerton, R. J. O'Neill, W. Timp, J. M. Zook, M. C. Schatz, E. E. Eichler, K. H. Miga and A. M. Phillippy, *Science*, 2022, **376**, 44–53.

2 R. Sachidanandam, D. Weissman, S. C. Schmidt, J. M. Kakol, L. D. Stein, G. Marth, S. Sherry, J. C. Mullikin, B. J. Mortimore, D. L. Willey, S. E. Hunt, C. G. Cole, P. C. Coggill, C. M. Rice, Z. Ning, J. Rogers, D. R. Bentley, P.-Y. Kwok, E. R. Mardis, R. T. Yeh, B. Schultz, L. Cook, R. Davenport, M. Dante, L. Fulton, L. Hillier, R. H. Waterston, J. D. McPherson, B. Gilman, S. Schaffner, W. J. Van Etten, D. Reich, J. Higgins, M. J. Daly, B. Blumenstiel, J. Baldwin, N. Stange-Thomann, M. C. Zody, L. Linton, E. S. Lander, D. Altshuler, The International SNP Map Working Group, Cold Spring Harbor Laboratories:, National Center for Biotechnology Information:, The Sanger Centre:, Washington University in St. Louis:, and Whitehead/MIT Center for Genome Research:, *Nature*, 2001, **409**, 928–933.

3 J. Hanson, D. Brezavar, S. Hughes, S. Amudhavalli, E. Fleming, D. Zhou, J. T. Alaimo and P. E. Bonnen, *Clin. Genet.*, 2022, **101**, 214–220.

4 A. Corsi, C. Bombieri, M. T. Valenti and M. G. Romanelli, *Int. J. Mol. Sci.*, 2022, **23**, 15383.

5 M. Niblock and J.-M. Gallo, *Biochem. Soc. Trans.*, 2012, **40**, 677–680.

6 T. Sposito, E. Preza, C. J. Mahoney, N. Setó-Salvia, N. S. Ryan, H. R. Morris, C. Arber, M. J. Devine, H. Houlden, T. T. Warner, T. J. Bushell, M. Zagnoni, T. Kunath, F. J. Livesey, N. C. Fox, M. N. Rossor, J. Hardy and S. Wray, *Hum. Mol. Genet.*, 2015, **24**, 5260–5269.

7 H. Zetterberg and B. B. Bendlin, *Mol. Psychiatry*, 2021, **26**, 296–308.

8 T. G. Richardson, G. M. Leyden, Q. Wang, J. A. Bell, B. Elsworth, G. D. Smith and M. V. Holmes, *PLOS Biol.*, 2022, **20**, e3001547.

9 A. J. Saykin, L. Shen, X. Yao, S. Kim, K. Nho, S. L. Risacher, V. K. Ramanan, T. M. Foroud, K. M. Faber, N. Sarwar, L. M. Munsie, X. Hu, H. D. Soares, S. G. Potkin, P. M. Thompson, J. S. K. Kauwe, R. Kaddurah-Daouk, R. C. Green, A. W. Toga, M. W. Weiner and A. D. N. Initiative, *Alzheimers Dement.*, 2015, **11**, 792–814.

10 Y. Deming, Z. Li, M. Kapoor, O. Harari, J. L. Del-Aguila, K. Black, D. Carrell, Y. Cai, M. V. Fernandez, J. Budde, S. Ma, B. Saef, B. Howells, K. Huang, S. Bertelsen, A. M. Fagan, D. M. Holtzman, J. C. Morris, S. Kim, A. J. Saykin, P. L. De Jager, M. Albert, A. Moghekar, R. O'Brien, M. Riemenschneider, R. C. Petersen, K. Blennow, H. Zetterberg, L. Minthon, V. M. Van Deerlin, V. M.-Y. Lee, L. M. Shaw, J. Q. Trojanowski, G. Schellenberg, J. L. Haines, R. Mayeux, M. A. Pericak-Vance, L. A. Farrer, E. R. Peskind, G. Li, A. F. Di Narzo, J. S. K. Kauwe, A. M. Goate, C. Cruchaga, Alzheimer's Disease Neuroimaging Initiative (ADNI), and The Alzheimer Disease Genetic Consortium (ADGC), *Acta Neuropathol. (Berl.)*, 2017, **133**, 839–856.

11 J. Stevenson-Hoare, A. Heslegrave, G. Leonenko, D. Fathalla, E. Bellou, L. Luckcuck, R. Marshall, R. Sims, B. P. Morgan, J. Hardy, B. de Strooper, J. Williams, H. Zetterberg and V. Escott-Price, *Brain*, 2023, **146**, 690–699.

12 A. F. Schmidt, C. Finan, M. Gordillo-Marañón, F. W. Asselbergs, D. F. Freitag, R. S. Patel, B. Tyl, S. Chopade, R. Faraway, M. Zwierzyna and A. D. Hingorani, *Nat. Commun.*, 2020, **11**, 3255.

13 M. V. Holmes, M. Ala-Korpela and G. D. Smith, *Nat. Rev. Cardiol.*, 2017, **14**, 577–590.

14 A. E. A. Surace and C. M. Hedrich, *Front. Immunol.*, , DOI:10.3389/fimmu.2019.01525.

15 A. X. Maihofer, A. Ratanatharathorn, S. M. J. Hemmings, K. H. Costenbader, V. Michopoulos, R. Polimanti, A. O. Rothbaum, S. Seedat, E. A. Mikita, A. K. Smith, R. M. Salem, R. A. Shaffer, T. Wu, J. Sebat, K. J. Ressler, M. B. Stein, K. C. Koenen, E. J. Wolf, J. A. Sumner and C. M. Nievergelt, *Transl. Psychiatry*, 2024, **14**, 1–10.
16 M. Bagheri, C. Wang, M. Shi, A. Manouchehri, K. T. Murray, M. B. Murphy, C. M. Shaffer, K. Singh, L. K. Davis, G. P. Jarvik, I. B. Stanaway, S. Hebbring, M. P. Reilly, R. E. Gerszten, T. J. Wang, J. D. Mosley and J. F. Ferguson, *Sci. Rep.*, 2021, **11**, 15652.
17 X. Zhang, Y. Li, P. Qi and Z. Ma, *Int. J. Med. Sci.*, 2018, **15**, 1443–1448.
18 H. Zhu, C. Han and T. Wu, *Carcinogenesis*, 2015, **36**, 1213–1222.
19 L.-L. Fang, X.-H. Wang, B.-F. Sun, X.-D. Zhang, X.-H. Zhu, Z.-J. Yu and H. Luo, *Int. J. Mol. Med.*, 2017, **40**, 1624–1630.
20 D. Petrova, R. Jankova, A. Yosifova, V. Tzenova, I. Dimova and D. Toncheva, *Onkologie*, 2006, **29**, 198–200.
21 A. W. Hemming, N. L. Davis, A. Kluftinger, B. Robinson, N. F. Quenville, B. Liseman and J. Lcriche, *J. Surg. Oncol.*, 1992, **51**, 147–152.
22 A. M. Kluftinger, B. W. Robinson, N. F. Quenville, R. J. Finley and N. L. Davis, *Surg. Oncol.*, 1992, **1**, 97–105.
23 R. Zhang, R. Liu, C. Liu, Y. Niu, J. Zhang, B. Guo, C.-Y. Zhang, J. Li, J. Yang and X. Chen, *Cell. Physiol. Biochem.*, 2017, **42**, 1559–1574.
24 S. Zhuang and N. Liu, *Kidney Int. Suppl.*, 2014, **4**, 70–74.
25 S. He, N. Liu, G. Bayliss and S. Zhuang, *Am. J. Physiol.-Ren. Physiol.*, 2013, **304**, F356– F366.
26 J. Pancewicz-Wojtkiewicz, *Cancer Med.*, 2016, **5**, 3572–3578.
27 T. Sonoda, S. Nishikawa, R. Sakakibara, M. Saiki, R. Ariyasu, J. Koyama, S. Kitazono, N. Yanagitani, A. Horiike, F. Ohyanagi, H. Ninomiya, Y. Ishikawa and M. Nishio, *Respir. Med. Case Rep.*, 2018, **24**, 19–21.
28 Y. Wang, Z. Guo, Y. Li and Q. Zhou, *Open Med.*, 2016, **11**, 68–77.
29 T. Masuda, S. Miura, Y. Sato, M. Tachihara, A. Bessho, A. Nakamura, T. Miyawaki, K. Yoshimine, M. Mori, H. Shiraishi, K. Hamai, K. Haratani, S. Maeda, E. Tabata, C. Kitagawa, J. Tanizaki, T. Imai, S. Nogami, N. Yamamoto, K. Nakagawa and N. Hattori, *Sci. Rep.*, 2023, **13**, 19729.
30 M. A. Field, *Immunol. Cell Biol.*, 2021, **99**, 146–156.
31 P. D. Stenson, E. V. Ball, M. Mort, A. D. Phillips, J. A. Shiel, N. S. T. Thomas, S. Abeysinghe, M. Krawczak and D. N. Cooper, *Hum. Mutat.*, 2003, **21**, 577–581.
32 S. H. Jiang, V. Athanasopoulos, J. I. Ellyard, A. Chuah, J. Cappello, A. Cook, S. B. Prabhu, J. Cardenas, J. Gu, M. Stanley, J. A. Roco, I. Papa, M. Yabas, G. D. Walters, G. Burgio, K. McKeon, J. M. Byers, C. Burrin, A. Enders, L. A. Miosge, P. F. Canete, M. Jelusic, V. Tasic, A. C. Lungu, S. I. Alexander, A. R. Kitching, D. A. Fulcher, N. Shen, T. Arsov, P. A. Gatenby, J. J. Babon, D. F. Mallon, C. de Lucas Collantes, E. A. Stone, P. Wu, M. A. Field, T. D. Andrews, E. Cho, V. Pascual, M. C. Cook and C. G. Vinuesa, *Nat. Commun.*, 2019, **10**, 2201.
33 G. Cao, Y. Qiu, K. Long, Y. Ma, H. Luo, M. Yang, J. Hou, D. Huo and C. Hou, *Anal. Chem.*, 2022, **94**, 17653–17661.
34 C. Graham, A. Eshaghi, A. Sarabia, S. Zittermann, P. Stapleton, J. V. Kus and S. N. Patel, *Access Microbiol*, 2020, **2**, acmi000111.
35 T.-L. Li, M.-W. Wu, W.-C. Lin, C.-H. Lai, Y.-H. Chang, L.-J. Su and W.-Y. Chen, *Anal. Bioanal. Chem.*, 2019, **411**, 3871–3880.

36 C. P. Paweletz, A. G. Sacher, C. K. Raymond, R. S. Alden, A. O'Connell, S. L. Mach, Y. Kuang, L. Gandhi, P. Kirschmeier, J. M. English, L. P. Lim, P. A. Jänne and G. R. Oxnard, *Clin. Cancer Res.*, 2016, **22**, 915–922.
37 E. C. Berglund, C. M. Lindqvist, S. Hayat, E. Övernäs, N. Henriksson, J. Nordlund, P. Wahlberg, E. Forestier, G. Lönnerholm and A.-C. Syvänen, *BMC Genomics*, 2013, **14**, 856.
38 J. S. Welch, T. J. Ley, D. C. Link, C. A. Miller, D. E. Larson, D. C. Koboldt, L. D. Wartman, T. L. Lamprecht, F. Liu, J. Xia, C. Kandoth, R. S. Fulton, M. D. McLellan, D. J. Dooling, J. W. Wallis, K. Chen, C. C. Harris, H. K. Schmidt, J. M. Kalicki-Veizer, C. Lu, Q. Zhang, L. Lin, M. D. O'Laughlin, J. F. McMichael, K. D. Delehaunty, L. A. Fulton, V. J. Magrini, S. D. McGrath, R. T. Demeter, T. L. Vickery, J. Hundal, L. L. Cook, G. W. Swift, J. P. Reed, P. A. Alldredge, T. N. Wylie, J. R. Walker, M. A. Watson, S. E. Heath, W. D. Shannon, N. Varghese, R. Nagarajan, J. E. Payton, J. D. Baty, S. Kulkarni, J. M. Klco, M. H. Tomasson, P. Westervelt, M. J. Walter, T. A. Graubert, J. F. DiPersio, L. Ding, E. R. Mardis and R. K. Wilson, *Cell*, 2012, **150**, 264–278.
39 T. Li, H. Zou, J. Zhang, H. Ding, C. Li, X. Chen, Y. Li, W. Feng and K. Kageyama, *Analyst*, 2022, **147**, 3993–3999.
40 M. Azhar, R. Phutela, M. Kumar, A. H. Ansari, R. Rauthan, S. Gulati, N. Sharma, D. Sinha, S. Sharma, S. Singh, S. Acharya, S. Sarkar, D. Paul, P. Kathpalia, M. Aich, P. Sehgal, G. Ranjan, R. C. Bhoyar, K. Singhal, H. Lad, P. K. Patra, G. Makharia, G. R. Chandak, B. Pesala, D. Chakraborty and S. Maiti, *Biosens. Bioelectron.*, 2021, **183**, 113207.
41 V. Taly, D. Pekin, L. Benhaim, S. K. Kotsopoulos, D. Le Corre, X. Li, I. Atochin, D. R. Link, A. D. Griffiths, K. Pallier, H. Blons, O. Bouché, B. Landi, J. B. Hutchison and P. Laurent-Puig, *Clin. Chem.*, 2013, **59**, 1722–1731.
42 S. Bai, B. Xu, Y. Zhang, Y. Zhang, H. Dang, S. Yang, C. Zuo, L. Zhang, J. Li and G. Xie, *Biosens. Bioelectron.*, 2020, **154**, 112092.
43 N. Zhang and D. H. Appella, *J. Infect. Dis.*, 2010, **201 Suppl 1**, S42–S45.
44 M. B. Thayer, J. M. Lade, D. Doherty, F. Xie, B. Basiri, O. S. Barnaby, N. S. Bala and B. M. Rock, *Sci. Rep.*, 2019, **9**, 3566.
45 F. Bekkaoui, I. Poisson, W. Crosby, L. Cloney and P. Duck, *BioTechniques*, 1996, **20**, 240– 248.
46 Q. Huang, Z. Liu, Y. Liao, X. Chen, Y. Zhang and Q. Li, *PLOS ONE*, 2011, **6**, e19206.
47 S. Tyagi and F. R. Kramer, *Nat. Biotechnol.*, 1996, **14**, 303–308.
48 V. V. Demidov and M. D. Frank-Kamenetskii, *Trends Biochem Sci*, 2004, **29**, 62–71.
49 D. M. Kolpashchikov, *Chem. Rev.*, 2010, **110**, 4709–4723.
50 R. Van Hoof, M. Szymonik, S. K. Nomidis, K. Hollanders, A. Jacobs, I. Nelissen, P. Wagner and J. Hooyberghs, *Sens. Actuators B Chem.*, 2022, **368**, 132175.
51 L. Chen, H. Huang, Z. Wang, K. Deng and H. Huang, *Talanta*, 2022, **243**, 123352.
52 X. Ke, Y. Ou, Y. Lin and T. Hu, *Biosens. Bioelectron.*, 2022, **212**, 114428.
53 M. Ahmed, N. M. Pollak, G. J. Devine and J. Macdonald, *Sens. Actuators B Chem.*, 2022, **367**, 132085.
54 M. Stancescu, T. A. Fedotova, J. Hooyberghs, A. Balaeff and D. M. Kolpashchikov, *J. Am. Chem. Soc.*, 2016, **138**, 13465–13468.
55 P. Hardinge and J. A. H. Murray, *BMC Biotechnol.*, 2019, **19**, 55.
56 P. W. K. Rothemund, *Nature*, 2006, **440**, 297–302.
57 N. C. Seeman and H. F. Sleiman, *Nat. Rev. Mater.*, 2017, **3**, 1–23.

58 K. E. Dunn, F. Dannenberg, T. E. Ouldridge, M. Kwiatkowska, A. J. Turberfield and J. Bath, *Nature*, 2015, **525**, 82–86.
59 Y. Tian, J. R. Lhermitte, L. Bai, T. Vo, H. L. Xin, H. Li, R. Li, M. Fukuto, K. G. Yager, J. S. Kahn, Y. Xiong, B. Minevich, S. K. Kumar and O. Gang, *Nat. Mater.*, 2020, **19**, 789–796.
60 C. Zhang, R. J. Macfarlane, K. L. Young, C. H. J. Choi, L. Hao, E. Auyeung, G. Liu, X. Zhou and C. A. Mirkin, *Nat. Mater.*, 2013, **12**, 741–746.
61 K. F. Wagenbauer, C. Sigl and H. Dietz, *Nature*, 2017, **552**, 78–83.
62 L. L. Ong, N. Hanikel, O. K. Yaghi, C. Grun, M. T. Strauss, P. Bron, J. Lai-Kee-Him, F. Schueder, B. Wang, P. Wang, J. Y. Kishi, C. Myhrvold, A. Zhu, R. Jungmann, G. Bellot, Y. Ke and P. Yin, *Nature*, 2017, **552**, 72–77.
63 N. C. Seeman and H. F. Sleiman, *Nat. Rev. Mater.*, 2017, **3**, 1–23.
64 N. C. Seeman, *J. Theor. Biol.*, 1982, **99**, 237–247.
65 S. Zhao, S. Zhang, H. Hu, Y. Cheng, K. Zou, J. Song, J. Deng, L. Li, X.-B. Zhang, G. Ke and J. Sun, *Angew. Chem.*, 2023, **135**, e202303121.
66 T. Tian, T. Zhang, S. Shi, Y. Gao, X. Cai and Y. Lin, *Nat. Protoc.*, 2023, **18**, 1028–1055.
67 B. Wei, M. Dai and P. Yin, *Nature*, 2012, **485**, 623–626.
68 M. Lawal, J. Payne, H. Onyeaka, A. M. Alao and E. Okoampah, *Nano Sel.*, 2024, **5**, 2300078.
69 D. Houhoula, M. Kouzilou, C. Tzogias, V. Kyrana, C. Sflomos, J. Tsaknis and V. Lougovois, *J. Food Res.*, 2017, **6**, p34.
70 P. Valentini, A. Galimberti, V. Mezzasalma, F. De Mattia, M. Casiraghi, M. Labra and P. P. Pompa, *Angew. Chem. Int. Ed.*, 2017, **56**, 8094–8098.
71 P. Valentini, A. Galimberti, V. Mezzasalma, F. De Mattia, M. Casiraghi, M. Labra and P. P. Pompa, *Angew. Chem.*, 2017, **129**, 8206–8210.
72 Y. Zhang, F. Lu, K. G. Yager, D. van der Lelie and O. Gang, *Nat. Nanotechnol.*, 2013, **8**, 865–872.
73 B. Wei, M. Dai and P. Yin, *Nature*, 2012, **485**, 623–626.
74 H. Yan, S. H. Park, G. Finkelstein, J. H. Reif and T. H. LaBean, *Science*, 2003, **301**, 1882–1884.
75 S. Ko, H. Liu, Y. Chen and C. Mao, *Biomacromolecules*, 2008, **9**, 3039–3043.
76 W. Sun, T. Jiang, Y. Lu, M. Reiff, R. Mo and Z. Gu, *J. Am. Chem. Soc.*, 2014, **136**, 14722–14725.
77 T. Tian, T. Zhang, S. Shi, Y. Gao, X. Cai and Y. Lin, *Nat. Protoc.*, 2023, **18**, 1028–1055.
78 Y. Nie, J. Jiang, K. Peng, Y. Chai and R. Yuan, *Biosens. Bioelectron.*, 2021, **175**, 112848.
79 S. Modi, S. M. G., D. Goswami, G. D. Gupta, S. Mayor and Y. Krishnan, *Nat. Nanotechnol.*, 2009, **4**, 325–330.
80 D. Gareau, A. Desrosiers and A. Vallée-Bélisle, *Nano Lett.*, 2016, **16**, 3976–3981.
81 C. Bu, L. Mu, X. Cao, M. Chen, G. She and W. Shi, *Nanotechnology*, 2018, **29**, 295501.
82 Y.-J. Zhou, Y.-H. Wan, C.-P. Nie, J. Zhang, T.-T. Chen and X. Chu, *Anal. Chem.*, 2019, **91**, 10366–10370.
83 X. Zhang, L. Pan, R. Guo, Y. Zhang, F. Li, M. Li, J. Li, J. Shi, F. Qu, X. Zuo and X. Mao, *Chem. Commun.*, 2022, **58**, 3673–3676.
84 S. Li, Q. Jiang, S. Liu, Y. Zhang, Y. Tian, C. Song, J. Wang, Y. Zou, G. J. Anderson, J.-Y. Han, Y. Chang, Y. Liu, C. Zhang, L. Chen, G. Zhou, G. Nie, H. Yan, B. Ding and Y. Zhao, *Nat. Biotechnol.*, 2018, **36**, 258–264.

85 Y. Zhang, D. Bai, J. Pu, L. Zhang, W. Wang, T. Feng, J. Zhang, H. Yu, X. Han, K. Lv, L. Wang, Y. Guo and G. Xie, *Chem. Eng. J.*, 2024, **499**, 156044.
86 Z. Zhou, J. D. Brennan and Y. Li, *Angew. Chem. Int. Ed.*, 2020, **59**, 10401–10405.
87 N. Arulkumaran, C. Lanphere, C. Gaupp, J. R. Burns, M. Singer and S. Howorka, *ACS Nano*, 2021, **15**, 4394–4404.
88 T. Galbadage, D. Liu, L. B. Alemany, R. Pal, J. M. Tour, R. S. Gunasekera and J. D. Cirillo, *ACS Nano*, 2019, **13**, 14377–14387.
89 D. Liu, V. García-López, R. S. Gunasekera, L. Greer Nilewski, L. B. Alemany, A. Aliyan, T. Jin, G. Wang, J. M. Tour and R. Pal, *ACS Nano*, 2019, **13**, 6813–6823.
90 J. Zhang, P. Zhao, W. Li, L. Ye, L. Li, Z. Li and M. Li, *Angew. Chem. Int. Ed.*, 2022, **61**, e202117562.
91 J. Hahn, S. F. J. Wickham, W. M. Shih and S. D. Perrault, *ACS Nano*, 2014, **8**, 8765–8775.
92 S. M. Taghdisi, N. M. Danesh, M. Ramezani, R. Yazdian-Robati and K. Abnous, *Mol. Pharm.*, 2018, **15**, 1972–1978.
93 A. R. Chandrasekaran, *Nat. Rev. Chem.*, 2021, **5**, 225–239.
94 Y. T. E. Chiu, H. Li and C. H. J. Choi, *Small*, 2019, **15**, 1805416.
95 P. Chidchob, T. G. W. Edwardson, C. J. Serpell and H. F. Sleiman, *J. Am. Chem. Soc.*, 2016, **138**, 4416–4425.
96 C. Lin, S. D. Perrault, M. Kwak, F. Graf and W. M. Shih, *Nucleic Acids Res.*, 2013, **41**, e40.
97 A. Shaw, E. Benson and B. Högberg, *ACS Nano*, 2015, **9**, 4968–4975.
98 D. M. Kolpashchikov, *Scientifica*, 2012, **2012**, e928783.
99 Created with BioRender.com.
100 E. Navarro, G. Serrano-Heras, M. J. Castaño and J. Solera, *Clin. Chim. Acta*, 2015, **439**, 231–250.
101 S. A. E. Marras, S. Tyagi and F. R. Kramer, *Clin. Chim. Acta*, 2006, **363**, 48–60.
102 M. W. McCarthy and T. J. Walsh, *Expert Rev. Mol. Diagn.*, 2016, **16**, 1025–1036.
103 V. Kia, A. Tafti, M. Paryan and S. Mohammadi-Yeganeh, *Ir. J. Med. Sci. 1971 -*, 2023, **192**, 723–729.
104 E. M. Criscuolo, F. Barbanti and P. Spigaglia, *Microbiol. Res.*, 2024, **15**, 354–370.
105 Z. Ma, M. Ma, X. Cao, Y. Jiang and D. Gao, *Microchim. Acta*, 2024, **191**, 430.
106 M. C. Mears, T. L. Olivier, D. Williams-Coplin, E. Espinoza and A. Bakre, *Sci. Rep.*, 2024, **14**, 18047.
107 Z. Zhang, S. Wang, J. Ma, T. Zhou, F. Wang, X. Wang and G. Zhang, *ACS Biomater. Sci. Eng.*, 2020, **6**, 3114–3121.
108 S. Tyagi, S. A. E. Marras and F. R. Kramer, *Nat. Biotechnol.*, 2000, **18**, 1191–1196.
109 Q. Guo, X. Yang, K. Wang, W. Tan, W. Li, H. Tang and H. Li, *Nucleic Acids Res.*, 2009, **37**, e20.
110 A. Tsourkas, M. A. Behlke, S. D. Rose and G. Bao, *Nucleic Acids Res.*, 2003, **31**, 1319–1330.
111 G. Bonnet, S. Tyagi, A. Libchaber and F. R. Kramer, *Proc. Natl. Acad. Sci.*, 1999, **96**, 6171–6176.
112 L. Peng and W. Tan, in *Molecular Beacons*, eds. C. J. Yang and W. Tan, Springer, Berlin, Heidelberg, 2013, pp. 19–43.
113 Y. Kim, C. J. Yang and W. Tan, *Nucleic Acids Res.*, 2007, **35**, 7279–7287.
114 S. A. Benner, *Acc. Chem. Res.*, 2004, **37**, 784–797.

115 P. Sheng, Z. Yang, Y. Kim, Y. Wu, W. Tan and S. A. Benner, *Chem. Commun.*, 2008, 5128–5130.
116 J. Caton-Williams, B. Fiaz, R. Hoxhaj, M. Smith and Z. Huang, *Sci. China Chem.*, 2012, **55**, 80–89.
117 R. Liu, Q. Hua, Q. Lou, J. Wang, X. Li, Z. Ma and Y. Yang, *J. Org. Chem.*, 2021, **86**, 4763–4778.
118 Y. Li, C. Abraham, O. Suslov, O. Yaren, R. W. Shaw, M.-J. Kim, S. Wan, P. Marliere and S. A. Benner, *ACS Synth. Biol.*, 2023, **12**, 1772–1781.
119 S. Tyagi and F. R. Kramer, *Nat. Biotechnol.*, 1996, **14**, 303–308.
120 C. Nguyen, J. Grimes, Y. V. Gerasimova and D. M. Kolpashchikov, *Chemistry*, 2011, **17**, 13052–8.
121 A. Tsourkas, M. A. Behlke, S. D. Rose and G. Bao, *Nucleic Acids Res.*, 2003, **31**, 1319–1330.
122 S. Tyagi, D. P. Bratu and F. R. Kramer, *Nat. Biotechnol.*, 1998, **16**, 49–53.
123 J. Perlette and W. Tan, *Anal. Chem.*, 2001, **73**, 5544–5550.
124 C. Rossi-Gendron, F. El Fakih, L. Bourdon, K. Nakazawa, J. Finkel, N. Triomphe, L. Chocron, M. Endo, H. Sugiyama, G. Bellot, M. Morel, S. Rudiuk and D. Baigl, *Nat. Nanotechnol.*, 2023, **18**, 1311–1318.
125 N. C. Seeman, *J. Theor. Biol.*, 1982, **99**, 237–247.
126 P. W. K. Rothemund, *Nature*, 2006, **440**, 297–302.
127 A. Porchetta, R. Ippodrino, B. Marini, A. Caruso, F. Caccuri and F. Ricci, *J. Am. Chem. Soc.*, 2018, **140**, 947–953.
128 Y. Song, X. Jin, Y. Zhao, S. Cheng, S. Xu, S. Bu, L. Liu, C. Zhou and C. Pang, *Microchim. Acta*, 2024, **191**, 553.
129 X. Huang, R. Narayanaswamy, K. Fenn, S. Szpakowski, C. Sasaki, J. Costa, P. Blancafort and P. M. Lizardi, *DNA Cell Biol.*, 2012, **31**, S-2.
130 M. Chern, P. M. Garden, R. C. Baer, J. E. Galagan and A. M. Dennis, *Angew. Chem.*, 2020, **132**, 21781–21786.
131 T. Hachigian, D. Lysne, E. Graugnard and J. Lee, *ACS Omega*, 2021, **6**, 26888–26896.
132 A. K. D. Younger, N. C. Dalvie, A. G. Rottinghaus and J. N. Leonard, *ACS Synth. Biol.*, 2017, **6**, 311–325.
133 W. Hou, J. Du, T. Liu, W. Wang, Y. Ai, M. Zhou, H. Wang and Z. Wang, *Food Anal. Methods*, 2024, **17**, 1394–1401.
134 Q. Huang, D. Chen, C. Du, Q. Liu, S. Lin, L. Liang, Y. Xu, Y. Liao and Q. Li, *Proc. Natl. Acad. Sci.*, 2022, **119**, e2110672119.
135 X. Li, Y. Huang, Y. Guan, M. Zhao and Y. Li, *Anal. Chem.*, 2006, **78**, 7886–7890.
136 Y.-W. Lin, H.-T. Ho, C.-C. Huang and H.-T. Chang, *Nucleic Acids Res.*, 2008, **36**, e123.
137 V. V. Demidov and M. D. Frank-Kamenetskii, *Trends Biochem. Sci.*, 2004, **29**, 62–71.
138 J. F. Hopkins and S. A. Woodson, *Nucleic Acids Res*, 2005, **33**, 5763–70.
139 B. A. Armitage, *Drug Discov. Today*, 2003, **8**, 222–228.
140 S. A. Kushon, J. P. Jordan, J. L. Seifert, H. Nielsen, P. E. Nielsen and B. A. Armitage, *J. Am. Chem. Soc.*, 2001, **123**, 10805–10813.
141 S. Lane, J. Evermann, F. Loge and D. R. Call, *Biosens. Bioelectron.*, 2004, **20**, 728–735.
142 W.-T. Liu, H. Guo and J.-H. Wu, *Appl. Environ. Microbiol.*, 2007, **73**, 73–82.

143 J. Grimes, Y. V. Gerasimova and D. M. Kolpashchikov, *Angew. Chem. Int. Ed.*, 2010, **49**, 8950–8953.
144 N. Weigert, A.-L. Schweiger, J. Gross, M. Matthes, S. Corbacioglu, G. Sommer and T. Heise, *Biol. Chem.*, 2023, **404**, 1123–1136.
145 A. Tsourkas, M. A. Behlke, S. D. Rose and G. Bao, *Nucleic Acids Res.*, 2003, **31**, 1319–1330.
146 C. Fan, K. W. Plaxco and A. J. Heeger, *Proc. Natl. Acad. Sci. U. S. A.*, 2003, **100**, 9134–9137.
147 M. Zuker, *Nucleic Acids Res.*, 2003, **31**, 3406–3415.
148 T. Guo, W. Noble and D. P. Hanger, *Acta Neuropathol*, 2017, **133**, 665–704.
149 R. J. Karadeema, M. Stancescu, T. P. Steidl, S. C. Bertot and D. M. Kolpashchikov, *Nanoscale*, 2018, **10**, 10116–10122.
150 M. Goedert and R. Jakes, *Biochim. Biophys. Acta BBA - Mol. Basis Dis.*, 2005, **1739**, 240–250.
151 M. Hasegawa, M. J. Smith, M. Iijima, T. Tabira and M. Goedert, *FEBS Lett.*, 1999, **443**, 93–96.
152 J. N. Zadeh, C. D. Steenberg, J. S. Bois, B. R. Wolfe, M. B. Pierce, A. R. Khan, R. M. Dirks and N. A. Pierce, *J. Comput. Chem.*, 2011, **32**, 170–173.
153 D. M. Kolpashchikov, *J. Am. Chem. Soc.*, 2006, **128**, 10625–10628.
154 S. Takiguchi, F. Kambara, M. Tani, T. Sugiura and R. Kawano, *Anal. Chem.*, 2023, **95**, 14675–14685.
155 E. Koscianska, J. Starega-Roslan, L. J. Sznajder, M. Olejniczak, P. Galka-Marciniak and W. J. Krzyzosiak, *BMC Mol. Biol.*, 2011, **12**, 14.
156 S. Sharbati-Tehrani, B. Kutz-Lohroff, R. Bergbauer, J. Scholven and R. Einspanier, *BMC Mol. Biol.*, 2008, **9**, 34.
157 W. Ahmad, B. Gull, J. Baby and F. Mustafa, *Curr. Issues Mol. Biol.*, 2021, **43**, 457–484.
158 T. A. Molden, C. T. Niccum and D. M. Kolpashchikov, *Angew. Chem.*, 2020, **132**, 21376–21380.
159 Y. Sun, Y. Sun, W. Tian, C. Liu, K. Gao and Z. Li, *Chem. Sci.*, 2018, **9**, 1344–1351.
160 X. Chen, J. Huang, S. Zhang, F. Mo, S. Su, Y. Li, L. Fang, J. Deng, H. Huang, Z. Luo and J. Zheng, *ACS Appl. Mater. Interfaces*, 2019, **11**, 3745–3752. 161 A. Cao and C. Zhang, *Anal. Chem.*, 2012, **84**, 6199–6205.